

**CRAB PULSAR GIANT RADIO PULSES: AN
INVESTIGATION OF MICROSECOND-SCALE
STRUCTURE AND DISPERSION
CHARACTERISTICS**

by

Jared Harrington Crossley

Submitted in Partial Fulfillment
of the Requirements for the Degree of
Master of Science in Physics

New Mexico Institute of Mining and Technology
Socorro, New Mexico

May, 2009

To the seekers
and the mysteries
that draw them out.

Jared Harrington Crossley
New Mexico Institute of Mining and Technology
May, 2009

ABSTRACT

I have analyzed microsecond-scale structures, “microbursts,” in single giant pulses from the Crab pulsar and found rapid variability in microburst flux, width, energy, and dispersion measure. Flux, widths, and energies vary over 2 orders of magnitude for bursts recorded at similar frequencies. Width measurements reveal the existence of a variable and shallow pulse broadening power law that acts in addition to steeper interstellar scattering. Plots of microburst flux and width contain an upper limit at all frequencies that may be related to a maximum microburst energy. I find that microburst energies are variable in both the observed and emitted frames. Simultaneous two-frequency observations reveal that microburst bandwidths are < 4 GHz, and both high- and low-frequency microburst energies and widths are well correlated; spectral indices of individual bursts vary greatly but as a group are roughly consistent with average profile measurements. Giant pulse dispersion measure (DM) follows the same trend as average profile DM over long time scales, but on shorter scales of minutes to hours, giant pulse DM varies randomly. The random variation is much greater in Crab interpulses than in main pulses. This suggests that a variable dispersion occurs in the magnetosphere. Furthermore, the interpulse DM has a slight frequency dependence (after dedispersion) which

suggests a non-cold-plasma dispersion process. I compare my data with two models from the literature, but find that neither model describes my data well. I have also found a new Crab pulse echo event in data from 1996; my observations constrain the event lifetime to < 4 days. I analyze this event in addition to previously studied giant pulse echoes from 1997. Both echo events are visible as microbursts that trail the primary burst by 40 to $120 \mu\text{s}$; echo flux, widths, and energies correlate well with the respective primary burst characteristics. I suggest that this short lifetime event may be a result of refraction from Crab nebula wisps—evolving structures near the star associated with the pulsar wind.

ACKNOWLEDGMENT

The research project reported in this thesis has come together with the assistance of many people. I extend my gratitude to all who have assisted me with support, both professional and personal, during my tenure as a graduate student. To my fellow students, colleagues, family members, and friends: thank you.

I thank my committee members, Jean Eilek, Tim Hankins, and Peter Hofner, for agreeing to work with me on this project. Jean and Tim, in particular, have closely advised me on the research reported in this thesis, from the very beginning in the Spring of 2004. For their interest, enthusiasm, encouragement and patience, I am very grateful.

I also wish to thank my fellow graduate students who have aided me in many ways during the course of my studies. With regard to this thesis, I am especially grateful to Jim Sheckard, Jeff Kern, and James Anderson for discussions that improved my understanding of pulsar science, computer programming, and a host of other research minutiae necessary to the present study.

I am grateful to those who provided me financial support during my time as a graduate student. This includes my two research advisors Jean and Tim, who supported me as a research assistant during the first half of my schooling, and Nicole Radziwill, of the National Radio Astronomy Observatory, who hired me as a part-time and later full-time employee during the second half.

Nicole also gave me the flexibility to schedule and coordinate my professional and academic affairs such that I was able to accomplish both together; this was a boon to my degree progress and I extend my thanks to her.

I wish to thank some friends who have offered me emotional support during a long and sometimes daunting thesis project. My thanks to Rev. Judy Romero-Oak for encouraging me to believe in myself. My thanks to Fred Yarger who reminded me numerous times that obtaining a graduate degree has much more to do with patience and commitment than with intelligence and smarts. My thanks also to Prateeksha Bogardus for her recognition of the importance of my degree completion and her encouragement to keep going.

Finally, I give my love and thanks to Amanda Crossley, to whom I became engaged and married during the course of this work, and who has been throughout a source of support, encouragement and inspiration. Thank you.

This dissertation was typeset with \LaTeX^1 by the author.

¹ \LaTeX document preparation system was developed by Leslie Lamport as a special version of Donald Knuth's \TeX program for computer typesetting. \TeX is a trademark of the American Mathematical Society. The \LaTeX macro package for the New Mexico Institute of Mining and Technology dissertation format was adapted from Gerald Arnold's modification of the \LaTeX macro package for The University of Texas at Austin by Khe-Sing The.

TABLE OF CONTENTS

LIST OF TABLES	vii
LIST OF FIGURES	viii
1. INTRODUCTION TO THE CRAB PULSAR	1
1.1 Pulsar Basics	1
1.1.1 A Simple Magnetospheric Model	3
1.2 The Crab Pulsar and Nebula	7
1.2.1 Crab Pulsar	7
1.2.2 Crab Nebula	10
1.3 Propagation Effects	12
1.3.1 Pulse Dispersion	12
1.3.2 Scatter Broadening	14
1.3.3 Interstellar Scintillation	16
1.4 Signal Processing	17
1.4.1 Dedispersion	19
1.5 Observations	20
1.5.1 Capturing Giant Pulses: On-pulse Energy Threshold	22
1.6 This Study	23
2. MICROSECOND-SCALE SUBPULSE CHARACTERISTICS	24
2.1 Introduction	24

2.2	Observations	26
2.3	Microburst Function Fitting	27
2.4	Results	32
2.4.1	Goodness of Microburst Fits	32
2.4.2	Microburst Analysis	34
2.4.3	Simultaneous Two-frequency Observations	54
2.5	Conclusions	60
3.	ECHOES OF CRAB PULSAR GIANT RADIO PULSES	63
3.1	Introduction	64
3.2	Observations	67
3.3	Microburst Fitting	70
3.4	Results	75
3.4.1	Frequency Dependence	75
3.4.2	Analysis of Microburst Fits	77
3.4.3	Polarization	81
3.5	Discussion	83
3.5.1	Echo Event Lifetimes	84
3.5.2	Echo Broadening	84
3.5.3	Energy and Power Loss in Reflection	85
3.5.4	Echo Frequency Dependence	89
3.5.5	Crab Nebular Wisps as a Location for Reflection	94
3.6	Conclusions	97

4. DISPERSION MEASURE DETERMINATION	99
4.1 Introduction	99
4.2 Observations	101
4.3 Dispersion Measurement Method	106
4.4 Giant Pulse Dispersion Measurements	109
4.4.1 Single Pulse Measurements	110
4.4.2 Pulse-Averaged Measurements	110
4.5 Giant Interpulse Dispersion	117
4.5.1 Dispersion-Frequency Dependence	118
4.5.2 Dispersion-Flux Dependence	124
4.5.3 Dispersion in a Strong Magnetic Field	128
4.6 Conclusions	130
5. CONCLUSIONS	132
5.1 Microsecond-scale Pulse Structure	132
5.2 Echoes in Single Giant Pulses	135
5.3 Dispersion Measure	136
5.4 Pulse Scattering and Alternative Dispersion Laws	137
5.5 Next Steps	139
Bibliography	142

LIST OF TABLES

1.1	Characteristics of the Crab pulsar and nebula	8
1.2	VLA Crab nebula system temperature	21
2.1	Observations for microburst analysis	28
2.2	Interstellar scatter broadening widths	33
2.3	Constant energy curves in Figures 2.3 through 2.13	48
2.4	Characteristic Crab giant pulse widths	51
2.5	Microburst frequency power laws: width and energy	59
3.1	Observations used in Crab giant pulse echo analysis	69
4.1	DM measurements listed by observing session	102
4.1	DM measurements listed by observing session (continued)	103
4.2	Power law model for interpulse dispersion frequency dependence	123
4.3	DM-flux relation for strong wave dispersion	128

LIST OF FIGURES

1.1	Crab average profiles showing main and interpulse	9
1.2	Composite infrared, optical, and x-ray image of Crab nebula . . .	11
2.1	Microburst fitting function	30
2.2	Examples of fitted microbursts	31
2.3	Microburst characteristics for individual observing sessions . . .	36
2.4	Microburst characteristics for individual observing sessions (con- tinued)	37
2.5	Microburst characteristics for individual observing sessions (con- tinued)	38
2.6	Microburst characteristics for individual observing sessions (con- tinued)	39
2.7	Microburst characteristics for individual observing sessions (con- tinued)	40
2.8	Microburst characteristics for individual observing sessions (con- tinued)	41
2.9	Microburst characteristics for individual observing sessions (con- tinued)	42
2.10	Microburst characteristics for individual observing sessions (con- tinued)	43

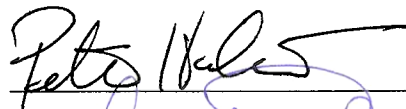
2.11	Microburst characteristics for individual observing sessions (continued)	44
2.12	Microburst characteristics, grouped by frequency	45
2.13	Microburst characteristics, grouped by frequency (continued)	46
2.14	High- versus low-frequency microburst widths of simultaneous two-frequency observations	56
2.15	High- versus low-frequency microburst energies of simultaneous two-frequency observations	57
3.1	Example giant pulses	71
3.2	Average intensity autocorrelations functions	76
3.3	Histogram of the time-of-arrival difference between the primary and echo microbursts	78
3.4	Plot of maximum echo flux, F_{echo} , versus maximum primary flux, F_{primary}	79
3.5	Plot of echo microburst width, W_{echo} , versus primary microburst width, W_{primary}	80
3.6	Plot of echo energy, E_{echo} , versus primary energy, E_{primary}	82
3.7	Dedispersed total intensity and dynamic spectrum of one pulse	86
3.8	Diagram of the direct and reflected ray paths from the pulsar to telescope	91

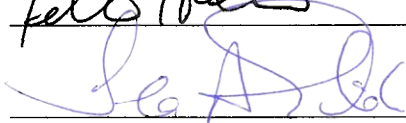
4.1	Dedispersed total intensity and dynamic spectra from one main pulse and one interpulse	105
4.2	Single giant main pulse DM measurements	111
4.3	Single giant interpulse DM measurements	112
4.4	Dispersion measures obtained from giant pulse and average profile observations	113
4.5	Enlargement of two groups of giant pulse DM measurements	115
4.6	Enlargement of another group of giant pulse DM measurements	116
4.7	Giant main pulse and interpulse dispersion measures plotted against average center frequency	120
4.8	Dispersion measure versus average on-pulse flux	127

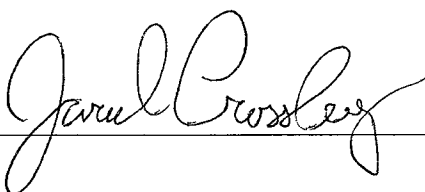
This dissertation is accepted on behalf of the faculty of the Institute by the following committee:



Tim Hankins, Advisor







Jared Harrington Crossley

2008 Dec 16

Date

CHAPTER 1

INTRODUCTION TO THE CRAB PULSAR

1.1 Pulsar Basics

The first pulsating source of radio emission, *pulsar*, was serendipitously discovered by Hewish et al. (1968). The object was unusual for its short and regular pulse period. In the following year more pulsars were discovered; each, like the first, had short and steady pulse periods. Gold (1968) proposed that rotating, magnetized neutron stars were the source of the regular pulsations—that a magnetic field threading a neutron star would imply a corotating plasma extending out to some distance from the star; the corotating plasma density was later quantified by Goldreich & Julian (1969). This relativistic plasma might produce radiation and thus appear as a “rotating beacon”. The rotation period would be very stable due to the high mass density of the star. Remarkably, the model proposed by Gold (1968) less than a year after the first pulsar observation is still the foundation of pulsar theory today, some 40 years later. In the intervening time over 1700 pulsars¹ have been discovered in our galaxy and its globular clusters, and more are being found by archive search programs.

¹Derived from the current number of entries in the Australia Telescope National Facility Pulsar Catalogue (Manchester et al., 2005):
<http://www.atnf.csiro.au/research/pulsar/psrcat/>

Pulsars are produced by some (but not all) supernova explosions. In these supernovæ, the core of the star is compressed by self gravitation to pressures exceeding the electron degeneracy pressure, which results in catastrophic core collapse. When this happens, protons and electrons combine to form a dense star supported by neutron degeneracy. A neutron star is a very small astrophysical object of approximately 10 km radius with a mass of $1.4 M_{\odot} < M_{\text{ns}} < 3 M_{\odot}$.

The short, regular period of pulsation is the defining observational characteristic of pulsars. Apart from this, all other observational characteristics vary among different sources. Although various trends exist within the known pulsar population, the great diversity of observational properties makes studying this group of sources as a whole a challenging endeavor.

Known pulsars have periods, P , ranging from 1 ms to 11 s, and period derivatives, dP/dt , ranging² from -2×10^{-17} to 4×10^{-10} s/s. The rotating beacon pulsar model interprets the period derivative as a change in the rotational speed of the neutron star. This implies a change in the rotational energy of the star. When $dP/dt > 0$ the energy lost by the star is called *spin-down energy*. The pulsar spin-down provides the energy for all radiation of the pulsar system: both pulsed and continuous emission from the pulsar³; particle emission in the form of a pulsar wind; and emission from the surrounding nebula, if it

²A small fraction of pulsars have a decreasing pulse period, often caused by mass accretion from a companion star. These pulsars are thus spinning up rather than down. *Apparent* spin up can occur for pulsars in globular clusters or near the galactic center; in these cases the spin up is a Doppler shift effect rather than an increase in the rotational frequency of the star.

³The thermal emission from the neutron star surface is an exception.

exists. The pulsed radiation observed from the pulsar accounts for only a small fraction of the total spin-down energy⁴. It is a standard assumption of pulsar theory to attribute the spin-down process to magnetic dipole radiation. This assumption then gives the magnetic field strength in terms of P and dP/dt (Carroll & Ostlie, 1996),

$$B = \frac{1}{2\pi R^3 \sin \alpha_B} \left(6 c^3 I P \frac{dP}{dt} \right)^{1/2}, \quad (1.1)$$

where R is stellar radius, α_B is the angle between the magnetic and rotation axes, and I is the neutron star moment of inertia. The magnetic field strength is a fundamental variable used in the pulsar magnetosphere models of the next subsection. It should be noted that some theorists attribute a substantial part of the spin-down energy to the pulsar wind outflow.

1.1.1 A Simple Magnetospheric Model

A simple and useful model of the magnetosphere was described by Goldreich & Julian (1969). In this model, the pulsar is assumed to be composed of a perfectly conducting neutron star containing a magnetic dipole field aligned with the stellar rotation axis. The region exterior to the star is initially assumed to be vacuum. The effect of the rotation of the conducting star is to produce an electric field at the stellar surface with a nonzero radial component. The magnitude of the electric field is a function of the magnetic field strength; most models assume the force of the electric field exceeds the gravitational and

⁴The Crab nebula synchrotron emission is equivalent to 10% to 20% of the pulsar spin-down energy.

surface binding forces, thus pulling particles from the star's surface. Goldreich & Julian (1969) concluded it is likely that pulsar magnetospheres are not vacuum, but are filled with plasma.

Goldreich & Julian (1969) assume the conductivity of the magnetospheric plasma is infinite, that the plasma particle inertia is insignificant, and that the plasma along closed magnetic field lines adjusts itself to create an electric field

$$\mathbf{E} = -(\boldsymbol{\Omega} \times \mathbf{r}) \times \mathbf{B}/c \quad (1.2)$$

where $\boldsymbol{\Omega}$ is the pulsar rotational velocity, and \mathbf{r} is the position of the plasma relative to the center of the star. This electric field allows the charge density to corotate with the star. The charged plasma density necessary to support this electric field is

$$N_e = 7 \times 10^{-2} B_z P^{-1} [\text{cm}^{-3}], \quad (1.3)$$

where B_z is the component of the magnetic field pointing the in the direction of the rotational and magnetic axes. This is known as the Goldreich-Julian, or corotation, charge density, and is used as a canonical value for comparison with more complex models⁵.

Corotation of the magnetic field and plasma is confined by the fact that the tangential speed must be less than the speed of light in vacuum. The surface at which the tangential speed of corotation equals the speed of light in vacuum is called the *light cylinder* of radius $r_{\text{LC}} = cP/2\pi$. Closed magnetic

⁵The Goldreich-Julian density says nothing of the particle number density in the magnetosphere; it is possible that electrons *and* positrons both are present, one particle being more abundant and producing the non-zero charge density.

field lines and corotational plasma cannot extend beyond this radius; in fact relativistic effects near the inside of the light cylinder can greatly distort the dipole field (Arendt & Eilek, 1998). *Open field lines* are those that would, in the absence of rotation, extend beyond the light cylinder; instead, open field lines pass through the light cylinder and take on a toroidal component (Meszaros, 1992). Eventually, the open field lines reconnect to the background magnetic field of the ISM.

A brief review of the common elements of pulsar magnetosphere models is given by (Eilek et al., 2002); I summarize these common elements here. The regions where open field lines intersect the neutron star surface are called the *polar caps*; extending radially outward from the polar caps, the open field line regions form *polar flux tubes*, which are believed to be important to the pulsed emission we observe. Within a polar flux tube and near to the stellar surface the plasma density is believed to differ from the Goldreich-Julian density [for example see Ruderman & Sutherland (1975)]. This density variation results in a strong electric field that accelerates charges; the charges are either pulled from the stellar surface or are generated by pair production from high-energy background photons. These particles quickly obtain relativistic energies at which point they radiate high-energy photons. If the radiation occurs close enough to the polar cap, the photons will pair produce a “second generation” of particles; these second generation particles are subsequently accelerated producing more high-energy photons. A pair cascade continues, moving outward from the stellar surface until the particle energies decrease below the pair generation threshold and the polar flux tube electric field is quenched.

The energetic particles produced by the pair cascade continue moving outward from the magnetic pole with relativistic velocity. It is this energetic, outward-moving plasma that is believed to be responsible first for the pulsed emission and later for the pulsar wind.

For the Crab pulsar, single pulses contain *components* of emission that vary in duration from fractions of a nanosecond to (possibly) many microseconds⁶. These components are believed to be radiation from variably-sized plasma groups. Careful study of components will likely give insight into emission physics (Crab microsecond-scale components are the subject of Chapter 2).

How the plasma energy is converted to electromagnetic radiation is not well understood; several models exist but without consensus among pulsar theorists (Eilek et al., 2002). Ruderman & Sutherland (1975) describe pulse emission as resulting from “sparks” near the polar cap that generate narrow, relativistically beamed plasma outflow; the plasma emits curvature radiation as it moves out along open field lines. Petrova (2004) describes pulsar radiation as stimulated emission; a maser process in which small variations in the local physical conditions produce large variations in emitted power. Several authors (Lyutikov, 2003, 2006; Shekard et al., 2009) have drawn an analogy between pulsar emission and solar flares; magnetic reconnection is the direct radiating mechanism.

⁶Measuring the longest duration components is complicated by pulse scattering in the interstellar medium; strong short-duration components are sometimes observed despite interstellar scattering.

1.2 The Crab Pulsar and Nebula

1.2.1 Crab Pulsar

One of the more outstanding sources within the pulsar population is the Crab pulsar. The Crab pulsar is a young, isolated star residing approximately in the center of the Crab nebula supernova remnant, 2 kpc from Earth. The supernova that created the Crab pulsar was observed in 1054 A.D. by ancient astronomers. Some observational and derived characteristics of the Crab pulsar and nebula are contained in Table 1.1. The Crab pulsar has been observed at frequencies as low as 23 MHz (Popov et al., 2006), at energies as high as several TeV (γ -rays), and has been observed at infra-red, optical, ultraviolet, and X-ray wavelengths. The Crab pulsar exhibits two strong pulses for each rotational period, the *main pulse* and *interpulse*. Figure 1.1 shows average profiles of the full Crab rotational period across a wide range in frequency; the prominent main and interpulse are highlighted with vertical dashed lines⁷. It is conventionally believed that the main pulse and interpulse originate from plasma outflows above the two magnetic poles of the star. As shown in Table 1.1, the main pulse and interpulse are not separated by 180° of rotational phase; the main-to-interpulse phase difference is between 135° and 145° ; the frequency dependence of the phase difference is clearly seen in Figure 1.1. Neither the cause of the $< 180^\circ$ phase difference, nor the cause of the frequency dependence is precisely known. It may be that the magnetic field is not a dipole, or

⁷Other pulsed emission includes a low frequency main pulse precursor and two components at high radio frequency (Moffett, 1997; Moffett & Hankins, 1996). This emission, which has a narrower bandwidth than the main pulse and interpulse, is not discussed in this study.

Table 1.1: Characteristics of the Crab Pulsar and Nebula

Period	0.0330 s
Period derivative	4.23×10^{13} s/s
Distance ¹	2 ± 0.5 kpc
Magnetic Field Strength	3.78×10^{12} G
Light cylinder radius	1600 km
Main-to-interpulse separation ²	135 to 145°
Spin-down energy ³	5×10^{38} erg/s
Nebula size	4×3 kpc

¹Cordes & Lazio (2002)

²Moffett & Hankins (1996)

³Bietenholz et al. (2004)

it may be that both pulses originate above one magnetic pole very high in the magnetosphere where the field lines direct the emission in different directions.

Main pulse and interpulse flux magnitudes each vary in different ways with frequency. Furthermore, the flux in each pulse is strongly variable from one rotational period to the next⁸; stronger pulses are less frequent than weaker pulses. Pulses for which the maximum flux exceeds the average integrated pulse flux by more than a factor of a few are called *giant pulses*. The Crab pulsar is one of only seven pulsars for which giant pulses have been claimed (Soglasnov et al., 2004); only in the Crab pulsar and the millisecond pulsar do giant pulses occur often enough to allow for a statistical analysis (Popov & Stappers, 2007). The large flux of giant pulses allow for high-time-resolution observations, like those reported here.

⁸Note that pulse flux magnitude is dependent on time resolution; higher time resolution observations record pulses with higher flux.

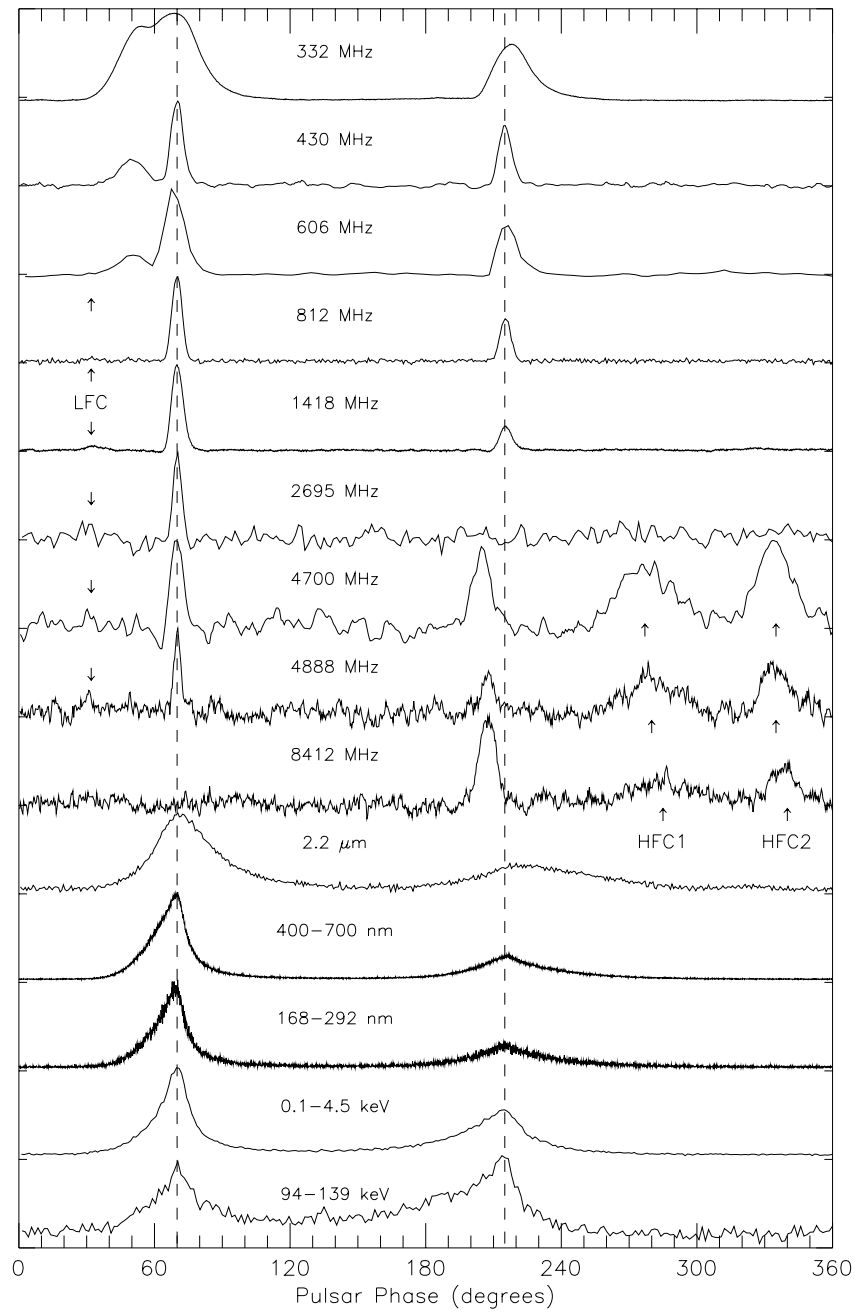


Figure 1.1: Crab average profiles recorded over a wide range of frequencies; from Moffett & Hankins (1996). The vertical dashed lines show the main pulse (left) and interpulse (right).

1.2.2 Crab Nebula

The Crab nebula is a supernova remnant that appears on the sky as a roughly oval shape with semi-major and semi-minor axes of approximately 7 and 5 arcminutes, respectively, at 5 GHz; at 2 kpc distance, this corresponds to linear dimensions of 4 and 3 kpc, respectively. The nebular radio emission is predominantly synchrotron and has a power law spectrum, $F \propto \nu^\alpha$ with spectral index $\alpha = -0.299$ between 1 and 35 GHz (Baars et al., 1977).

The Crab nebula is expanding at an accelerating rate. Observations of synchrotron radiation reveal the presence of relativistic particles and a magnetic field. The power required to accelerate expansion of the nebula, relativistic particles, and magnetic field is equal to the rotational power loss of the neutron star, $\sim 5 \times 10^{38} \text{ erg s}^{-1}$ (Carroll & Ostlie, 1996). The rotational spin-down of the star is the power supply for the whole nebula. The mechanisms by which energy is transferred from the star to the nebula are assumed to be magnetic dipole radiation and magnetic drag of the charged particles from the pulsar wind.

A composite image of the Crab nebula using infrared, optical, and X-ray observations is shown in Figure 1.2. The nebula has an intricate spatial and spectral structure. Closest to the pulsar are knot-like structures visible in optical and wisp-like structures visible in radio and optical. The inner knot appears to be as close as 1500 AU to the pulsar (Hester et al., 1995). The wisps evolve on timescales of days, moving outward from the star. The knots and wisps are believed to be produced by the pulsar wind shock—the interface between the pulsar and the surrounding nebula.



Figure 1.2: Composite image of Crab nebula combining infrared (shown here as red), optical (green), and X-ray (blue). The white dot at the center of the X-ray emission is the pulsar. The sides of the image are 7.8 arcminutes in length. This image was obtained from the Chandra X-ray Observatory web site at <http://chandra.harvard.edu/photo/2006/crab/>. This image is credited to the following organizations and authors: NASA, CXC, ASU, J. Hester et al. (X-ray image); NASA, ESA, ASU, J. Hester & A. Loll (optical image); NASA, JPL-Caltech, Univ. Minn., R. Gehrz (infrared image).

Coincident with the wisps is the inner edge of a torus of high energy plasma visible most prominently in X-rays (Weisskopf et al., 2000) and concentric about the pulsar. A jet, also visible in X-rays, extends outward from the pulsar, perpendicular to the torus. The jet is aligned with the elongated dimension of the optical and radio nebula. The X-ray torus and jet are both visible in the composite image of Figure 1.2.

The optical nebula is approximately centered on the pulsar and is almost twice as large as the X-ray torus and jet. Near its outer boundary lie chemically rich filaments produced by the supernova. The radio nebula extends further beyond the bounds of the optical nebula, and is a synchrotron radiator at lower frequencies.

1.3 Propagation Effects

Investigation of pulsar emission physics is complicated by the fact that the emitted radiation interacts with charged particles between the emitter and Earth. The important effects of this interaction, with regard to the observations and analysis presented in this work, are pulse dispersion, scatter broadening, and scintillation.

1.3.1 Pulse Dispersion

The interstellar medium (ISM) is filled with matter ionized by surrounding stars. From the Lorentz force law, an electron in the ISM will have an equation of motion

$$m \frac{d\mathbf{v}}{dt} = -q\mathbf{E} - \frac{q}{c} \mathbf{v} \times (\mathbf{B} + \mathbf{B}_0),$$

where m , \mathbf{v} , and q are the electron mass, velocity, and charge, respectively. \mathbf{E} and \mathbf{B} are the propagating electric and magnetic (EM) field and \mathbf{B}_0 is the background magnetic field. Dispersion is one effect of the propagating EM wave interacting with the ionized particles of the ISM; the mass of the particles results in an inertial resistance to the perturbation of the EM field. More quantitatively, the dispersion relation of cold, i.e. non-relativistic⁹, isotropic plasma is (Rybicki & Lightman, 1979)

$$\omega^2 = \omega_p^2 + k^2 c^2, \quad (1.4)$$

where ω and k are the angular frequency¹⁰ and wavenumber of radiation propagating through the plasma, and the plasma frequency is

$$\omega_p = \sqrt{4\pi N_e q^2 / m}. \quad (1.5)$$

Here, N_e , q , and m are the electron number density, electron charge, and electron mass, respectively. The dielectric constant, ϵ_r , for an isotropic plasma, is related to the index of refraction¹¹,

$$n_r = \sqrt{\epsilon_r} = \sqrt{1 - \frac{\omega_p^2}{\omega^2}}. \quad (1.6)$$

The effect of a medium with $n_r < 1$ can be quite significant for pulsating radio sources.

⁹For a plasma in thermal equilibrium, the root-mean-square electron velocity is $v_{\text{rms}} = \sqrt{3k_B T / m_e}$. In the non-relativistic limit, $v_{\text{rms}} \ll c$ implies $T \ll 10^9$ K. The temperatures of the vast majority of the ISM in our galaxy satisfy this inequality.

¹⁰The normal wave frequency, ν , relates to ω by $\omega = 2\pi\nu$.

¹¹For an isotropic plasma, Maxwell's equations reveal that $\epsilon_r = c^2 k^2 / \omega^2$ (Rybicki & Lightman, 1979). The index of refraction is defined as $n_r \equiv c / v_{\text{ph}} = kc / \omega$, where v_{ph} is the phase velocity. From here it is clear that $n_r = \sqrt{\epsilon_r}$.

The frequency dependence of n_r causes the low frequency radiation to propagate more slowly through the ISM than high frequency radiation. The propagation time for radiation to traverse a distance L in the ISM is

$$t_p(\omega) = \int_0^L \frac{1}{v_g} dr, \quad (1.7)$$

where $v_g = d\omega/dk$ is the EM wave group velocity. The ISM electron density is $\sim 0.03 \text{ cm}^{-3}$, which gives a plasma frequency $\omega_p \sim 10 \text{ kHz}$. Since most observations, including those presented in this work, satisfy $\omega \gg \omega_p$, the group velocity can be written in the form

$$\frac{1}{v_g} \approx \frac{1}{c} \left(1 + \frac{\omega_p^2}{2\omega^2} \right).$$

Equation (1.7) then reduces to

$$t_p(\omega) = \frac{L}{c} + \frac{2\pi q^2}{cm\omega^2} \text{DM}, \quad (1.8)$$

where $\text{DM} \equiv \int_0^L N_e dr$ is the dispersion measure (conventionally written in units of [pc cm^{-3}]), and r is length along the light ray path. For the Crab pulsar $\text{DM} \sim 57 \text{ pc cm}^{-3}$. Notice that the first term on the right hand side of Equation (1.8) is the propagation time in vacuum, and the second term is the additional propagation time due to the ionized medium.

1.3.2 Scatter Broadening

Another effect of pulse propagation through ionized matter is scatter broadening. Scatter broadening has been analyzed in extensive detail [see, for example, Lee & Jokipii (1975)]. I present here a simple model that describes the basic frequency dependence of scatter broadening.

Scattering of pulsar signals is caused by fluctuations in the index of refraction between Earth and the pulsar. If the fluctuations have a scale size a , then the wavefront passing through the fluctuation will undergo a phase change

$$\Delta\phi \sim \Delta n_r \frac{\omega a}{c} = \Delta n_r \frac{2\pi a}{\lambda} \quad (1.9)$$

For a cold, isotropic plasma equations (1.6) and (1.5) show that the index of refraction relates to the electron number density as

$$\Delta n_r \approx -\frac{2\pi q^2}{\omega^2 m} \Delta N_e, \quad (1.10)$$

where I have assumed that $\omega \gg \omega_p$. Combining equations (1.9) and (1.10) gives

$$\Delta\phi = \Delta N_e \lambda a r_e, \quad (1.11)$$

where $r_e = q^2/mc^2$ is the classical electron radius.

The large amplitude fluctuations seen in pulsar signals are interpreted as evidence that the ISM causes strong scattering (Scheuer, 1968) defined by $\Delta\phi > \pi$. For strong scattering, the angle over which the wavefront scatters is

$$\theta_s = \frac{\Delta\phi \lambda}{2\pi a} \quad (1.12)$$

Combining equations (1.11) and (1.12) gives

$$\theta_s \propto \lambda^2. \quad (1.13)$$

It can be shown geometrically¹² that the path length difference between the direct Earth-pulsar line of sight and the largest-angle scattered path

¹²This same approximation is performed in a different context, and in slightly more detail, in Chapter 3; see equation (3.7) and Figure 3.8.

is proportional to θ_s^2 . The propagation time is proportional to the path length and therefore the pulse is broadened by time,

$$\tau \propto \theta_s^2 \propto \lambda^4 \tag{1.14}$$

So we find for a cold, isotropic plasma the pulse will be broadened roughly as a function of λ^4 .

1.3.3 Interstellar Scintillation

The study of interstellar scintillation is vast; see Rickett (1977, 1990) for some review. For the work reported here, the intricacies of scintillation phenomena are not important, but a simple understanding will help to elucidate the analysis to come.

Pulse scattering (either in the form of diffraction or refraction) between emitter and receiver not only broadens the pulse temporally, it also produces interference when the scattered signals arrive at the telescope with different phases. The phase differences produce a diffraction pattern in the observing plane. The diffraction pattern varies with frequency and time; frequency variation is a result of the frequency-dependent index of refraction of the scattering medium; time variation is a result of the relative motion of the Earth-pulsar sight line and the scattering medium. The observational effects of the diffraction pattern are called *scintillation*.

If a scattered pulsar signal arrives at a telescope over a range of time τ , the resulting interference pattern is correlated over a bandwidth given by

the Fourier transform relation (Backer, 1988),

$$B_s = \frac{1}{2\pi\tau}. \quad (1.15)$$

Invoking the simple scattering model of § 1.3.2 we can infer that the scintillation bandwidth varies with frequency as

$$B_s \propto \lambda^{-4} \propto \nu^4 \quad (1.16)$$

This steep frequency dependence has a powerful effect on pulsar observations. At low radio frequencies, many scintillation bandwidths may fit within the receiver bandwidth, resulting in a continual sensitivity to pulsar flux. At higher frequencies, the scintillation bandwidth may exceed the receiver bandwidth and result in an apparent null over long periods of time when the receiving center frequency lies in a scintillation minimum. At still higher frequencies (> 20 GHz) the effects of scintillation decrease until eventually the effects disappear completely.

1.4 Signal Processing

The observational time resolution of individual pulses is fundamentally limited by several factors: characteristics of the observing instrumentation, pulse dispersion broadening, and pulse scattering. Pulse dispersion broadening is a systematic and frequency dependent process that can be removed from the data in one of two ways, discussed below. Pulse scattering is a random process; despite its well defined frequency dependence, it cannot be removed from the data.

The available bandwidth of the telescope and the sampling rate of the voltage recording instrument impact the observational time resolution. The product of the best possible time resolution, Δt , and total bandwidth, $\Delta\nu$, of an observed signal is constant according to the uncertainty relation,

$$\Delta t \Delta\nu = 1.$$

Thus, to obtain small time resolution requires large bandwidth. Furthermore, for a given bandwidth, the *sampling theorem* states that all signal information within the band can be obtained by sampling at an interval $\Delta t = 1/(2\Delta\nu)$, the Nyquist rate. Sampling slower than the Nyquist rate, known as *undersampling*, results in a decrease in time resolution, a loss of the highest frequency signal fluctuations, and an overestimation of the power at lower frequencies [see Bracewell (2000) for a discussion]. Given a 2-GHz bandwidth signal, the Nyquist rate is $\Delta t = 0.25$ ns; for 2-bit sampling, a 1 second observation will produce 1 gigabyte of data. Thus, time resolution is limited by the memory size and the data storage rate of the recording instrumentation.

In addition to allowing for small time resolution, large observing bandwidth is desirable because it increases the signal-to-noise ratio of the pulsar after dedispersion according to the radiometer equation,

$$\frac{\Delta T}{T} = \frac{1}{\sqrt{\Delta\nu \Delta t}}, \quad (1.17)$$

where T is the system temperature and ΔT is the root-mean-square fluctuation of the system temperature.

1.4.1 Dedispersion

Dispersion broadening can be removed from pulsar observations by two mechanisms: incoherent dedispersion and coherent dedispersion. Incoherent dedispersion utilizes a filter bank spread over the observing band. Signals in each channel of the filter bank can be detected, delayed appropriately to remove most of the effect of dispersion, and then added together to improve the signal to noise ratio. What remains is the dispersion broadening across the individual channel bandwidths.

Coherent dedispersion, developed by Hankins (1971) and Hankins & Rickett (1975), can fully remove dispersive broadening. The process is as follows. A pulsar signal, $S(\nu)$, propagating through the ISM undergoes a change of phase described by

$$S(\nu) \rightarrow S(\nu)e^{ikL},$$

where L is the distance from the pulsar and k is the wavenumber of the signal in the ISM given by equation (1.4). In signal processing terminology, the exponential factor $H(\nu) \equiv e^{ikL}$ is the *transfer function* of the ISM. To remove the effect of dispersion, all that need be done is multiply the Fourier transform of the pulsar signal by the inverse of the ISM transfer function. An approximation to the inverse function is obtained by first expanding k in a Taylor series about the observing center frequency, ν_0 , then shifting the frequency to baseband. For bandwidths that are small relative to ν_0 , the inverse becomes (Hankins & Rickett, 1975),

$$H^{-1}(\nu + \nu_0) = \exp \left[\frac{i2\pi D\nu^2}{\nu_0^2(\nu_0 + \nu)} \right], \quad \nu \ll \nu_0.$$

The *dispersion coefficient*, D , can be written in terms of the dispersion measure,

$$DM [\text{pc cm}^{-3}] = 2.410000 \times 10^{-16} (D [\text{sec Hz}^2]).$$

Dedispersion of the giant pulses in this work was performed as follows: the giant pulses were initially recorded as a voltage time series. The time series were Fourier transformed to the frequency domain and multiplied by the inverse ISM transfer function. The products were then inverse Fourier transformed back to the time domain and stored for subsequent analysis.

1.5 Observations

Crab giant radio pulse observations between 1993 and 1999, utilized the Very Large Array (VLA) and the high-time-resolution observing system described by Moffett (1997). In total, observations were recorded on 24 different days, and in various VLA array configurations. The array was used in phased-array mode, where individual antenna delays are set in real time to restore the original wave front. The interferometric nature of the VLA is advantageous for Crab pulsar observations because, even in the most compact D-array configuration, the small synthesized beam resolves out most of the structure of the Crab nebula, thus increasing sensitivity to pulsar signals. To avoid recording radio sources other than the pulsar, the software package TEMPO was used in prediction mode along with the Crab Pulsar ephemeris published by Jodrell Bank Observatory to create a pulsar timing model. The model was used to set a period-synchronous gate on either the main pulse or interpulse. With the gate activated, the cumulative VLA signal was square-law detected and monitored for power exceeding a threshold set at observing time. If the threshold

Table 1.2: VLA Crab Nebula System Temperature

Observing Frequency (GHz)	T_{sys} (K)
0.333	200
1 – 6	140
8 – 9	96.5

was exceeded while the gate was on, a LeCroy oscilloscope was triggered to sample two orthogonal circular polarization signals at a rate of 100 MHz. The signals were then transferred to disk for subsequent off-line coherent dedispersion (Hankins, 1971). During the transfer time, 10-30 s, the data acquisition was disabled, and no pulses could be captured. Pulses recorded at the VLA were flux calibrated assuming a system temperature, T_{sys} , given in Table 1.2. The change in T_{sys} with frequency is partially due to the spectral index of the nebula (see above in this chapter) and partially to the VLA receivers (the 0.3 GHz receivers are not cooled and therefore have a higher T_{sys}).

Observations recorded in 2004 and 2005 utilize the Arecibo radio telescope and the $P\mu\eta$ system, described by Kern (2004). These observations were taken on 29 different days. The large observing bandwidths available in the 5- and 9-GHz receivers at Arecibo allow for better time resolution despite the decrease in sensitivity due to observing the radio-bright Crab nebula with a single-dish telescope.

Unlike the earlier high-time-resolution observing system, the $P\mu\eta$ system allows for creating a real-time pulsar average profile. At the right frequencies, and when the pulsar is visible, both the Crab main and interpulse are present in the average profile. Gates can be set on both pulses, and giant

pulses detected in either pulse can be captured. At Arecibo, pulses were sampled and captured with a Tektronix oscilloscope at the Nyquist rate.

1.5.1 Capturing Giant Pulses: On-pulse Energy Threshold

The P $\mu\eta$ system includes hardware designed to capture giant pulses while ignoring weaker pulses. When a giant pulse is detected, the system signals the oscilloscope to write its memory contents to disk, thus saving the giant pulse record. The process of giant pulse detection is as follows.

The raw voltage signal from the telescope is square-law detected, $y(t) = x^2(t)$, and then smoothed by a resistor-capacitor time constant low-pass filter. The smoothing time is $\sim 2\tau_{RC}$, where τ_{RC} is the time constant (Kraus, 1986); the time constant is set at observing time such that $2\tau_{RC}$ is approximately the sweep time of the pulse across the bandwidth of the channel used for the detector, $\Delta\nu_d$. The output of this filter is then the square-law detected signal convolved with the resistor-capacitor circuit response,

$$z(t) = y(t) * e^{-t/\tau_{RC}}. \quad (1.18)$$

The signal $z(t)$ then passes through another capacitor circuit which removes the DC component; this DC component is effectively the running mean of $z(t)$ taken over the previous ~ 3 seconds.

$$u(t) = z(t) - \langle z(t) \rangle_{3s} \quad (1.19)$$

Next, the root mean square of $u(t)$ is computed, $\sigma_{u(t)}$. If we assume that giant pulses occur no more than once per 3 seconds, then prior to a giant pulse $\sigma_{u(t)}$ is approximately the standard deviation of the off-pulse noise. Subsequently,

another resistor-capacitor circuit is used to compute the running mean of the standard deviation over the previous 3 seconds, $\langle\sigma_{u(t)}\rangle_{3s}$. With this information, I can rewrite the radiometer equation [equation (1.17)] for the giant pulse detector,

$$\langle\sigma_{u(t)}\rangle_{3s} = \frac{\langle z(t)\rangle_{3s}}{\sqrt{\Delta\nu_d 2\tau_{RC}}}, \quad (1.20)$$

where $2\tau_{RC}$ is the effective sampling interval¹³ of the smoothed signal, $z(t)$.

The condition for detecting a giant pulse is,

$$u(t) > n \langle\sigma_{u(t)}\rangle_{3s}, \quad (1.21)$$

where the coefficient n is set at observing time, generally to $n = 7$.

1.6 This Study

The work presented in this study divides into three parts. Chapter 2 presents an analysis of microsecond-scale structure in observations of Crab giant pulses recorded with the Very Large Array. Chapter 3 focuses on a pulse-echo-like phenomenon observed on two days of VLA observations. Chapter 4 uses data recorded at the Arecibo radio telescope to analyze the dispersion measure of single Crab giant pulses. Finally, in chapter 5 all the results of this work are reviewed and their implications for astronomical research are discussed.

¹³The sampling interval in the denominator of equation (1.20) is $2\tau_{RC}$. This is the sampling interval of the signal, $z(t)$, from which the standard deviation, $\langle\sigma_{u(t)}\rangle_{3s}$, and mean, $\langle z(t)\rangle_{3s}$, are computed. The standard deviation and mean are running measurements taken over a period of about 3 seconds, but that does not change the sampling interval of the signal from which they are computed.

CHAPTER 2

MICROSECOND-SCALE SUBPULSE CHARACTERISTICS

2.1 Introduction

At radio frequencies, the Crab pulsar main and interpulses consist of superimposed components (or “bursts”) (Sallmen et al., 1999). Properties of Crab components are highly variable. For example, the number of components per pulse varies from one period to the next; the component rotational phase, energy content, and width vary between consecutive periods and even within single pulses. Component rotational phase variability obscures all but the strongest components when the pulsar is observed using the traditional technique of pulse-averaging. Fortunately, the brightness of Crab giant pulses makes it possible to record high-time-resolution single pulses wherein the components are observed well above the noise. Components have been detected with widths of $10\ \mu\text{s}$ (Sallmen et al., 1999), 4 to $65\ \mu\text{s}$ (Popov & Stappers, 2007), and $0.4\ \text{ns}$ (Hankins & Eilek, 2007). In this thesis I differentiate the component timescales with the terms “*microburst*” and “*nanoshot*”, denoting a component with width on the order of microseconds or nanoseconds respectively. Since the data presented in this chapter has microsecond time resolution, I focus my study on microbursts.

Pulse microbursts have long been known to exist, and were observed in single pulses very soon after Hewish and Bell’s discovery of the first pulsar

(Craft et al., 1968). There are a few theoretical models of pulse microbursts. First, is the narrow spark or plasma column model, which was introduced by Ruderman & Sutherland (1975); in this model the emitting regions are narrow and relativistically beamed. Second, Petrova (2004) has proposed that pulse microburst emission is stimulated—a maser process; the emission power of a maser goes as e^X , and X accounts for the variable physical conditions of the medium; small variations in the physical conditions produce large variations in power, accounting for the vast range of microburst flux. Third, is a solar flare-like model wherein energy is released from magnetic field reconnection (Lyutikov, 2003, 2006; Sheckard et al., 2009).

Microbursts represent a mid-scale of the Crab pulsar emission region. Existing on the order of $10 \mu\text{s}$, I can infer a source size $c \Delta t = 3 \text{ km}$; much larger than the 2-ns (implying a source size of 60 cm) bursts observed by Hankins et al. (2003) or the 0.4-ns (12 cm) nanoshots found by Hankins & Eilek (2007) but much smaller than the magnetosphere radius $r_{\text{LC}} = cP/2\pi \sim 1600 \text{ km}$. It is possible that microbursts represent variably-sized groups of nanoshots (Hankins & Eilek, 2007; Hankins et al., 2003; Cordes, 1976). Whatever the nature of their sources, microbursts are part of the pulsar emission process, and their characteristics provide important constraints for current and future emission models.

In this chapter I report on a study of the characteristics of microbursts in Crab main pulse observations made at the Very Large Array. In § 2.2 I describe the observations used; in § 2.3 I describe the functional fitting of microbursts; in § 2.4 I describe the results of an analysis of fitted microbursts;

and in § 2.5 I summarize the chapter.

2.2 Observations

In this chapter, I utilize observations recorded with the Very Large Array (VLA) between 1993 (MJD 49080) and 1999 (MJD 51218)¹. The observing method used is described in § 1.5. I limit my study to observing sessions in which no fewer than 27 main pulses were captured². Most of my VLA observing sessions monitored and recorded main pulses only. Although interpulses were recorded in some VLA sessions, these data are sufficiently few that I choose to exclude them from this study³.

Table 2.1 lists 27 observing sessions used in this chapter. Pulses were observed using four VLA receivers at frequencies of 0.33, 1.2-1.7, 4.5-5.0, and 8.4 GHz; most observations were made with 1.2-1.7 or 4.5-5.0 GHz receivers. All observations were made with 0.05-GHz bandwidth, with two exceptions: the lowest frequency observations allowed only 0.005-GHz bandwidth at 0.33-GHz center frequency⁴; a simultaneous two-frequency observation at 1.2 and 1.7 GHz used 0.025-GHz bandwidth at each frequency. Table 4.1 also lists:

¹I limit this microburst study to VLA observations; Arecibo observations, discussed in Chapter 4, were made using larger bandwidths and higher radio frequencies, which I expect to affect pulse microburst characteristics.

²The number 27 was chosen, after examining the data, to include a useful and interesting ensemble of observing sessions but to avoid observing sessions with statistically insignificant numbers of pulses. Some observing sessions present in Chapters 3 and 4 are not present in this chapter because they contain too few pulses.

³A study of interpulse microbursts or nanoshots should include a statistically significant sample of interpulses. Interpulse and main pulse analyses should be performed separately; based on the dispersion results in Chapter 4 and on a recent study by Hankins & Eilek (2007), the interpulse is, at least in some respects, very different from the main pulse.

⁴The 0.3-GHz VLA receiver has a total bandwidth of only 0.04 GHz.

the number of pulses and microbursts fitted (see §2.3), the post-processing time resolution, the span of time between first and last recorded pulse, and the MJD for each observing session. In total, the observations reported here include 1610 Crab pulses (consisting of 3058 fitted microbursts) observed over 914 non-consecutive minutes of telescope time.

Of the 27 observing sessions listed in Table 2.1, 14 comprise simultaneous two-frequency observations in which pulses were recorded at two non-overlapping passbands. These 7 pairs of observing sessions can be identified by the superscripts on the first column of Table 2.1; corresponding superscripts denote simultaneously recorded data. By observing two frequency bands simultaneously, the frequency structure of single giant pulses can be studied across a wider span of frequency than is possible with single-frequency observing at the VLA.

It should be noted that pulse records at 0.33-GHz center frequency extend over 36 ms, and thus capture an entire Crab pulsar rotational period. A small number of these records contain giant main pulses *and* giant interpulses within the same rotational period. Also visible in a small number of 0.33-GHz pulse records is emission from the main pulse precursor, first observed by Rankin et al. (1970). For the main pulse study to follow, I have intentionally ignored the interpulse and precursor emissions.

2.3 Microburst Function Fitting

To analyze the properties of main pulse microbursts, I fit microbursts with a function having a fast-rise-slow-decay shape. Pulse processing, including

Table 2.1: Observations for microburst Analysis

Center Freq (GHz)	BW (GHz)	# GPs Fitted	# Microbursts Fitted	Time Res (μ s)	Time Span (min)	MJD
0.3339	0.0050	49	49	20	18	49406
1.2401 ^a	0.0250	38	61	1.6	55	51218
1.3851 ^b	0.0500	27	52	0.8	41	51159
1.3851 ^c	0.0500	52	97	0.8	20	51174
1.4149	0.0500	61	142	0.8	26	49399
1.4351	0.0500	52	95	0.8	14	51137
1.4351	0.0500	50	131	0.8	11	51159
1.4351	0.0500	54	123	0.8	15	51167
1.4351	0.0500	51	119	0.8	10	51174
1.4351 ^d	0.0500	34	81	0.8	13	51174
1.4351	0.0500	51	81	0.8	22	51214
1.4351	0.0500	203	259	0.8	59	50193
1.4351	0.0500	103	200	0.8	84	50224
1.4351 ^e	0.0500	34	69	0.8	30	50368
1.4351 ^f	0.0500	61	108	0.8	170	50370
1.6649 ^b	0.0500	70	145	0.8	41	51159
1.7141 ^a	0.0250	38	63	1.6	55	51218
1.7149 ^c	0.0500	52	101	0.8	20	51174
1.7149 ^d	0.0500	34	74	0.8	13	51174
4.5351 ^g	0.0500	46	96	0.2	41	51167
4.8851	0.0500	51	104	0.2	57	49080
4.8851 ^e	0.0500	40	79	0.2	31	50368
4.8851 ^f	0.0500	62	117	0.2	170	50370
4.8851	0.0500	34	54	0.2	16	51112
4.8851	0.0500	152	312	0.2	126	51112
4.9851 ^g	0.0500	52	145	0.2	42	51167
8.4149	0.0500	59	89	0.2	84	49086

Superscript pairs denote simultaneous 2-frequency observing sessions.

smoothing, decimation, and fitting, is performed off-line⁵.

After coherent dedispersion (Hankins, 1971), the off-pulse mean intensity is calculated and subtracted from each individual pulse. Microbursts are fit using a sum of fast-rise-slow-decay functions,

$$F(t) = \sum_{i=1}^n F_i(t) = \sum_{i=1}^n A_i(t - t_{0i}) e^{-(t-t_{0i})/\tau_i}. \quad (2.1)$$

This sum, $F(t)$, was also used by Sallmen et al. (1999), and is a modification of the best-fit function found by Rankin et al. (1970) for pulses scatter broadened by propagation through the turbulent ISM. An example of $F_i(t)$ is shown in Figure 2.1. For each microburst, the three parameters, A_i , t_{0i} , and τ_i , are set by initial estimates. χ^2 minimization is then used to obtain the best fit of $F(t; A_i, t_{0i}, \tau_i)$ (Press et al., 1992). I choose the number of terms, $1 \leq n \leq 6$, such that the uncertainties in the function parameters are small and the pulse residuals are close to being normally distributed about zero with standard deviation $\sigma_F(t)$; this uncertainty is given by the radiometer equation:

$$\sigma_F(t) \equiv \begin{cases} [F(t) + F_{\text{off}}]/\sqrt{\Delta\nu \Delta t} & , \quad t \in \text{on-pulse region} \\ \sigma_{\text{off}} = F_{\text{off}}/\sqrt{\Delta\nu \Delta t} & , \quad t \in \text{off-pulse region} \end{cases}, \quad (2.2)$$

where $\Delta\nu$ is the observing bandwidth, Δt is the smoothed time resolution, F_{off} is the off-pulse mean flux. For χ^2 minimization, the uncertainty of each data point is set to the off-pulse standard deviation. Finally, all fits are assessed by eye to avoid non-physical χ^2 minima.

Once good fits are obtained, I analyze the microburst properties by making use of the fitted-function parameters. In equation (2.1) a microburst

⁵This microburst fitting method is also described in § 3.3.

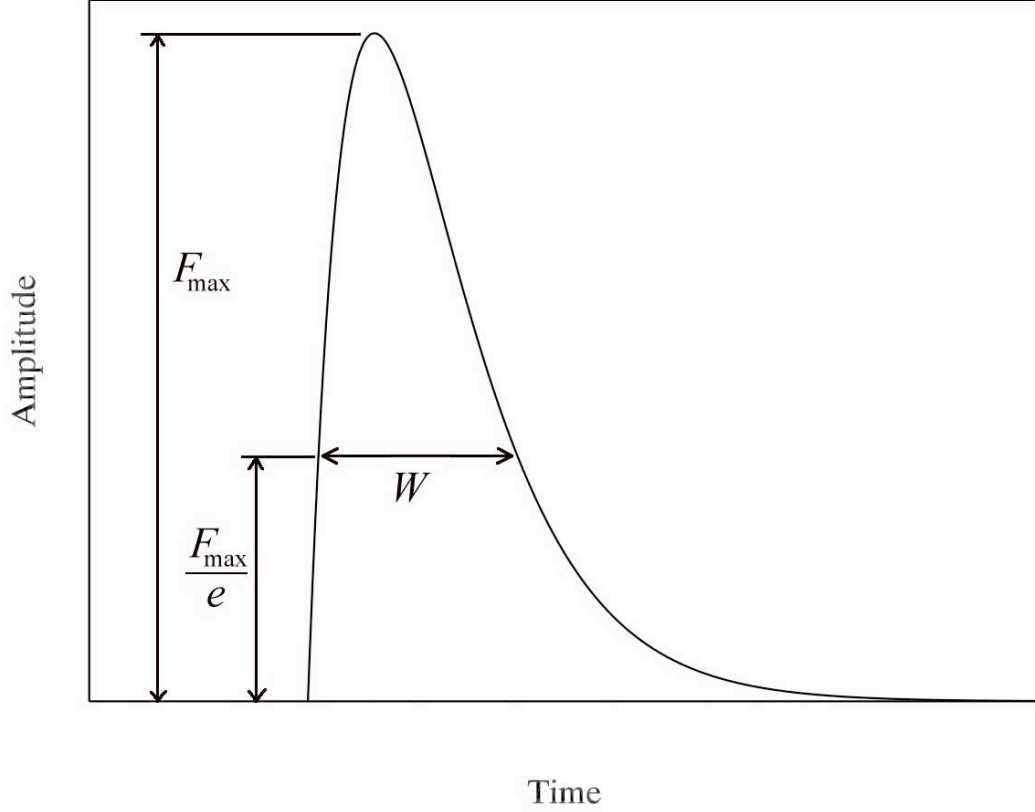


Figure 2.1: Plot of microburst fitting function. The function maximum is labeled F_{\max} . The function width, W , is defined as the width at an amplitude of F_{\max}/e . In practice, amplitude has units of flux density.

(term i) has maximum flux $(F_{\max})_i = A_i \tau_i e^{-1}$ at time $t_{\text{TOA } i} = t_{0i} + \tau_i$; the microburst width is $W_i = 3\tau_i$ [defined as the length of time that the flux exceeds $(F_{\max})_i e^{-1}$]; the total microburst energy is $E_i = A_i \tau_i^2 = (F_{\max})_i W_i e/3$. $(F_{\max})_i$ and W_i are shown graphically in Figure 2.1.

Examples of fitted microbursts are shown in Figure 2.2 (see more examples in Figure 3.1). Individual terms [see Equation (2.1)] are drawn with dashed lines; the sum of all terms, $F(t)$, is drawn with a solid line. The pulse

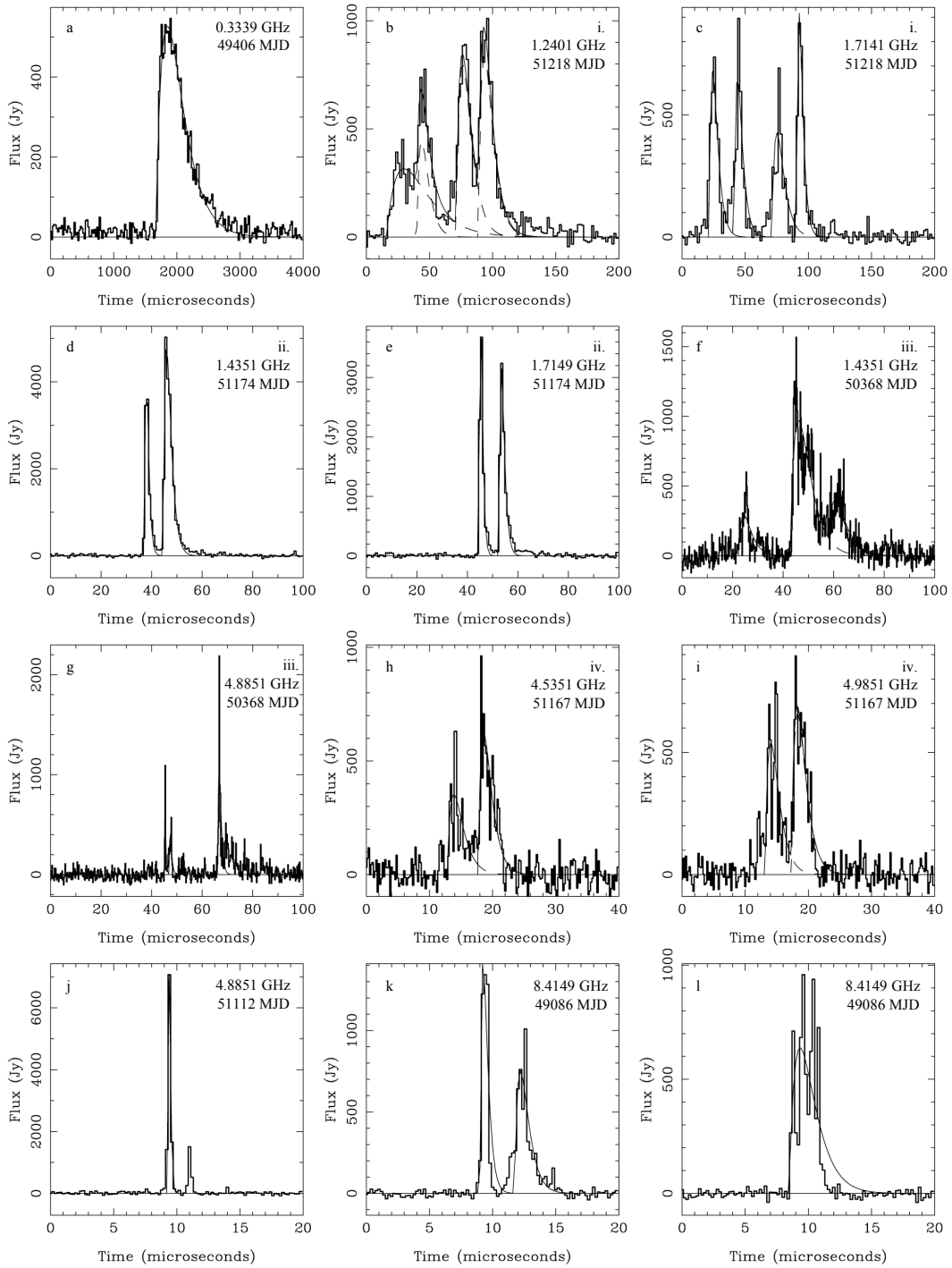


Figure 2.2: Examples of fitted microbursts. See § 2.3 for details.

time resolution is given in Table 2.1. Pulses are labeled by unique letters in the top left of each plot. The observing frequency and MJD are shown, for comparison with Table 2.1. Pulses recorded simultaneously at two different frequencies are denoted by a corresponding lowercase Roman numeral in the top right corner of each plot.

2.4 Results

2.4.1 Goodness of Microburst Fits

Examples of fitted microbursts are shown in Figure 2.2. I find that the fast-rise-slow-decay function given in equation (2.1) fits my microbursts best at low frequencies. This is no surprise since the function in equation (2.1) is a modification of the empirical best fit found by Rankin et al. (1970), who were fitting Crab average profiles observed at frequencies of 74 to 430 MHz. The consistency of single giant pulse shape at 0.3 GHz, compared with the variability seen at higher frequencies, indicates that the lower frequency pulse shape is dominated by interstellar scatter broadening. In §1.3.2, I explain that a thin screen scattering model predicts interstellar scatter broadening will relate to frequency as

$$\tau_B \propto \nu^{-4}. \quad (2.3)$$

I observe single pulses at 0.3 GHz with pulse widths of approximately 600 μs . Extrapolating from this measurement, Table 2.2 shows the expected amount of interstellar scatter broadening for the full range of frequencies I have observed. Above 0.3 GHz, the microburst widths I measure (see §2.4.2) are all larger than the inferred interstellar scattering width. It should be noted that changes in pulse width do occur over a range of time scales [for example see Backer et al.

Table 2.2: Interstellar Scatter Broadening Widths

Frequency (GHz)	Scattering Width (μs)
0.3	600
1.2	2
1.4	1
4.5	0.01
8.4	0.0009

(2000)]. Widths calculated in Table 2.2 are representative only of the epoch of the 0.3 GHz observation (see Table 2.1).

At 0.33 GHz the main pulse⁶ is very well fitted with a single term of Equation (2.1) ($n = 1$). Between 1.2 and 1.7 GHz, microbursts are well fitted with occasional deviations from the functional form at the beginning or end of the microburst; for example, see plot (b) in Figure 4.1. Above 4.5 GHz, microbursts are frequently composed of very narrow bursts of emission which are superimposed upon broader features often resembling the functional form of equation (2.1); see, for example, plots (g), (h), and (i) in Figure 2.2.

The function described by Equation (2.1) fits resolved emission features well, but it does not fit unresolved⁷ structures well. Although unresolved emission is sometimes present in 1- to 2-GHz data (often at the peak of a resolved microburst), unresolved emission is more abundant at higher frequen-

⁶At 0.33 GHz interstellar scatter broadening obscures microstructure, and results in a main pulse that consists of only one broad microburst.

⁷In this context, “unresolved” refers only to the smoothed and decimated data; in the absence of smoothing, the same features may be resolved, but the higher noise level makes analysis more difficult.

cies. Examples of such unresolved emission are seen in plots (c) and (e) through (l) of Figure 2.2. Unresolved bursts at the peak of broader microbursts can account for a large fraction of the microburst peak flux. In my data, most of these unresolved bursts are not fitted and therefore are not accounted for in the analysis of this section. Fortunately, the energy contribution of the unresolved emission is very small compared to most microbursts; therefore, my microburst energy measurements are not greatly affected by this limitation of my fitting function and algorithm.

2.4.2 Microburst Analysis

Microburst characteristics, derived from function fits, are shown graphically in Figures 2.3 through 2.13. All figures contain plots in three columns; from left to right the plots are, microburst flux versus width, microburst energy histogram, and microburst width histogram. The flux versus width plots contain data points plotted as diamonds, with error bars denoting the fitted-microburst uncertainty in both flux and width. Data points plotted as triangles do not have error bars because the uncertainties are large enough to push the bounds of the error bars beyond zero, on one or both axes (these error bars cannot be displayed on a logarithmic plot). Diagonal lines in the flux-width plots denote constant energy curves and are described below. To ease comparison, the horizontal and vertical axis ranges are uniform for all flux versus width plots in Figures 2.3 through 2.13. The histograms show the distribution of microburst energy and width. In both histograms, data are binned in one-tenth-decade intervals; the histogram values are not normalized to the bin

size⁸. The horizontal axis of each histogram is uniform throughout Figures 2.3 to 2.13. The diagonal lines in the energy histogram plots show uniform microburst energy distributions and are discussed later in this section.

Figures 2.3 through 2.11 display microburst characteristics for individual observing sessions; each row contains one observing session. Rows are ordered by frequency, the same order as Table 2.1.

Figures 2.12 and 2.13 show the same data as contained in Figures 2.3 through 2.11, but here data have been grouped by frequency. Each row displays the characteristics of all data observed within the specified frequency range; rows are ordered by frequency. By combining observing sessions with similar frequencies, I increase the statistical significance of several microburst trends.

Microburst Flux Analysis

The left-most columns of Figures 2.3 through 2.13 contain plots of microburst width (W) versus microburst maximum flux (F_{\max}). Flux variability over 2 or more orders of magnitude is present in every frequency group and almost every observing session (excluding the 0.34-GHz pulses). This large microburst flux variability occurs on timescales as short as microseconds; even within a single main pulse. However, for each observing session (Figures 2.3 to 2.11), the apparent centroid of the microburst flux is relatively constant;

⁸The units of the vertical axis are “number of microbursts”, not “number of microbursts per bin size”. This is important when comparing to an analytical model, as done later in this section.

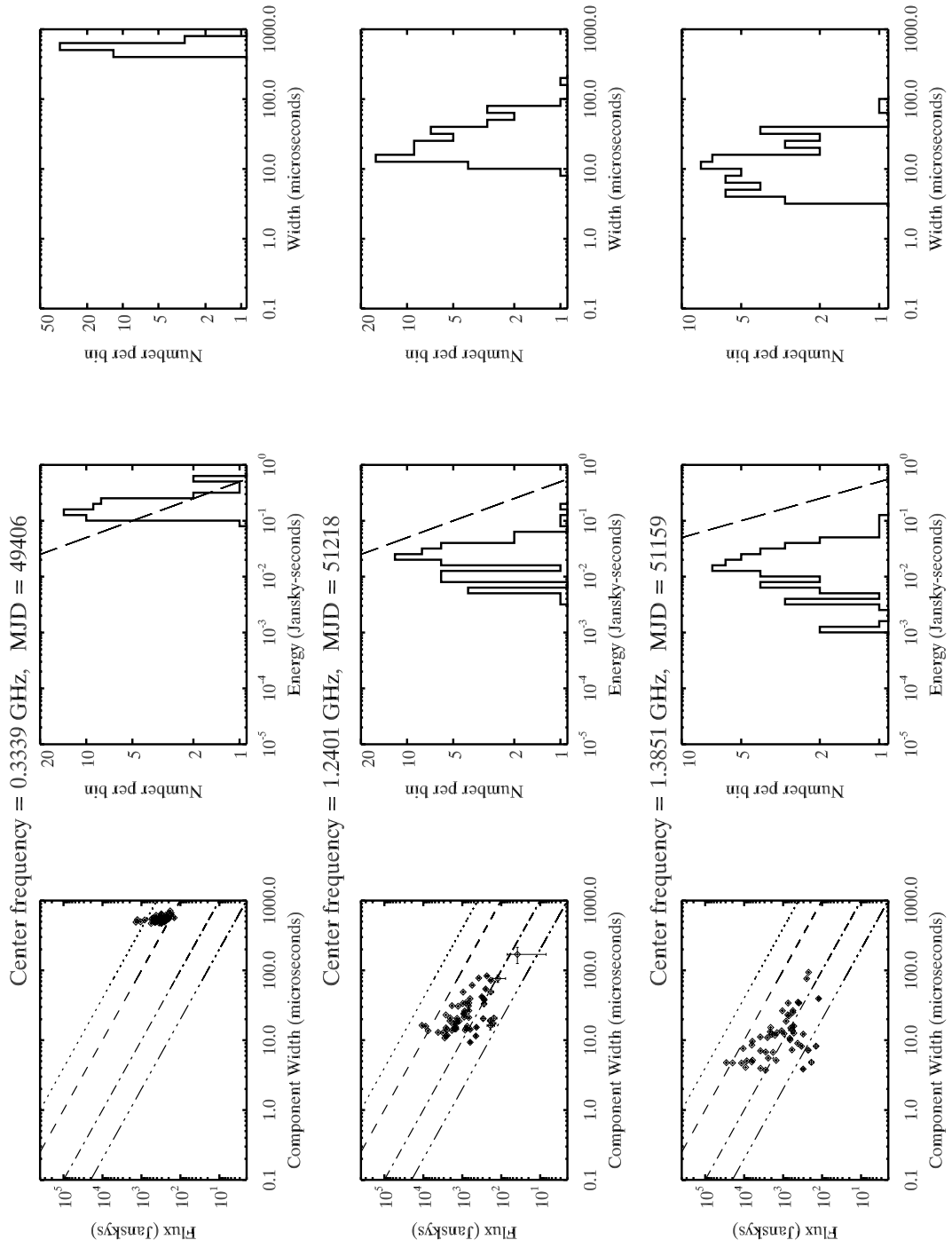


Figure 2.3: Microburst characteristics for individual observing sessions. See § 2.4.2 for details.

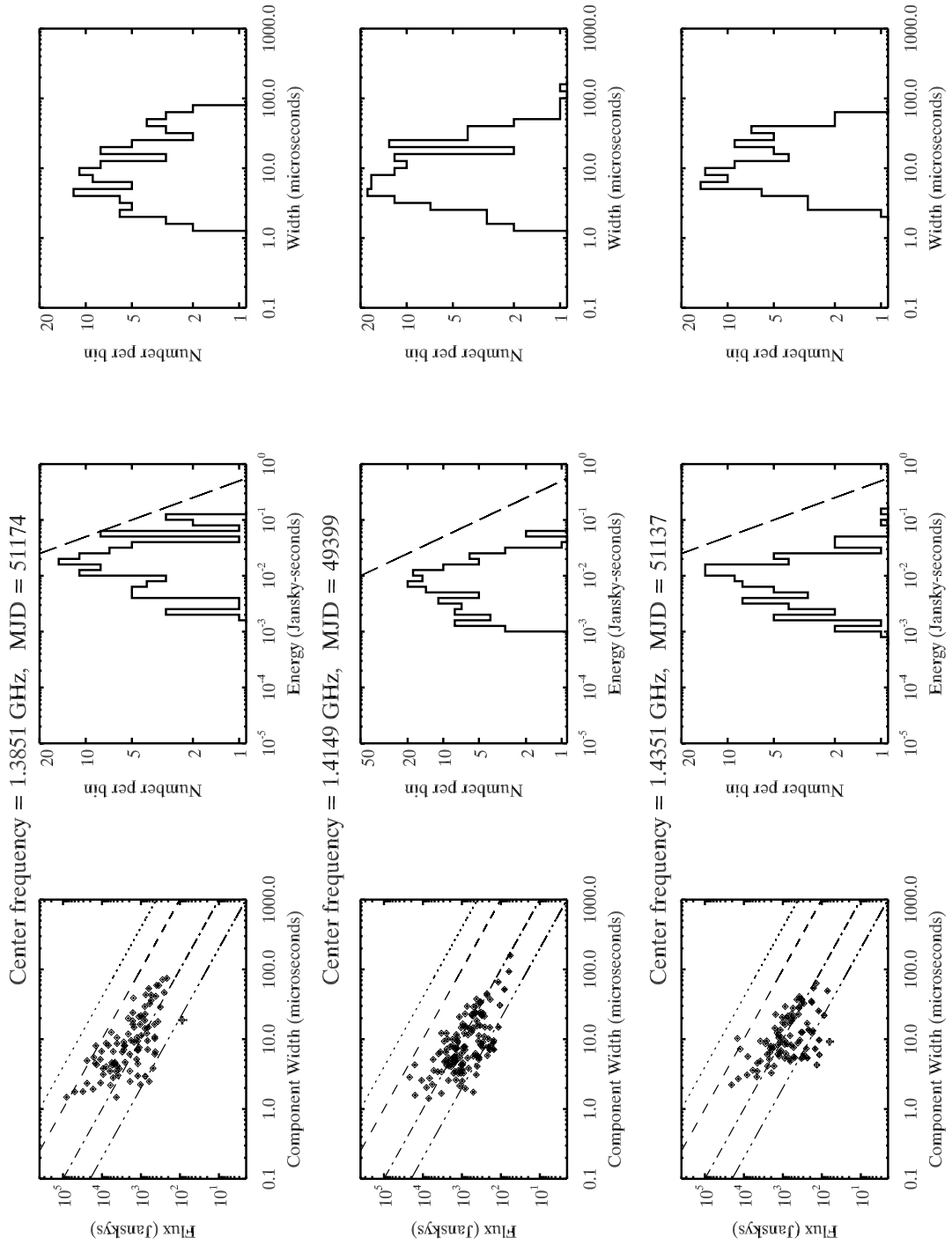


Figure 2.4: Microburst characteristics for individual observing sessions (continued from Figure 2.3).

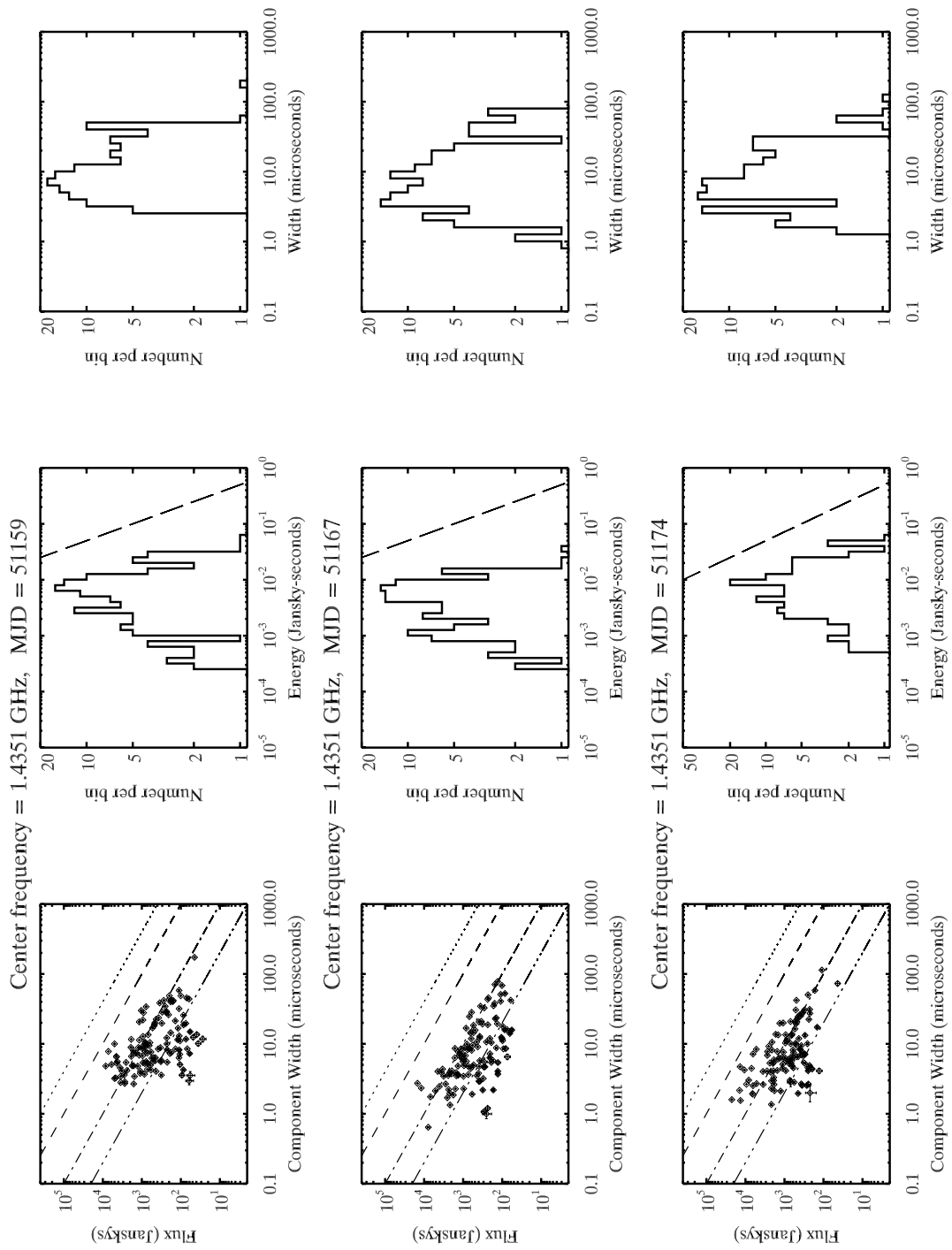


Figure 2.5: Microburst characteristics for individual observing sessions (continued from Figure 2.4).

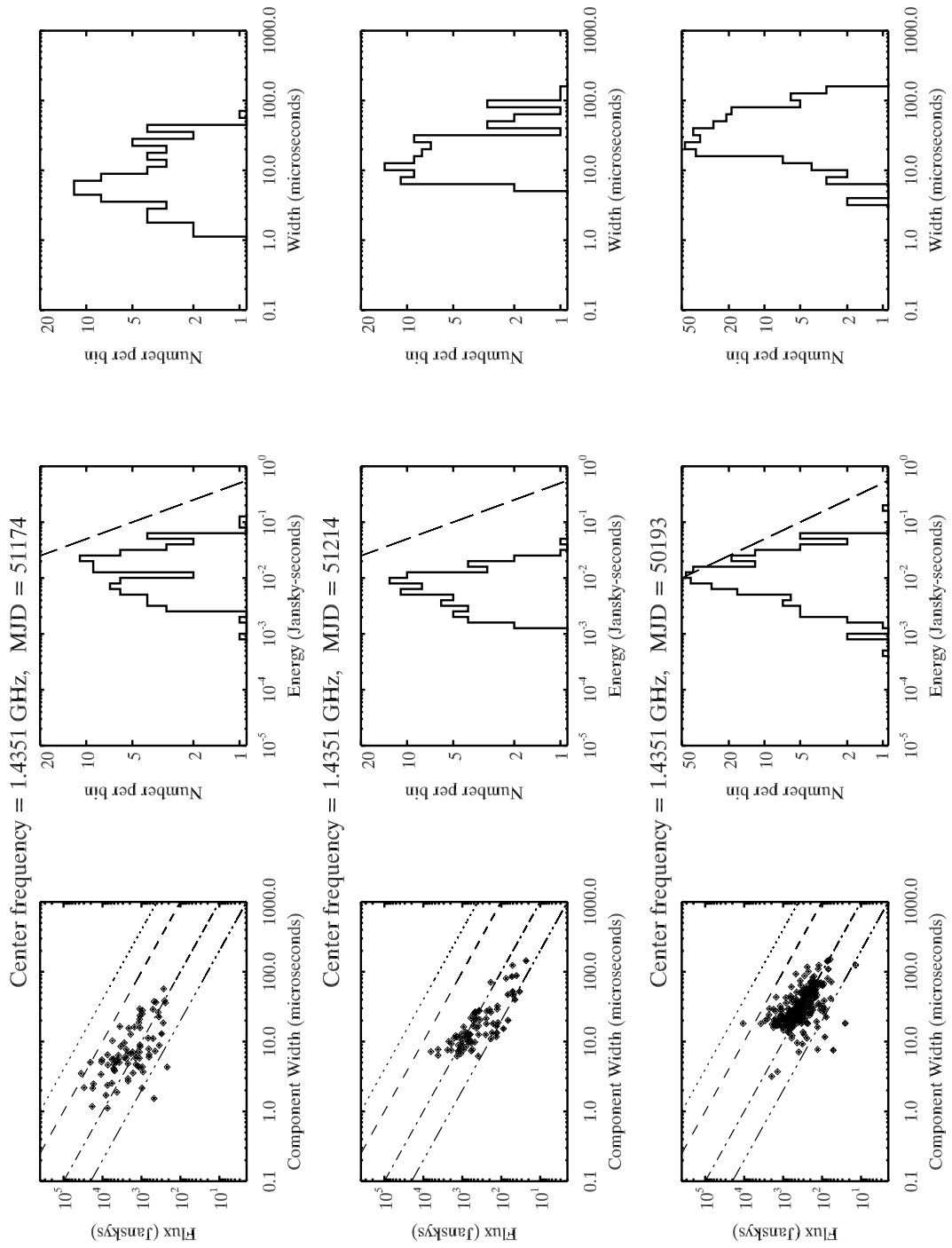


Figure 2.6: Microburst characteristics for individual observing sessions (continued from Figure 2.5).

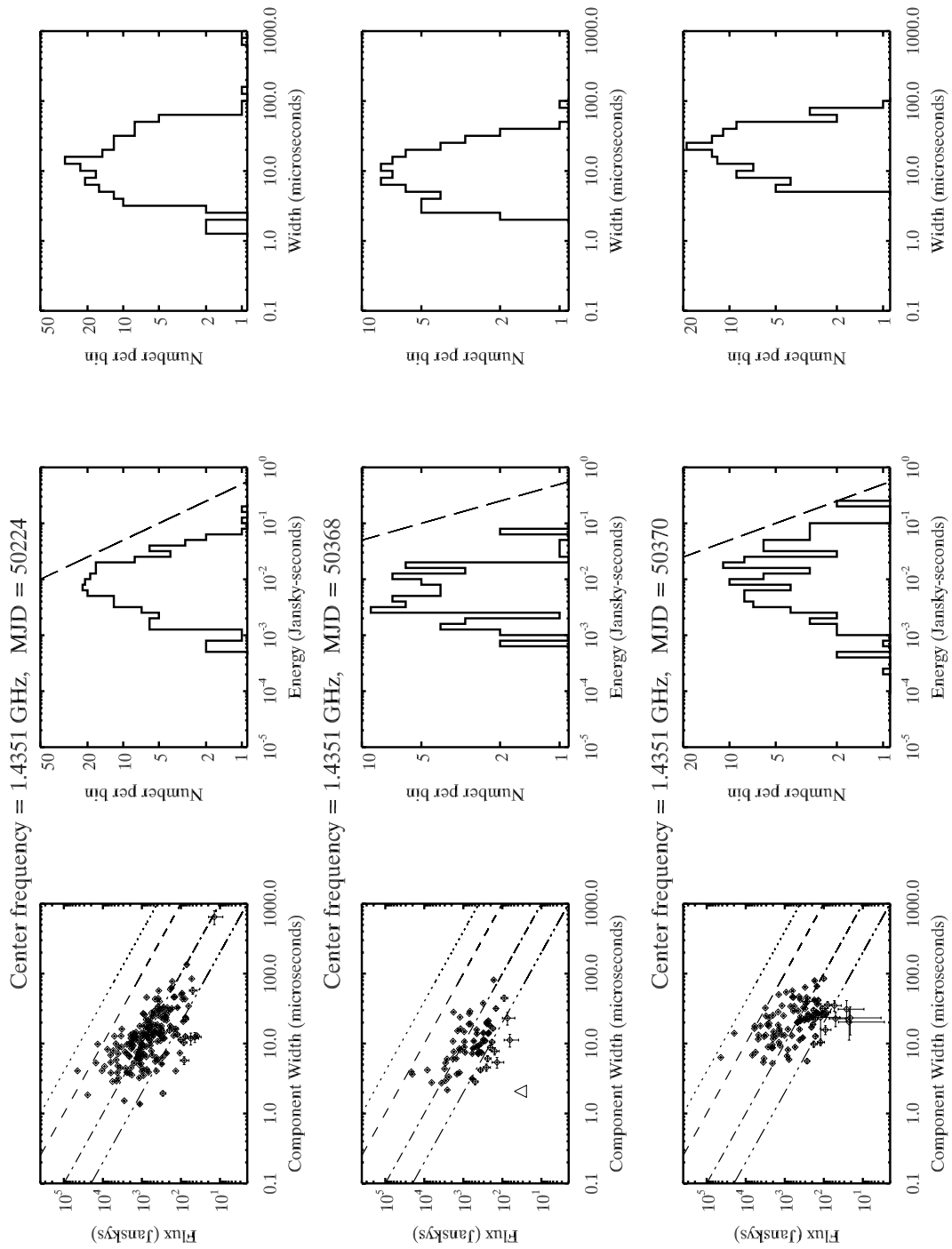


Figure 2.7: Microburst characteristics for individual observing sessions (continued from Figure 2.6).

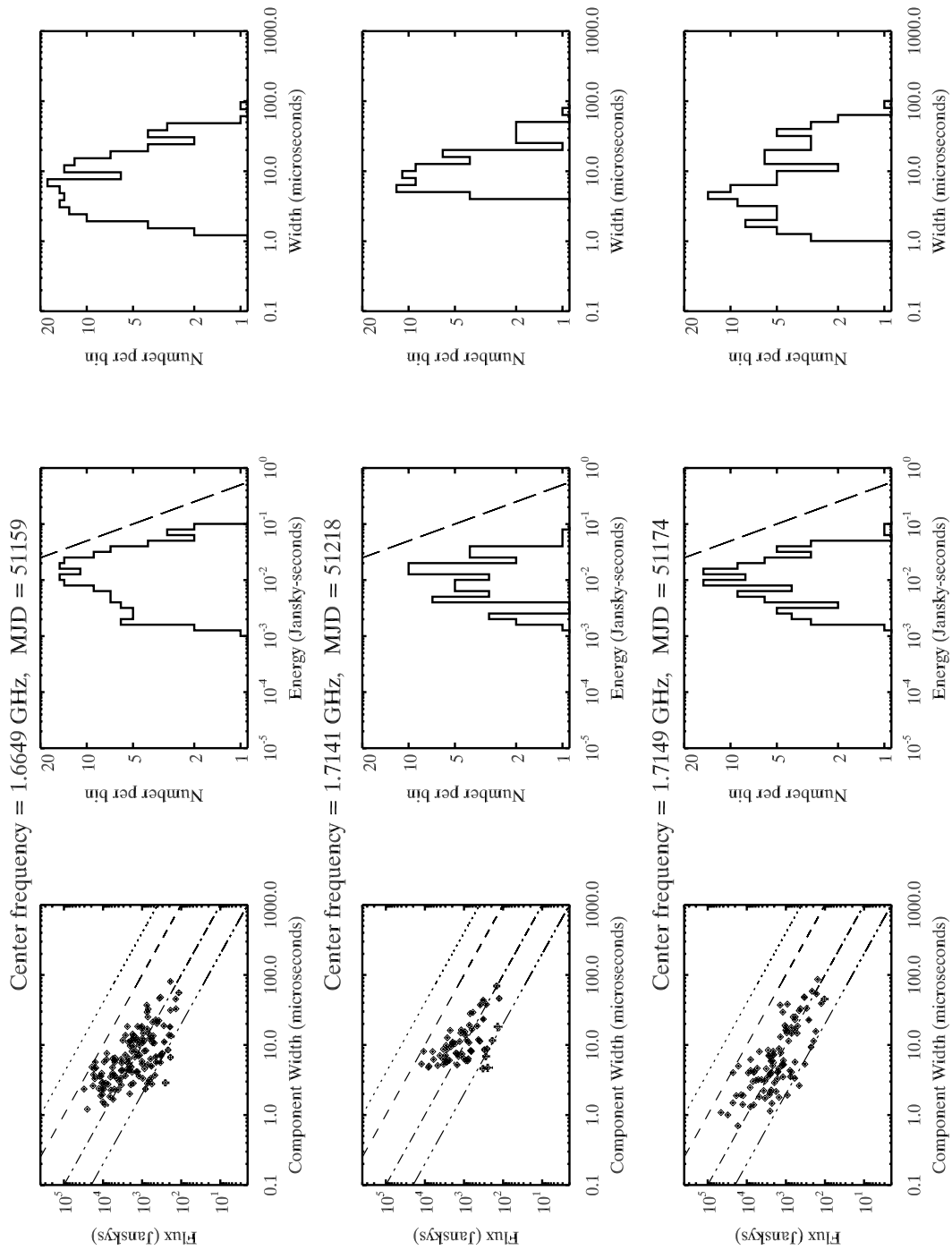


Figure 2.8: Microburst characteristics for individual observing sessions (continued from Figure 2.7).

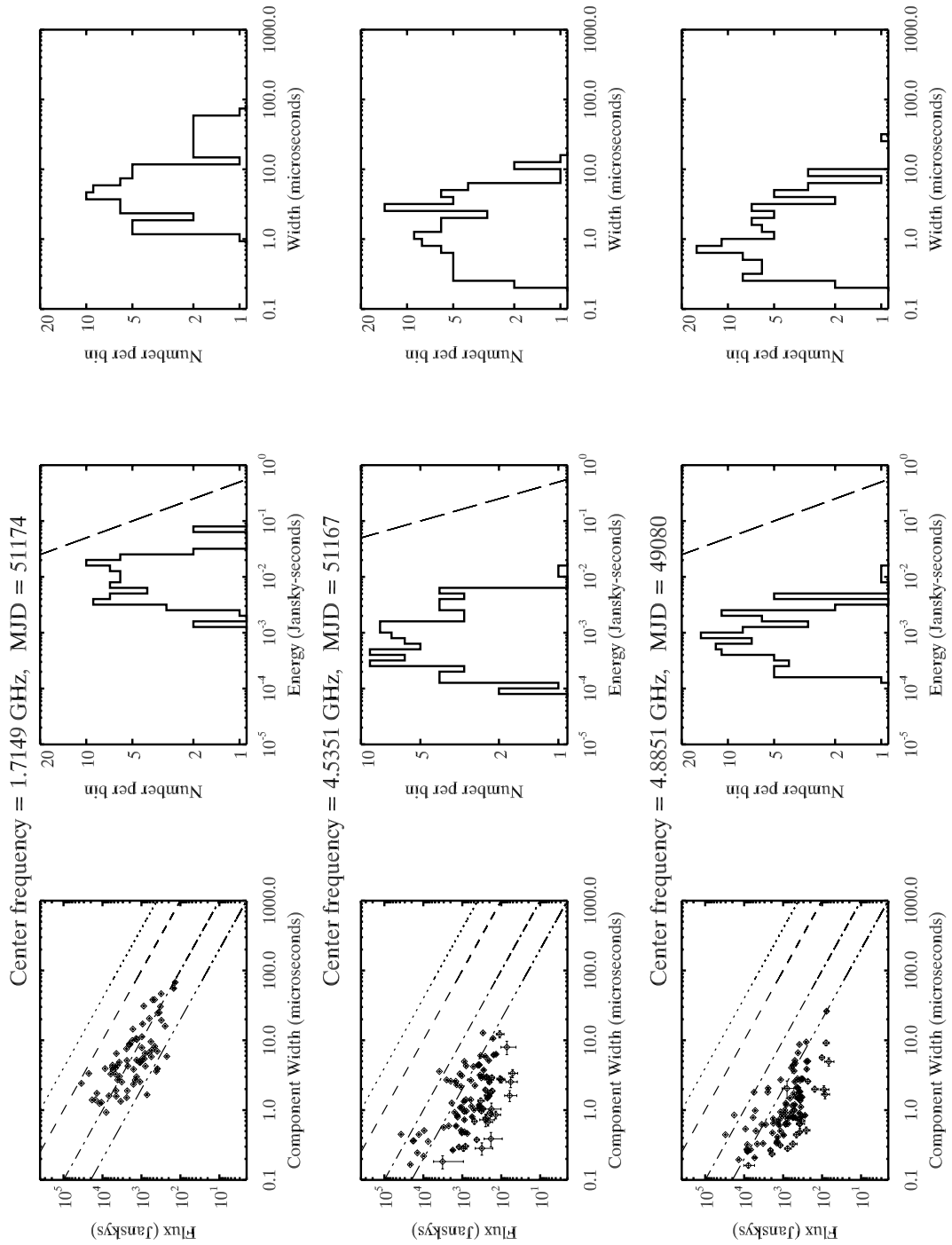


Figure 2.9: Microburst characteristics for individual observing sessions (continued from Figure 2.8).

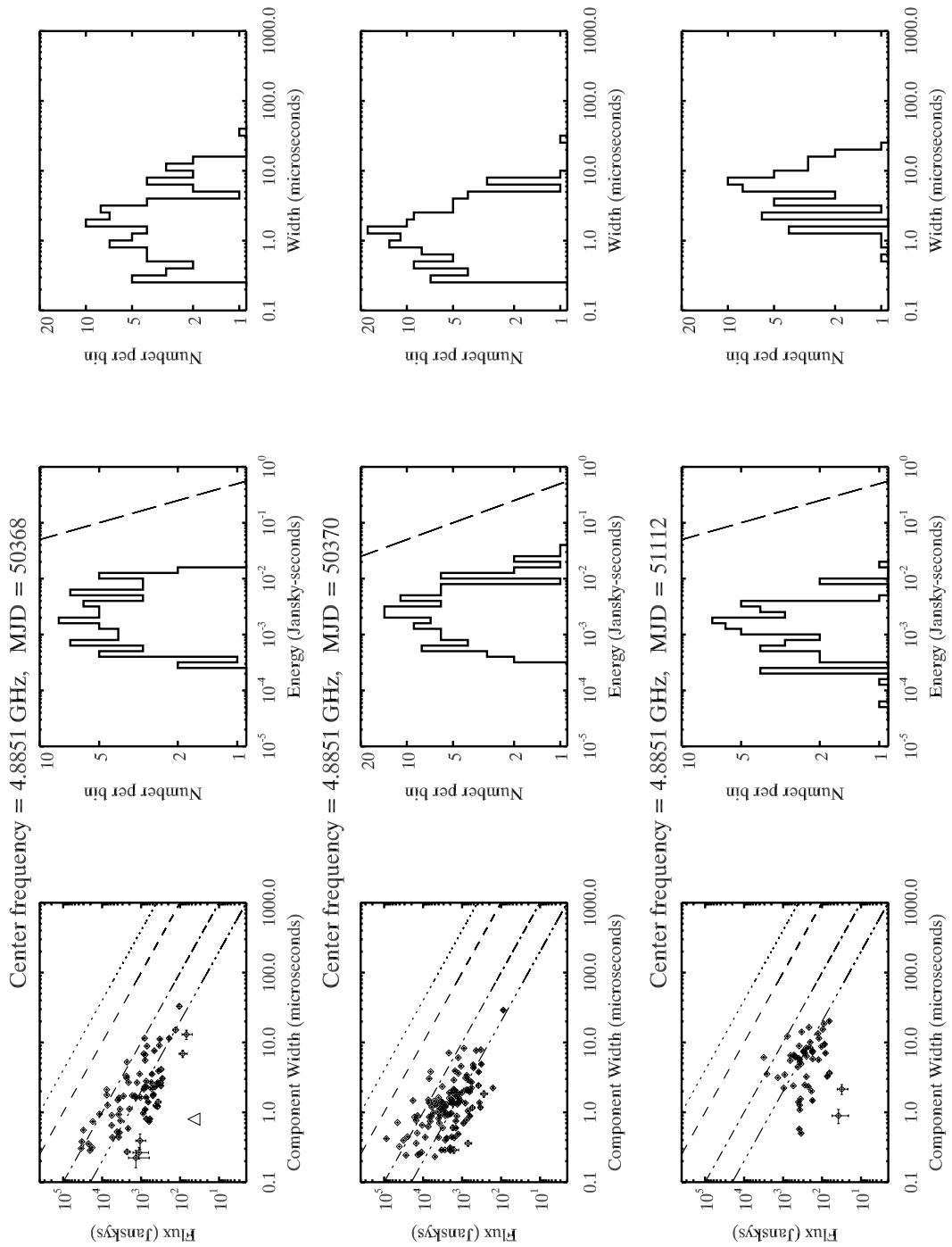


Figure 2.10: Microburst characteristics for individual observing sessions (continued from Figure 2.9).

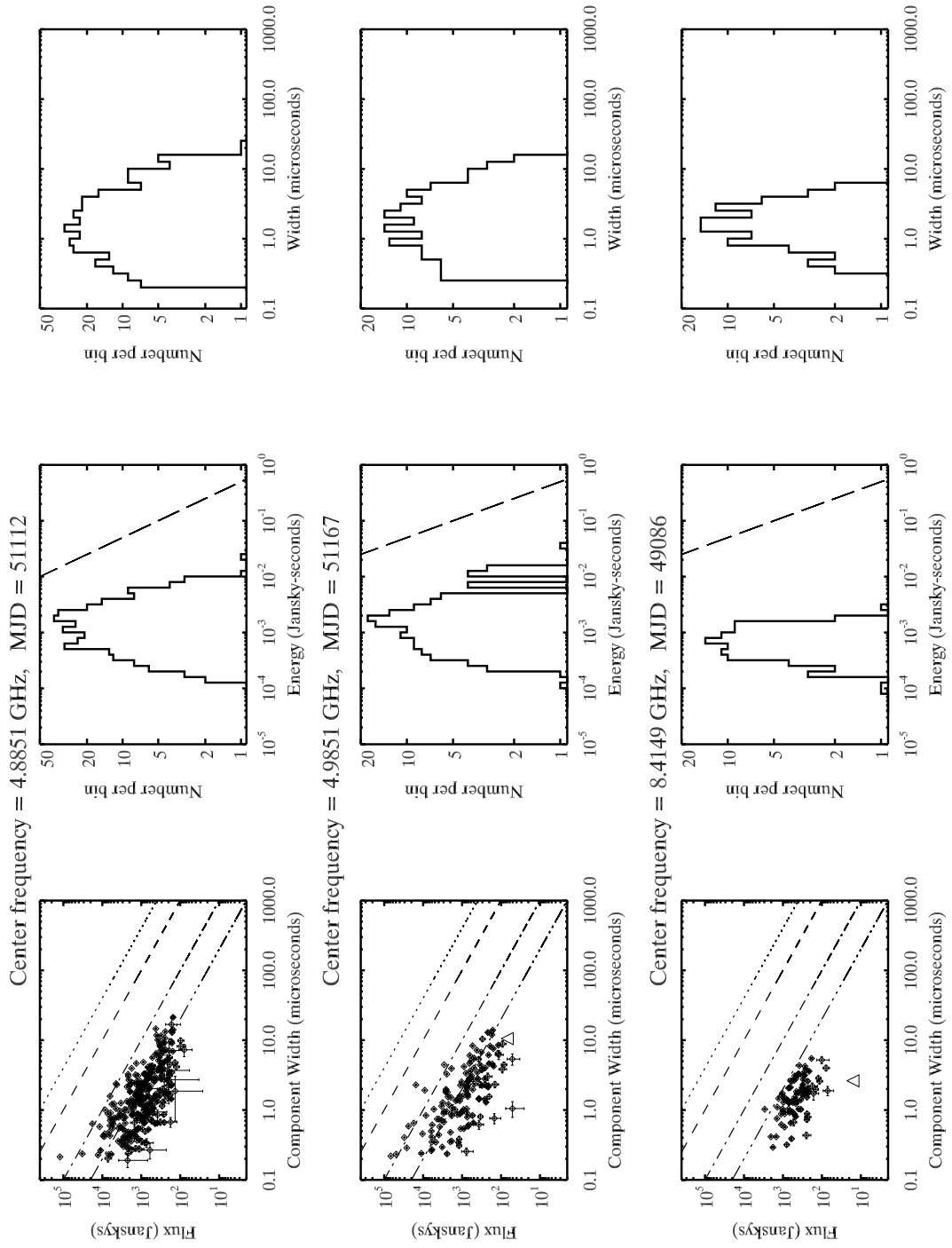


Figure 2.11: Microburst characteristics for individual observing sessions (continued from Figure 2.10).

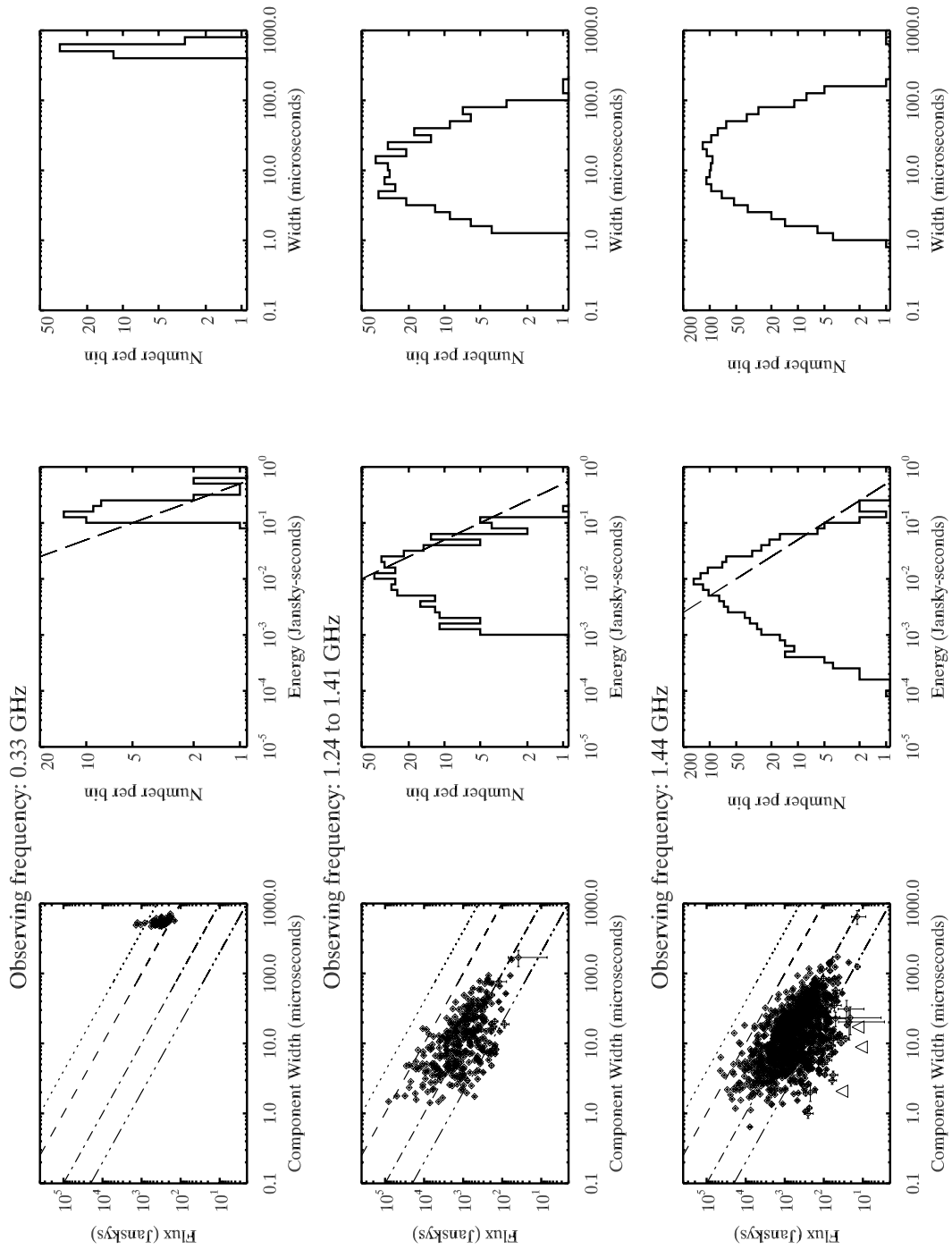


Figure 2.12: Microburst characteristics, grouped by frequency. See § 2.4.2 for details.

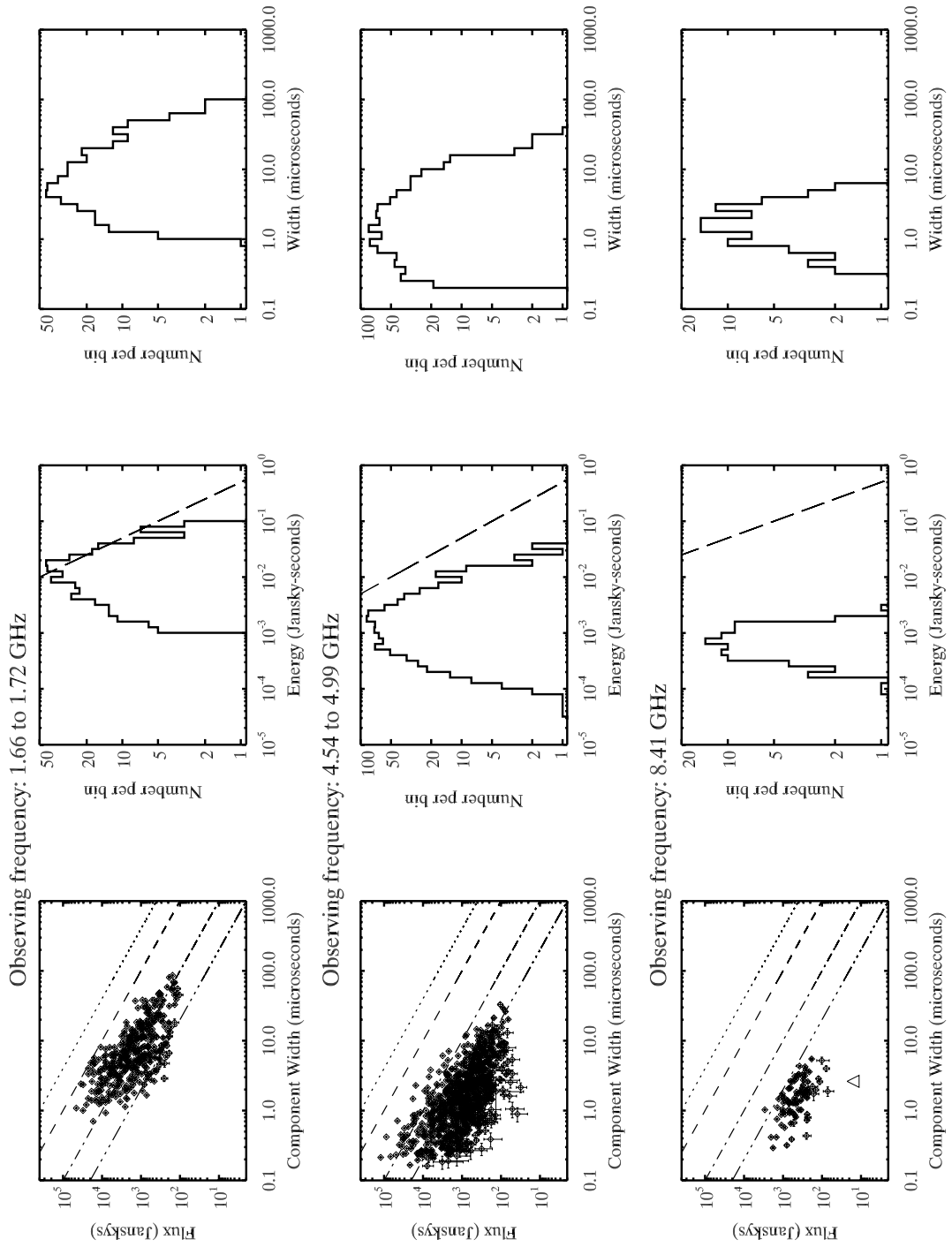


Figure 2.13: Microburst characteristics, grouped by frequency (continued from Figure 2.12).

the microburst flux centroid varies by a factor of a few between observing sessions (timescales of hours to days). This result agrees with Lundgren et al. (1995) and Rickett & Lyne (1990), both of whom observe total flux amplitude variations (at 0.8 and 0.61 GHz, respectively⁹) in time-averaged Crab pulses of factor of a few on timescales of 5 to 100s of days. This relatively small time-averaged flux variability, in contrast to the 2-order-of-magnitude microburst variability, is precisely what allows us to study pulse flux in frequency groups (such as those in Figures 2.12 and 2.13), where data recorded on different days has been combined.

The measurements reveal significant variability in microburst energy (see below in this section for further discussion of microburst energies). The energy threshold used to record only giant pulses (see § 1.5) biases the microbursts toward higher energy. Since energy is a product of microburst width and flux (see § 2.3, and below), the microburst sample is biased toward both large-width and high-flux microbursts. In the frequency-grouped data, the high-flux and large-width part of the main pulse microburst distribution is well sampled¹⁰. At all frequencies, there exists a break in the flux-width distribution that occurs along a power law (linear function in the log-log plots) with negative slope; on the high-flux, high-width side of the break, the number of microbursts decays rapidly. As frequency increases, the break moves toward smaller widths.

⁹Flux amplitude variability above 2 GHz is not well studied. In this part of the spectrum, scintillation timescale increases with frequency, requiring a comparable increase in the observing time for studying scintillation-induced variability.

¹⁰This assumes that the recorded dispersed pulses did not saturate the VLA voltage samplers.

Table 2.3: Constant Energy Curves in Figures 2.3 through 2.13

Line Style	E (Jy· μ s)
dot	$4 \cdot 10^5$
dash	$1 \cdot 10^5$
dash-dash-dot	$1 \cdot 10^4$
triple dot-dash	$2 \cdot 10^3$

Using the microburst fitting function in §2.3 I see that microburst energy relates to flux and width as

$$E_i = \frac{e}{3}(F_{\max})_i W_i. \quad (2.4)$$

If the flux-width distribution break visible in Figures 2.3 through 2.13 occurs at a frequency-dependent energy, then the break may be described by a power law $F_{\max} \propto W_i^{-1}$. Equation (2.4) has been drawn in the flux-width plots of Figures 2.3 through 2.13 for four values of E listed in Table 2.3. These energy values roughly correspond to the flux-width breaks visible at each frequency. The energy values in Table 2.3 also correspond to the upper limit of the energy distributions, plotted in the middle column of Figures 2.3 through 2.13. These energy plots are discussed in detail later in this section.

Comparing the flux-width data with the constant energy curves reveals that the distribution break may have a steeper slope than is described by the constant energy expression, above. In particular, the data points at the large-width side of the distribution appear to drop away from the constant energy lines as width increases. A quantitative fit to the break is left for a future study.

Microburst Width Analysis

At each of the six observing frequencies the microburst width distributions shown in Figures 2.12 and 2.13 are roughly symmetric (in log space) about some mean width. At 0.3 GHz the microbursts are very wide with only minimal variation about a width of $600 \mu s$. Between 1.2 and 1.44 GHz, widths vary over 2 orders of magnitude and are centered on $10 \mu s$. The 1.6 to 1.7 GHz distribution has a peak density near $5 \mu s$, and is approximately scattered over 2 orders of magnitude; here, the asymmetry in the logarithmic width density distribution is likely a result of data smoothing and decimation to $0.8 \mu s$ ¹¹. At 4.5 to 4.9 GHz the maximum of the microburst width density distribution is $1 \mu s$; whereas the smoothed and decimated time resolution is $0.2 \mu s$. At 8.4 GHz the width distribution density peaks at approximately $2 \mu s$ and is scattered over slightly more than 1 order of magnitude.

The large variability in microburst width occurs on very short timescales. Microbursts within a single pulse (~ 1 ms timescales) can have vastly different widths. Neither the interstellar medium nor the Crab Nebula vary rapidly enough to account for such short timescale pulse width variability. The variability must be a result of processes occurring in the emission region—within the pulsar magnetosphere.

Kern (2004) used some of the same data presented here to study pulse scatter broadening. Using a function identical to equation (2.1) [differing only

¹¹Microburst fitting becomes difficult as the microburst width approaches the post-processing time resolution limit. Unresolved and nearly-unresolved microbursts are narrow rectangle functions—not fast-rise-slow-decay functions, such as equation (2.1). Only the strongest unresolved microbursts have been fitted. See §2.4.1 for further discussion.

in constants; Kern’s equation (3.2)], he fits giant pulse microbursts in a manner very similar to what I have done here. After fitting, he estimates the lower bound of the microburst width distribution and infers that this lower bound is equivalent to τ_B , the scatter broadening width of the interstellar medium. His measurements of τ_B are within an order of magnitude less than the lowest widths measured in the same frequency groups shown in Figures 2.12 and 2.13; Kern’s τ_B is greater than or equal to the interstellar scattering width estimates shown in Table 2.2, which were inferred from the width distribution at 0.3 GHz. Kern (2004) finds that his measurements of τ_B are roughly consistent with $\tau_B \propto \nu^{-4}$, as described in § 1.3.2 and equation (2.3).

In addition to measuring the pulse microburst widths using functions fitted to the time series data, Kern (2004) fits an interstellar scattering transfer function to observing-session-averaged power fluctuation spectra, using some of the same data presented in this chapter. He then measures the half power point of the transfer function and uses this to describe a “characteristic” width of the giant pulses. I have inverted the half power point measurement to obtain the characteristic width¹². These are listed in Table 2.4.

From 1.3 to 5.0 GHz, Kern’s characteristic widths are slightly larger than the widths at the peak density of the width histograms in the frequency-composite plots of Figures 2.12 and 2.13; at 8.4 GHz the characteristic width falls at the upper bound of the width distribution. At 0.3 GHz, Kern’s characteristic width lies at the small-width end of the width distribution in Figure

¹²The characteristic width, τ , relates to the spectral half power point, $\nu_{-3\text{dB}}$, as $\tau \nu_{-3\text{dB}} = 1/2\pi$.

Table 2.4: Characteristic Giant Pulse Widths from Kern (2004)

Frequency (GHz)	Half Power Point (Hz)	Characteristic Width (μ s)
0.3330	3.84×10^2	414.5
1.3851	9.33×10^3	17.1
1.3851	1.37×10^4	11.6
1.4351	1.22×10^4	13.0
1.6649	1.51×10^4	10.5
1.7149	9.62×10^3	16.5
3.3750	5.60×10^4	2.8
4.1500	7.08×10^4	2.2
4.1500	5.65×10^4	2.8
4.8851	3.72×10^4	4.3
5.5000	4.11×10^4	3.9
8.4149	2.25×10^4	7.1

Compare with Table 3.2 in Kern (2004).

2.3; the reason for the different positioning of the characteristic width relative to my width distribution at this low frequency is not clear. However, I do note that this 0.3 GHz data is the only data set that is completely interstellar scattering dominated (see goodness of fit discussion in § 2.4.1). Kern's characteristic widths, in conjunction with some scattering measurements from the literature, are described by a pulse broadening power law $\tau \propto \nu^{-1.9}$. The significance of this power law is discussed further in § 2.4.3 below.

Microburst Energy Analysis

The microburst energy histograms in Figures 2.3 and 2.13 show several interesting things. Foremost, is the fact that microbursts inhabit a range of energies. This differs from the suggestion by some authors that giant pulse

microbursts have a constant energy (Benford, 2003). The energy distribution can also be seen in the flux-width plots in the left most column of Figures 2.3 through 2.13; the constant-energy lines (see also Table 2.3) clearly show the variability in energy.

However, it is still possible that microbursts have constant energy in the emitter’s rest frame, and that the emission is relativistically beamed in the direction of the emitter’s motion (Weatherall & Eilek, private communication). To model this, let E' be the microburst energy in the emitter’s rest frame. Let the emitter have dimensionless velocity β , Lorentz factor γ , and move along a path at an angle θ to the Earth-pulsar line of sight. Then, letting $\mu = \cos(\theta)$, a Lorentz transformation gives the microburst energy in the Earth frame,

$$E = \frac{E'}{\gamma(1 - \beta\mu)}. \quad (2.5)$$

Let us assume that microbursts are emitted equally at all angles to the Earth-pulsar sight line; the distribution $n(\mu)$ is uniform. Then, the microburst distribution in angle relates to the distribution in energy as,

$$n(E)dE = n(\mu)d\mu \implies n(E) = \frac{n(\mu)}{dE/d\mu} \quad (2.6)$$

Combining equations (2.5) and (2.6), the energy distribution varies as

$$n(E) \propto \frac{1}{E^2}. \quad (2.7)$$

To compare equation (2.7) with the energy distributions, I multiply by E to obtain units of “number of microbursts”¹³. One example of this model

¹³Recall from earlier in this section that the vertical axes of these histograms have units of “number of microbursts”.

using constant of proportionality $0.5 \text{ Jy} \cdot \text{s}$ is plotted on the energy histograms in Figures 2.3 through 2.13. Comparing the data with the model I find that the high-energy side of the microburst energy distribution is only partially described by the model. At the highest energies the distribution falls more rapidly than the model. The microburst energies where the energy histograms fall away from the constant emission-frame-energy model roughly corresponds with the high-energy side of the flux-width distribution, which can be identified using the constant (observing frame) energy lines overlaid on the flux-width plots. The break in the flux width distributions (discussed above in this section) occurs at slightly lower energies.

The minimum pulse energies required for recording giant pulses (set at observing time; see § 1.5) correspond roughly with the peaks of the energy distributions in Figures 2.3 through 2.13. For a pulse with multiple microbursts, each burst contributes to the total pulse energy. For this reason, the microburst distribution is not truncated at the observational threshold, but it is under sampled. To avoid this under-sampled region, I do not analyze the low-energy side of the energy histograms.

The upper-bound of the energy distribution decreases with increasing frequency. This agrees with negative spectral index measurements of giant pulses, -2.7 ± 0.1 (Popov et al., 2006), and average profiles, -3.1 ± 0.2 (Lorimer et al., 1995). In § 2.4.3 I measure spectral indices for giant pulses observed simultaneously at two different frequencies and compare them with these measurements made by other authors.

2.4.3 Simultaneous Two-frequency Observations

After fitting the function of Equation (2.1) to microbursts in all the data, I look for evidence of microburst width and energy frequency dependence by carefully inspecting data sets that were observed simultaneously at two different frequencies. These data are denoted by superscripts in the first column of Table 2.1; simultaneously recorded data sets have the same superscript.

The same microbursts at high and low frequencies can be identified by visual inspection in some, but not all, of these data. Examples of simultaneously observed microbursts are shown in Figure 2.2 (i.e., pairs b & c, d & e, f & g, h & i). Corresponding microbursts are identified in three observing sessions that simultaneously recorded pulses at two bands between 1 and 2 GHz; and in one observing session that recorded pulses at two bands between 4 and 5 GHz. These four observing sessions (8 data sets total) are marked in Table 2.1 with superscripts *a*, *c*, *d*, and *g*¹⁴. Corresponding microbursts could not be identified in the majority of pulses observed simultaneously at 1.4 and 5 GHz. This suggests that the microbursts have an emission bandwidth of < 4 GHz in this frequency range, or that propagation in the pulsar magnetosphere sufficiently distorts one or both passbands that identification of burst pairs at the two frequencies is impossible.

In the four data set pairs listed above and in Table 2.5, 192 high- and low-frequency fitted microburst pairs are matched. Figures 2.14 and 2.15 show the correlation of microburst width and microburst energy, respectively,

¹⁴These superscripts are also referenced from Table 2.5

of these high- and low-frequency microbursts; both the microburst energies and widths are well correlated and have roughly a linear relationship between high and low frequency. In each plot, a dotted line shows the location of horizontal and vertical axis equality.

Width Measurements

Figure 2.14 reveals that lower frequency microbursts are typically wider than their higher frequency counterparts. To compare these findings with the results of other authors I quantify the width-frequency relationship using a power law, $W \propto \nu^y$; where ν is the observing frequency and y is a power law index to be determined. I measure power law indices for each microburst pair; the means, $\langle y \rangle$, and standard deviations, σ_y , of these indices are shown in Table 2.5. There is a large scatter in power law indices for each of the 4 observing session pairs. It should be noted that this scatter is not a result of measurement uncertainties. The large standard deviations of power law indices are partially a result of relative microburst-pair width fluctuations—fluctuations that are intrinsic to the observed pulse. These fluctuations are quantitatively amplified by the small separation (or “baseline”) of the two frequency bands, and I note that the smallest standard deviation of $\langle y \rangle$ occurs in the data set pair having

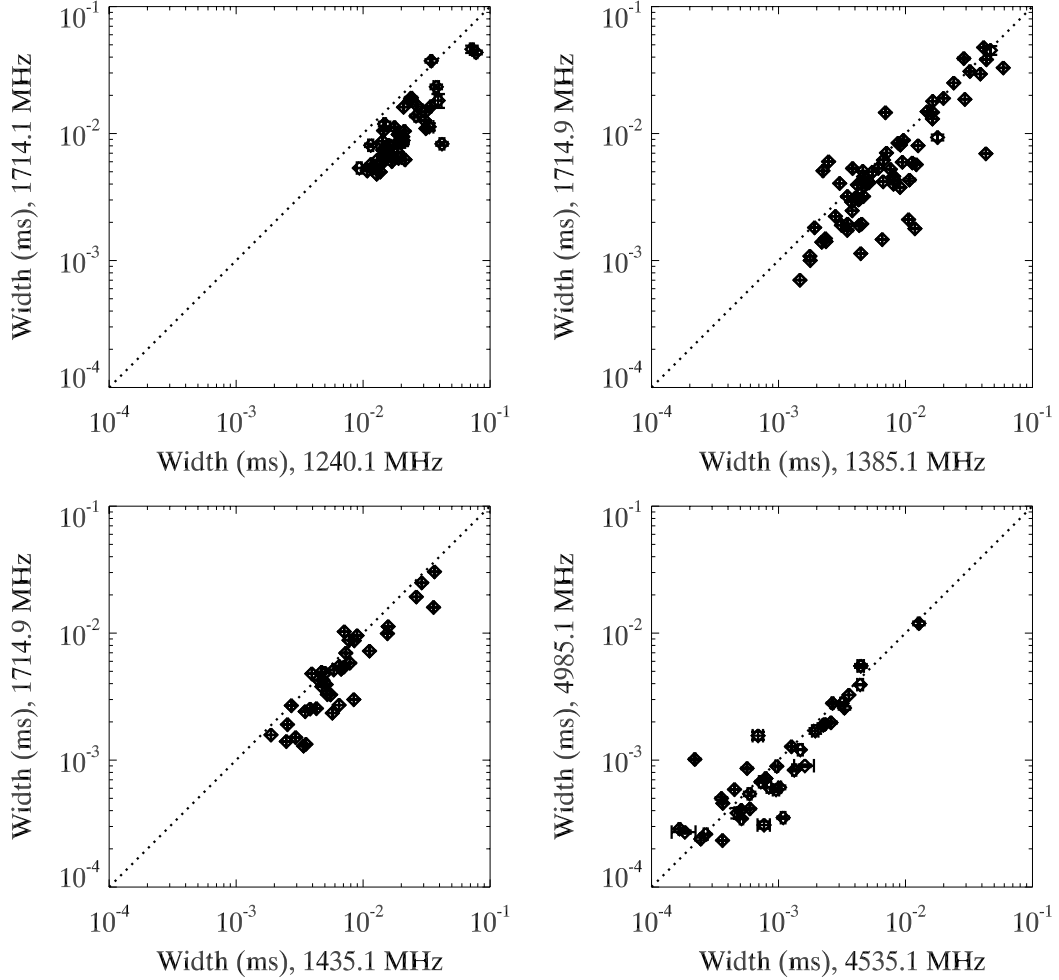


Figure 2.14: High- versus low-frequency microburst widths of simultaneous two-frequency observations. Error bars determined during the microburst fitting process are plotted for both axes. On average, lower-frequency microbursts tend to be wider than high-frequency microbursts. Average power law indices have been measured for each data set and are shown in Table 2.5. The scatter in data points (or standard deviation of the width power law index mean; see Table 2.5) tends to increase roughly with decreasing relative separation of observing bands, as explained in § 2.4.3. The dotted line shows the location of high- and low-frequency width equality.

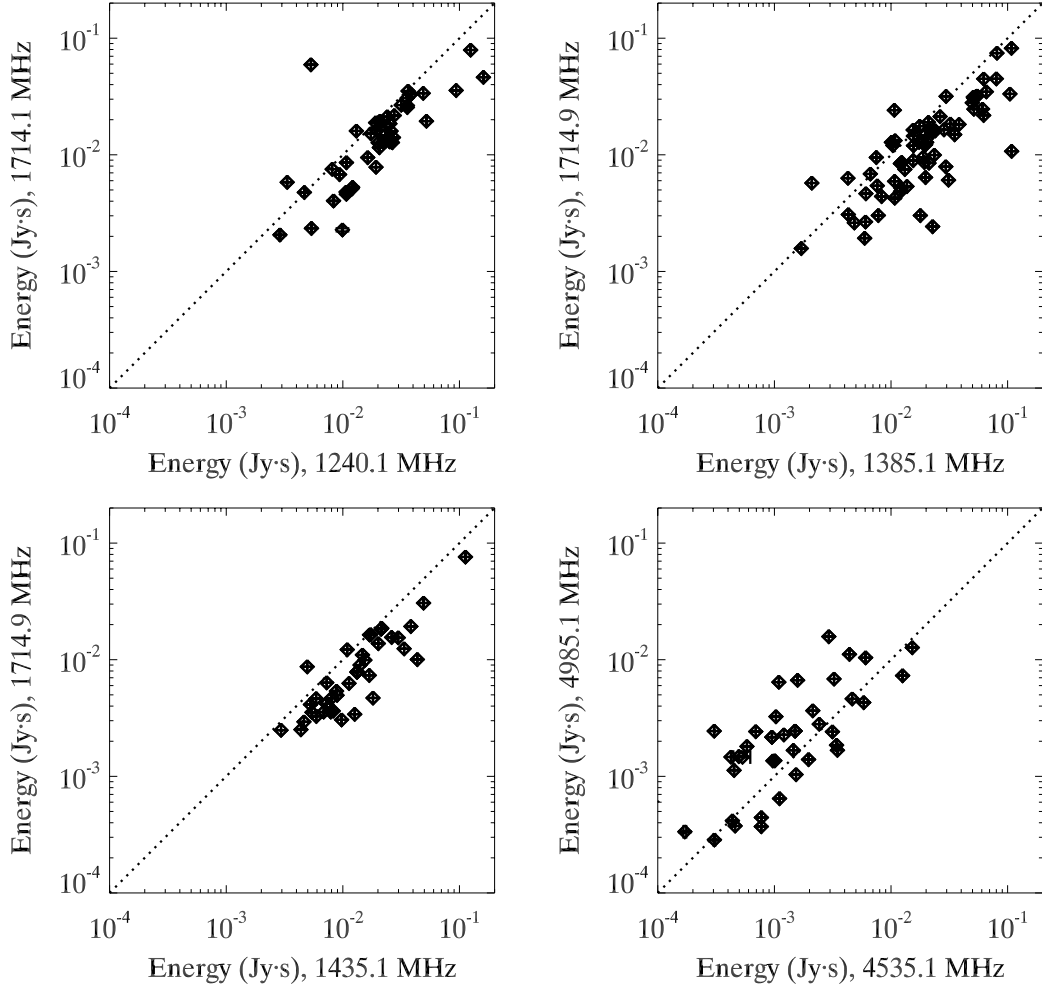


Figure 2.15: High- versus low-frequency microburst energies of simultaneous two-frequency observations. Error bars determined during the microburst fitting process are plotted for both axes. The three data sets utilizing observing frequencies between 1 and 2 GHz have, on average, higher energies at the lower frequencies. The bottom right plot, with observing frequencies between 4 and 5 GHz is an exception to this rule (but see § 2.4.3). Average spectral power law indices have been measured for each data set and are shown in Table 2.5. The dotted line shows the location of high- and low-frequency energy equality.

the largest band separation (1.24 to 1.71 GHz)¹⁵.

Even with the large fluctuations it is clear that the microburst broadening we have observed is different from the $\tau \propto \nu^{-4}$ scattering described in § 1.3.2. The width analysis of Kern (2004) used two different measurements of microburst width and identified two scatter broadening power laws (see discussion in § 2.4.2). His data suggest that the ISM scattering (ν^{-4}) operates in addition to a less-steep scattering law (ν^{-2}). As mentioned above in § 2.4.2, the ISM law corresponds roughly to the lower bound of my width measurements while the less-steep law corresponds more closely to the peak density of my 1.4- to 4.9-GHz width distributions.

The scattering represented by the less-steep law is highly variable in comparison with the ISM scattering. A variable mechanism, or environment, is needed to explain this scattering; the pulsar magnetosphere provides just that. It is not yet clear whether this microburst width variability is intrinsic to the emission process itself or is a result of scattering in the magnetosphere.

¹⁵A small frequency baseline amplifies any fluctuation in widths when performing the power law fit. For example, the width power law index derives from

$$y = \frac{\ln(W_1/W_2)}{\ln(\nu_1/\nu_2)},$$

where subscripts 1 and 2 represent measurements of the high and low frequency bursts, and a frequency ratio near 1 produces a large multiplicative factor. For this reason, the bottom row of Table 2.5 contains very large standard deviations, σ_α and σ_y , which make the values of α and y very uncertain.

Table 2.5: Microburst Frequency Power Laws: Width and Energy

Superscript (Table 2.1)	Freq 1 (GHz)	Freq 2 (GHz)	# Matched Microbursts	$\langle y \rangle^\ddagger$	σ_y^\ddagger	$\langle \alpha \rangle^\parallel$	σ_α^\parallel
a	1.2401	1.7141	46	-2.2	0.9	-1.2	1.8
c	1.3851	1.7149	68	-1.6	2.1	-2.4	2.4
d	1.4351	1.7149	37	-1.8	1.8	-2.7	2.0
g	4.5351	4.9851	41	-0.8	4.7	4.8	8.2

\ddagger Mean and standard deviation of width power law indices, where $W \propto \nu^y$.

\parallel Mean and standard deviation of energy power law indices, where $E \propto \nu^\alpha$.

Energy Measurements

Figure 2.15 shows that, between 1 and 2 GHz, microburst energy is typically larger at lower frequencies. I quantify the energy-frequency relationship with a power law, $E \propto \nu^\alpha$, where α is the spectral index. The large scatter in spectral indices points to an intrinsic fluctuation in the relative energy of high- and low-frequency microbursts. As discussed above for width power law measurements, the small frequency baseline between high and low frequency passbands amplifies any fluctuation in relative energies. Spectral index means for each of the four two-frequency data sets are shown in Table 2.5. Moffett (1997), using simultaneously recorded 1.4 and 4.9 GHz Crab giant pulses¹⁶, measured a distribution of single pulse spectral indices that peaks between -1.5 and -2.0; consistent with my measurements. My results agree well with Popov et al. (2006), who measured a mean spectral index of -2.7 ± 0.1 for Crab

¹⁶Moffett (1997) actually made use of 1.4351 GHz observations that I have also used in this chapter (see Table 2.1 and the observing session from MJD 50193). However, Moffett's simultaneously recorded 4.9-GHz observing session recorded only a small number of pulses and, therefore, was excluded from this study.

giant pulses between 23 and 600 MHz; however, the same authors suggest that the spectrum of individual Crab giant pulses is not well described by a simple power law. For comparison, the Crab average profile spectral index has been measured between 408 and 1606 MHz as -3.1 ± 0.2 (Lorimer et al., 1995).

It should be noted that the observing method introduces a bias for stronger pulses at higher frequency, because the energy threshold used to record only giant pulses is compared exclusively with the energy in the higher frequency band. Additionally, the mean value of α between 4.5 and 5.0 GHz is affected by interstellar scintillation, which alters the pulse power by an unknown function of frequency and time (see § 1.3.3).

2.5 Conclusions

Microbursts are pulse emission microbursts with widths on the order of microseconds. The VLA was used to record Crab pulsar giant pulse microbursts with high time resolution. Main pulses, interpulses, and main pulse precursors were recorded, but a statistically significant sample only of main pulses was obtained. Thus, I have focused my study on characteristics of main pulse microbursts.

I fit the microbursts with a series of fast-rise-slow-decay functions and analyze microburst properties by studying the fitted-function parameters. I find that the function fits the data best at low frequencies. As frequency increases, the number of unresolved bursts increases. I find that the flux of single microbursts varies by up to 2 orders of magnitude on timescales shorter than one pulse period; in contrast, the centroid of the microburst flux distributions

varies by roughly a factor of 2 over hours to days.

I find that all microbursts do not contain the same amount of energy. There is, however, evidence of a break in the flux-width distribution above which the density of microbursts decays rapidly. This flux-width break occurs along a power law that is roughly described by a constant-energy line, $F \propto W^{-1}$. The constant of proportionality (the microburst energy upper bound) decreases with increasing frequency. All microbursts do not have the same duration (width). A wide range of temporal widths (~ 2 orders of magnitude) occur within a short timescale (even within a single pulse). This width variation is too rapid to be caused by the ISM or nebula and must be intrinsic to the pulsar. The maximum density of the energy distribution decreases with increasing frequency; the break in the flux-width distribution moves to lower energies as frequency increases. I compare the high-energy side of the energy distribution with a model of microbursts having uniform energy in the rest frame, $n(E) \propto E^{-2}$, and find that at the highest energies the number of microbursts is less than is suggested by this model.

In simultaneously observed two-frequency observations, I am able to identify corresponding microbursts when the observing bands are both between 1 and 2 or 4 and 5 GHz. Corresponding microbursts could not be identified when the two observing bands were set to 1.4 and 4.8 GHz. The microburst emission bandwidth may be < 4 GHz at these frequencies, or magnetospheric distortions may occur over these wider bandwidths. Both microburst flux and width are well correlated between high and low simultaneously observed frequencies. Between 1 and 2 GHz, lower frequency microbursts are typically

wider and more energetic. Although I was able to identify microbursts between 4 and 5 GHz, the scintillation bandwidth at these frequencies is large enough that intrinsic relative flux and energy cannot be determined without more extensive observations. Microbursts tend to be wider and have greater energy at lower frequencies. I measure width and energy frequency dependence and find my measurements to be roughly consistent with other authors.

CHAPTER 3

ECHOES OF CRAB PULSAR GIANT RADIO PULSES¹

Abstract

We have detected short-lived “echoes” of giant pulses from the Crab pulsar. We observed individual giant pulses with high time resolution, at 1.4 and 4.8 GHz. Over a course of several years, we saw the echoes on only two days (separated by 13 months), and only at the lower frequency. The echo emission follows the giant pulse primary emission by 40–100 μ s. The peak flux of the echo microburst is consistently a factor of 10 less than that of the primary microburst. The echo widths are greater than the primary microburst widths. One of our two echo events lasted no more than four days. The frequency dependence, shorter echo lag time, and echo event lifetime together suggest that these echoes differ from those reported previously. We use simple models to investigate the possibility that the echoes are due to reflection from plasma structures close to the pulsar, possibly close to the interface between the pulsar wind and the outer synchrotron nebula.

¹This chapter has been submitted for publication in *The Astrophysical Journal*: Crossley, J. H., Hankins, T. H., & Eilek, J. A., Echoes from Crab Pulsar Giant Radio Pulses.

3.1 Introduction

The Crab pulsar was discovered in 1968 (Staelin & Reifenstein, 1968), only 15 months after the detection of the first pulsar by Hewish et al. (1968). Among the more than 1700 pulsars presently known² the Crab pulsar is exceptional in many respects including its youth, broadband emission, associated supernova remnant, rapidly evolving structures near the star, and extreme pulse brightness variability. The pulsar lies in the center of the Crab nebula, at a distance of 2 ± 0.5 kpc (Cordes & Lazio, 2002). The nebula and the pulsar have been explored extensively from radio through gamma ray wavelengths. The outer-nebula synchrotron emission is thought to be supported by the interior pulsar wind, which produces a shock at ~ 0.3 pc from the pulsar. Bright, variable “wisp” structures, explored in radio, optical and X-ray (Bietenholz et al., 2004; Hester et al., 2002, 1995; Mori et al., 2002), are interpreted as a product of the pulsar wind shock. The ejecta of the supernova lies at the outer boundary of the synchrotron nebula, and takes the form of large- and small-scale “filaments” which are believed to be ionized by the synchrotron emission from the interior nebula (Sankrit et al., 1998). X-ray observations have revealed a bilateral jet and torus centered on the pulsar, which are collocated with the wisps seen at optical wavelengths (Weisskopf et al., 2000). Pulse broadening variability has been attributed to scattering from evolving nebular plasma (Rickett, 1977).

The flux of radio pulses from the Crab pulsar varies widely, occa-

²Based on the current number of pulsars listed in the Australia Telescope National Facility Pulsar Catalogue: <http://www.atnf.csiro.au/research/pulsar/psrcat/>

sionally reaching more than 1000 times the average pulse amplitude. These sporadic, very luminous *giant pulses* were evident in the discovery of the Crab pulsar (Staelin & Reifenstein, 1968). There are presently only seven pulsars for which giant pulses have been claimed (Soglasnov et al., 2004). The properties of Crab giant pulses have been studied extensively (Hankins et al., 2003; Sallmen et al., 1999; Lundgren et al., 1995). Crab giant pulses have structure on nanosecond timescales (Hankins et al., 2003; Hankins & Eilek, 2007), and typical giant pulse widths are much shorter than the average pulse profile. The fraction of the average profile energy provided by giant pulses is frequency dependent, increasing from 1% at 0.146 GHz to 89% at 0.8 GHz (Sallmen et al., 1999). Crab giant pulses occur at the same rotational phases as the main pulse and interpulse, and may also occur at the phases of the high frequency microbursts (Słowikowska et al., 2005). During observations, we saw giant pulses with energies exceeding a 5σ threshold, where σ is the off-pulse detected noise standard deviation, as often as ~ 1 per second at 1.4 GHz³ with the Very Large Array⁴ (VLA). At higher frequencies the average rate of detectable pulses decreases significantly due to scintillation effects.

Changes in low radio frequency pulse characteristics, including the scattering width, dispersion measure, and rotation measure, have been attributed to plasma variability in the Crab nebula (Lyne & Thorne, 1975; Rankin et al., 1988). A new form of Crab pulse variability was detected by Smith &

³Our high time resolution data acquisition equipment was unable to record all giant pulses at this rate. See §3.2.

⁴The Very Large Array is an instrument of the National Radio Astronomy Observatory, a facility of the National Science Foundation operated under cooperative agreement by Associated Universities, Inc.

Lyne (2000) and Backer et al. (2000)—an irregular “echo” or “ghost replica” was detected following the main pulse and interpulse. We define a pulse *echo* as emission that appears in many pulse periods, lags behind the normal pulse microburst in rotational phase, and has characteristics that correlate with the primary emission. We refer to the normal pulse microburst preceding the echo as the *primary* microburst. The primary-to-echo time-of-arrival (TOA) difference is referred to as the *echo delay*. Smith & Lyne (2000), Backer et al. (2000), Lyne et al. (2001), and Dickerson (2003) all reported an echo event that began in 1997 August, with echo emission following the main pulse and interpulse by 7 ms; the echo delay decreased over a period of 50 days until the two microbursts merged. Lyne et al. (2001) found this echo event in archival timing data along with 16 other Crab echo events that occurred between 1984 and 1998. Many of the echo events occurred in pairs and were symmetrical in time: the echo delay decreased daily to a minimum, where the echo merged with the primary; the next echo then separated from the primary, and the echo delay increased; the echo eventually disappeared. Smith & Lyne (2000) and Backer et al. (2000) proposed that the echoes originate from pulse refraction in transient, ionized filaments in the Crab nebula supernova ejecta shell. This model accounts for the decreasing, and subsequently increasing, echo delay behavior because the light travel time from pulsar to transient filament to Earth will reach a minimum when the filament is closest to the Earth-pulsar sight line.

We made high-time-resolution observations of Crab giant pulses at 1.4 and 4.8 GHz on 20 days between 1993 and 1998. We found echoes on only two days: 1996 October 14 and 1997 November 26. The latter date coincides

with the period of enhanced dispersion measure and the echo event reported by Backer et al. (2000) and Lyne et al. (2001). The strength of giant pulses makes pulse averaging unnecessary, thus allowing us to probe the variability of echo emission on shorter timescales than was available in previous average profile studies. Furthermore, our observations span a range of higher radio frequencies than previous studies, allowing us to explore a new regime of echo frequency dependence. The echo emission we observed at two frequencies in 1996 October differs from the echo emission reported by Backer et al. (2000) and Lyne et al. (2001). This echo event has a shorter lifetime and, a smaller echo delay, and it is strongly frequency dependent. The origin of our echoes can be explained by a modification to the nebula refraction model of Backer et al. (2000) and Lyne et al. (2001).

In §3.2 we describe the details of our observations. In §3.3 we describe our microstructure analysis technique. We discuss the results of this analysis in §3.4, and in §3.5 we discuss implications of our findings on the current echo model and our understanding of the Crab nebula. Conclusions are provided in §3.6.

3.2 Observations

Our giant pulse observations were made at the Very Large Array in several baseline configurations in the phased-array mode, where individual antenna delays are adjusted in real-time so as to restore the original wave front. Even in the D-array configuration, the VLA at both 1.4 and 4.9 GHz forms such a small angular beam that, when pointed at the pulsar, it resolves out most of the structure of larger angular size in the Crab nebula. We therefore

attain a much lower system temperature on the Crab pulsar than is possible with a single-dish telescope of equivalent collecting area. The software package TEMPO (Taylor & Weisberg, 1989) was used in prediction mode to create a pulsar timing model based on the monthly Crab pulsar ephemeris published by Jodrell Bank Observatory⁵. The model was then used to set a period-synchronous gate at the pulse phase of either the Crab main pulse or interpulse. For each pulsar period the signal within the gate was square-law detected with a 200- μ s time constant. If the total energy of the giant pulse within the gate exceeded a preset multiple (typically 7) of the root-mean-square off-pulse noise, two orthogonal circular polarization signals were digitally sampled by a LeCroy oscilloscope at a rate of 100 MHz. The signals were then transferred to disk for subsequent off-line coherent dedispersion (Hankins, 1971). During the transfer time, 10–30 s, the data acquisition was disabled, and no pulses could be captured.

For six of the nine observations we present here, we utilized two distinct frequency bands simultaneously (usually 4.9 and 1.4 GHz) by splitting the VLA into two independent sub-arrays. Since nebular and interstellar dispersion causes the lower frequency pulsar emission to arrive later, the gated portion of the higher frequency pulse was compared against the energy threshold; if the threshold was exceeded, the pulse was recorded, and after the appropriate digitally controlled dispersion delay (to account for the dispersion delay to the lower frequency), the digital oscilloscope was triggered again to record the signal in the lower frequency band. Off-line coherent dedispersion utilized the

⁵<http://www.jb.man.ac.uk/~pulsar/crab.html>

Table 3.1: Observations used in Crab giant pulse echo analysis.

Date	Center Freq		Giant Pulses	Time span ^a (min)	Max (Min) SNR	
	(GHz)				ν_1	ν_2
	ν_1	ν_2				
1996 Oct 12	1.4	4.9	40	30	1128 (4.4)	664 (11)
1996 Oct 12 ^b	1.4	4.9	4	45	1033 (211)	389 (53)
1996 Oct 14	1.4 ^c	4.9	62	170	1999 ^d (9) ^d	1054 (21)
1996 Oct 16	1.4	4.9	4	20	643 (55)	212 (42)
1996 Oct 16	1.4	4.6	11	43	57 (8)	270 (16)
1997 Nov 19	4.8		1	n/a	154	
1997 Nov 26	1.4 ^e		14	15	161 ^d (36) ^d	
1997 Nov 26	4.8		4	15	269 (42)	
1997 Nov 26	4.94	4.89	3	18	113 (53)	70 (47)

^ameasured from first to last recorded pulse

^binterpulse observation

^c“Observation A”, echoes present

^dIncludes only pulses with good residuals after χ^2 minimization and clearly distinguishable echo and primary microbursts (same pulses used in Figures 3.3 through 3.6)

^e“Observation B”, echoes present

Note — Observations are of the main pulse except where noted. 50-MHz bandwidth was used at each center frequency. The measured SNR is a ratio of the smoothed primary microburst maximum flux and the smoothed off-pulse noise. The maximum and minimum SNR for each observation and each frequency are shown.

dispersion measure extrapolated from the Jodrell Bank Crab pulsar ephemeris as well as cross correlation of the detected intensity to obtain precise dispersion delays.

In Table 3.1 we present two sets of Crab pulsar observations in which we have seen echoes. The first set of observations was obtained over a five-day period in 1996 October; giant pulses were recorded simultaneously at center frequencies 1.435 and 4.885 GHz (at 1.435 and 4.635 GHz on 1996 October 16), with 50-MHz bandwidth at each frequency. A total of 121 giant main pulses

were observed along with 4 giant interpulses. Echoes were detected only on one day, 1996 October 14, and only at 1.4 GHz. The second set of observations was obtained on two days in 1997 November. A total of 19 giant pulses were observed with a single 50-MHz bandpass centered either at 1.435 or 4.885 GHz; 3 giant pulses were observed simultaneously at 4.935 and 4.885 GHz with 50-MHz bandwidth at each frequency. Again, echoes were observed only on one day, 1997 November 26, and only at 1.4 GHz.

This paper focuses primarily on echo emission observed at 1.4 GHz on 1996 October 14 and 1997 November 26. For convenience, these 1.4 GHz observations are referred to as *Observation A* and *Observation B*, respectively, in the remainder of the paper. The other observations shown in Table 3.1 are discussed only in so far as they provide insight into Observations A and B. A subsequent paper will present an in-depth study of a larger set of high-time resolution Crab pulsar observations, including the observations in Table 3.1.

3.3 Microburst Fitting

After dedispersion and smoothing, a region of weak, persistent emission trailing the otherwise normal, strong giant pulse emission is clearly visible in all but two pulses in Observation A and in all pulses in Observation B, examples of which are shown in Figure 3.1. We term this emission the echo and primary emission, respectively, as mentioned in §3.1. The primary emission is similar in variability and component complexity to Crab giant pulse emission observed at 1.4 GHz on other occasions (when the echo emission was absent). Crab giant radio pulses vary from one pulse to the next in both rotational phase and in the number of components present (Sallmen et al., 1999). However, the

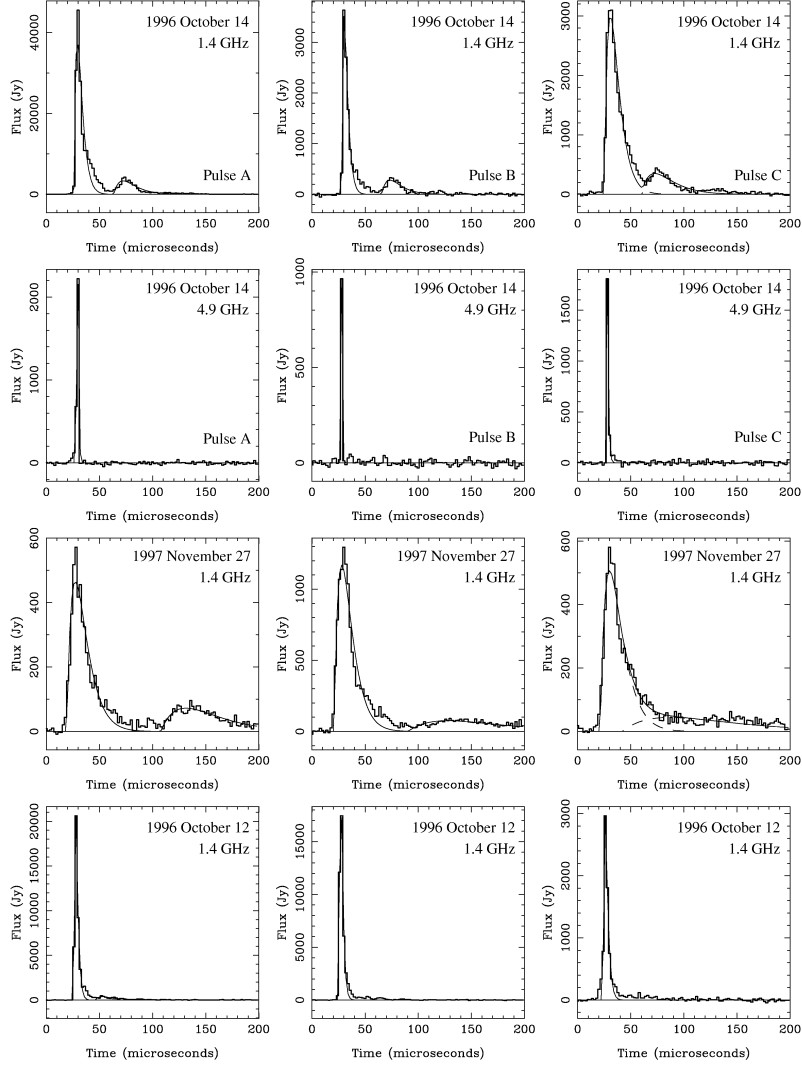


Figure 3.1: Example giant pulses. All pulses are plotted with a time resolution of $2\ \mu\text{s}$. The dashed lines show the fitted individual terms, $F_i(t)$, from equation (3.1); the thin solid line is the sum of the fitted pulse microbursts, $F(t)$. The first row contains pulses observed at 1.4 GHz on 1996 October 14; echoes can be seen following the primary emission. The second row shows the same three pulses (labeled A, B, and C for emphasis) but now at 4.9 GHz. The third row shows pulses observed at 1.4 GHz on 1997 November 27; echoes follow the primary. The bottom row shows giant pulses observed at 1.4 GHz on 1996 October 12, when no echo is present. The tail of emission following the main pulse on 1996 October 12 is typical of Crab pulses at 1.4 GHz and is not echo emission (see §3.3); the absence of echo emission on this day and on 1996 October 16 allows us to constrain the lifetime of the echo event to ≤ 4 days.

echo emission we observe correlates strongly, and in multiple ways (see §3.4), with the primary emission for the full duration of Observation A (170 minutes) and Observation B (15 minutes).

In 1996 October, the total lifetime of the echo emission is constrained to ≤ 4 days by giant pulse observations which show no echo emission on 1996 October 12 and 1996 October 16 (Table 3.1). Echoes with a signal-to-noise ratio of ~ 10 would have been clearly visible in any of the observations listed in Table 3.1. For the brightest pulses observed on non-echo days, a signal-to-noise ratio of ~ 10 would correspond to an echo with peak flux of approximately 1 percent the primary peak flux; the echoes we actually observe have a peak flux of 10% the primary peak flux (see §3.4). We have determined that a weak “tail” of emission frequently follows Crab pulses at ~ 1.4 GHz, as can be seen in the 1996 October 12 data shown in Figure 3.1; this same “tail” was found in Crab observations recorded in 1998, long after the echo events presented here. We do not believe this tail to be an echo.

Individual giant pulses at 1.4 GHz are often composed of several components, each of which has a fast-rise-slow-decay shape. To study the microstructure intensity properties of the pulses observed, we therefore subtract the off-pulse mean intensity, F_{off} , and fit the remaining pulse flux as a sum of microbursts with a fast-rise-slow-decay shape:

$$F(t) = \sum_{i=1}^n F_i(t) = \sum_{i=1}^n A_i(t - t_{0i}) e^{-(t-t_{0i})/\tau_i}. \quad (3.1)$$

This microburst functional form is a modification of the best-fit shape found by Rankin et al. (1970); it was used by Sallmen et al. (1999) in their Crab giant pulse analysis. From equation (3.1), a fitted pulse microburst i has a maximum

flux $F_i = A_i \tau_i e^{-1}$ at time $t_{\text{TOA } i} = t_{0i} + \tau_i$, total energy $E_i = A_i \tau_i^2$, and width $W_i = 3\tau_i$ (defined as the length of time that the flux exceeds $F_i e^{-1}$). We define the time-of-arrival of a pulse microburst as $t_{\text{TOA } i}$. Examples of fitted pulses are shown in Figure 3.1. Looking ahead to the analysis of §3.5, we note that if the energies of two microbursts are equal, then the flux and width ratios for the two microbursts are inversely equal: $E_1 = E_2 \Rightarrow F_1/F_2 = W_2/W_1$.

We employ χ^2 minimization to find the best fit of $F(t; A_i, t_{0i}, \tau_i)$ to each pulse (Press et al., 1992). For each term in $F(t)$, we provide initial estimates for the parameters A_i , t_{0i} , and τ_i . The smallest value of n , where $1 \leq n \leq 6$, is chosen such that the uncertainties in t_{0i} , F_i , and W_i are small and residuals of $F(t)$ are described as closely as possible by a normal distribution with zero mean and standard deviation $\sigma_F(t)$, where $\sigma_F(t)$ is the standard deviation given by the radiometer equation:

$$\sigma_F(t) \equiv \begin{cases} [F(t) + F_{\text{off}}]/\sqrt{\Delta\nu \Delta t} & , \quad t \in \text{on-pulse region} \\ \sigma_{\text{off}} = F_{\text{off}}/\sqrt{\Delta\nu \Delta t} & , \quad t \in \text{off-pulse region} \end{cases}. \quad (3.2)$$

Here $\Delta\nu$ is the bandwidth and Δt is the post-detection smoothing time.

In computing χ^2 for a given set of parameters of $F(t)$, every j 'th data sample must be assigned a standard deviation, $\sigma_{\chi j}$, to represent its uncertainty. After experimenting with a variety of methods for calculating $\sigma_{\chi j}$, we found that using the constant off-pulse standard deviation gives fits with the best residuals after χ^2 minimization. Using $\sigma_{\chi j} = \sigma_F(t)$ as the standard deviation unweights the strongest parts of the pulse and χ^2 minimization yields poor fits. Thus, the standard deviation $\sigma_{\chi j}$ used to compute χ^2 is not formally the same as the standard deviation, $\sigma_F(t)$; after χ^2 minimization we judge the fit according to $\sigma_F(t)$ to avoid non-physical χ^2 minima.

When the final fit of a pulse is attained, an $m \times m$ covariance matrix is returned (m is the number of parameters fitted; m increases by 3 for each microburst used), providing the covariance between each set of fitted parameters. We assume that the measurement errors in the data are normally distributed, thus allowing us to use the diagonal elements of the covariance matrix as the standard deviations in the respective parameters (Press et al., 1992).

The majority of flux in most pulses is accounted for by fitting two microbursts to the pulse—one to the primary and one to the echo. Many pulses contained low-level emission not accounted for by the two microburst fits. Very often low-level flux could be seen between the primary and echo, and less often preceding the primary. While this flux can be fitted by using two superimposed microbursts, the parameters (t_{0i} , F_i , and W_i) of the superimposed microbursts often have very large uncertainties, revealing a degeneracy in the parameter fits (a trough or valley in χ^2 -space); for the purpose of the analysis of §3.4, we sought to avoid superimposing microbursts as much as possible, thus exchanging better residuals for high precision parameter fits. Recurring unfitted flux features such as these suggest that a function with a slower rise and decay may provide a better fit.

In the analysis of the next section, only those pulses are used for which two or more microbursts, not strongly overlapping, are fitted to at least the primary and echo (with the exception of the average autocorrelation, which includes almost all pulses). Only two pulses, one in Observation A and one in Observation B, were fitted with 3 rather than 2 microbursts; for both pulses the extra microburst accounts for emission between the primary and echo.

For those two pulses that do contain more than two fitted microbursts, the analysis below regards the microburst with the maximum peak flux as the primary microburst and the latest microburst in time as the echo microburst, consistent with the definitions given in §3.1. We thus limit the analysis to 33 out of 62 observed pulses in Observation A, and 9 out of 14 observed pulses in Observation B.

3.4 Results

3.4.1 Frequency Dependence

Echo emission is seen in 1.4-GHz pulses on 1996 October 14 but not in simultaneously recorded 4.8-GHz pulses. This is demonstrated by plots of the individual pulses (for example see Figure 3.1) and the average autocorrelation function of each frequency in Figure 3.2. The prominent shoulder extending out $50 \mu\text{s}$ at 1.4 GHz coincides with the echo delay, $t_{\text{TOA echo}} - t_{\text{TOA primary}}$, deduced from pulse microburst fitting, discussed below. The smaller shoulder around the 4.8-GHz peak does not correspond to a persistent emission microburst, but arises from pulse structure; the 4.8-GHz shoulder reveals that the giant pulses at this frequency have a width of $\sim 15 \mu\text{s}$.

We searched for a 4.8-GHz echo in individual pulse data from 1996 October 14 and 1997 November 26, focusing especially on the echo delay expected from a purely geometrical delay and the echo delay expected from a purely dispersive delay (see §3.5 for details). No echoes were found in the 4.8-GHz individual pulse data. The 4.8-GHz 1996 October 14 observation contained 62 giant pulses with signal-to-noise ratios (SNR's) of up to 1054, where SNR is defined as the ratio of the smoothed pulse maximum flux to the

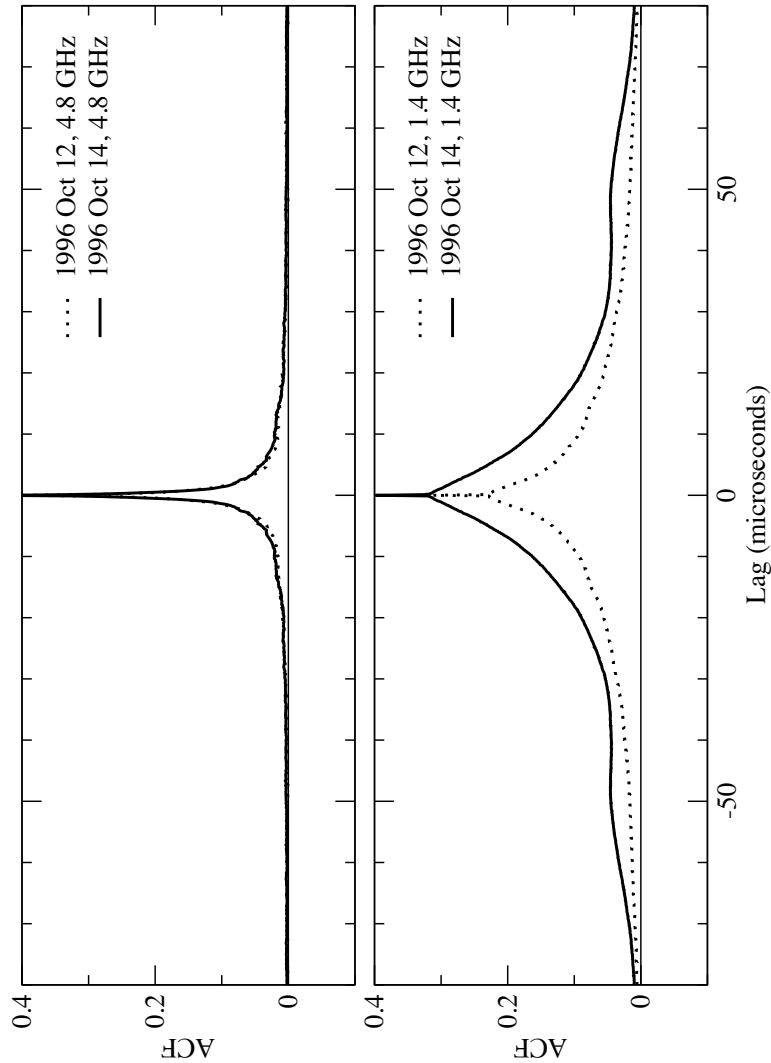


Figure 3.2: Average intensity autocorrelation functions (ACF's) for 1996 October 12 and 1996 October 14 at 4.8 and 1.4 GHz. These ACF's are averaged over all pulses for which both the high and low frequency pulses have a $\text{SNR} > 5$; this includes all 40 pulses for 1996 October 12 and 61 out of 62 pulses for 1996 October 14. The echo emission at $50\text{-}\mu\text{s}$ lag is clearly visible in the 1.4-GHz autocorrelation, but no echo is visible at the same lag in the 4.8-GHz data. The feature at $\sim 12\text{-}\mu\text{s}$ lag at 4.8 GHz does not correspond to a consistent emission microburst but is a result of pulse structure. The flux “spike” at zero lag is truncated by the upper bound of the plot. The ACF's have been smoothed to $1\text{-}\mu\text{s}$ resolution.

smoothed off-pulse detected noise. Echoes were detected simultaneously in 1.4-GHz pulses with SNR's as low as 9. The 4.8- and 4.9-GHz 1997 November 27 observations contained 7 giant pulses with signal-to-noise ratios of up to 269. Echoes were detected on the same day in 1.4-GHz pulses with SNR's as low as 36.

3.4.2 Analysis of Microburst Fits

The consistency of the echo delay in Observations A and B is shown in Figure 3.3. The average echo delay for Observation A is $45 \pm 4 \mu\text{s}$. The average echo delay for Observation B is $92 \pm 18 \mu\text{s}$. It is known that the TOA of individual pulses varies randomly with rotational phase within the pulsar average profile (Hankins et al., 2003). The Observation A and Observation B pulses show this expected random TOA variation. However, the TOA difference between the primary and echo emission is independent of the pulsar rotational phase.

The maximum flux of the echo emission, F_{echo} , is plotted against the maximum flux of the primary emission, F_{primary} , in Figure 3.4. In both observations the maximum echo flux is consistently a factor of 10 lower than the maximum primary flux. The Observation B flux distribution overlaps the weak end of the Observation A flux distribution. This is not surprising considering that Observation B occurred during the strong scattering event that took place during 1997 November (Backer et al., 2000).

The e^{-1} width of each echo microburst, W_{echo} , is plotted against the e^{-1} width of each primary microburst, W_{primary} , in Figure 3.5. The plot shows

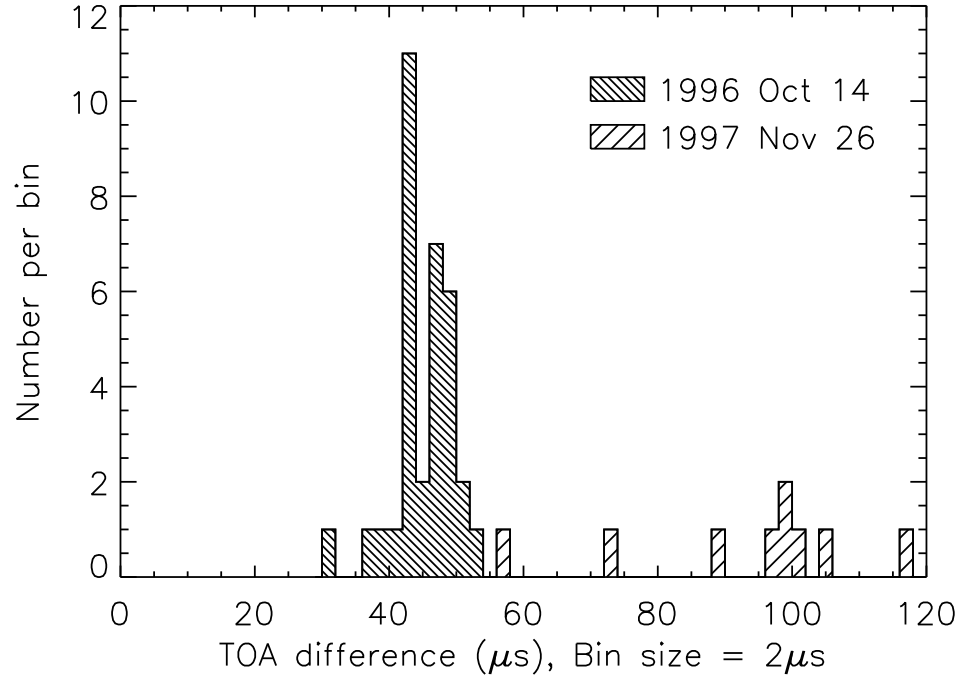


Figure 3.3: Histogram of the time-of-arrival (TOA) difference between the primary and echo microbursts, $t_{\text{TOA echo}} - t_{\text{TOA primary}}$, for 1996 October 14 and 1997 November 27 at 1.4 GHz. The TOAs are determined as described in §3.3. Only pulses with two or more, not strongly overlapping, microbursts fitted to the primary and echo are used in this plot; 33 pulses are plotted for 1996 October 14 and 9 pulses for 1997 November 27. Individual pulses have primary-to-echo TOA uncertainties of less than $6\mu\text{s}$. The 1996 October 14 and 1997 November 27 pulses have a mean echo delay of 45 ± 4 and $92\pm 18\mu\text{s}$, respectively.

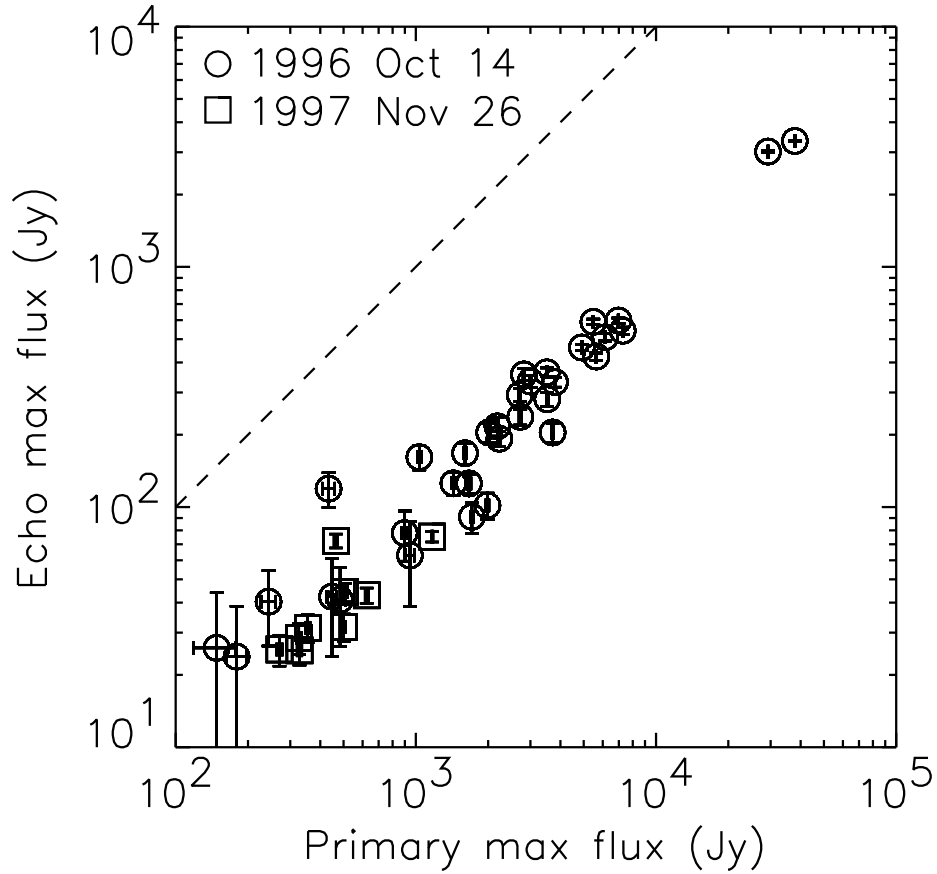


Figure 3.4: Plot of maximum echo flux, F_{echo} , versus maximum primary flux, F_{primary} , in units of Janskys for 1996 October 14 and 1997 November 27 at 1.4 GHz. The pulses used here are the same as those used in Figure 3.3. Note that the echo microburst peak flux is consistently a factor of 10 less than the peak flux of the primary microburst. The dashed line shows the location of primary and echo maximum flux equality.

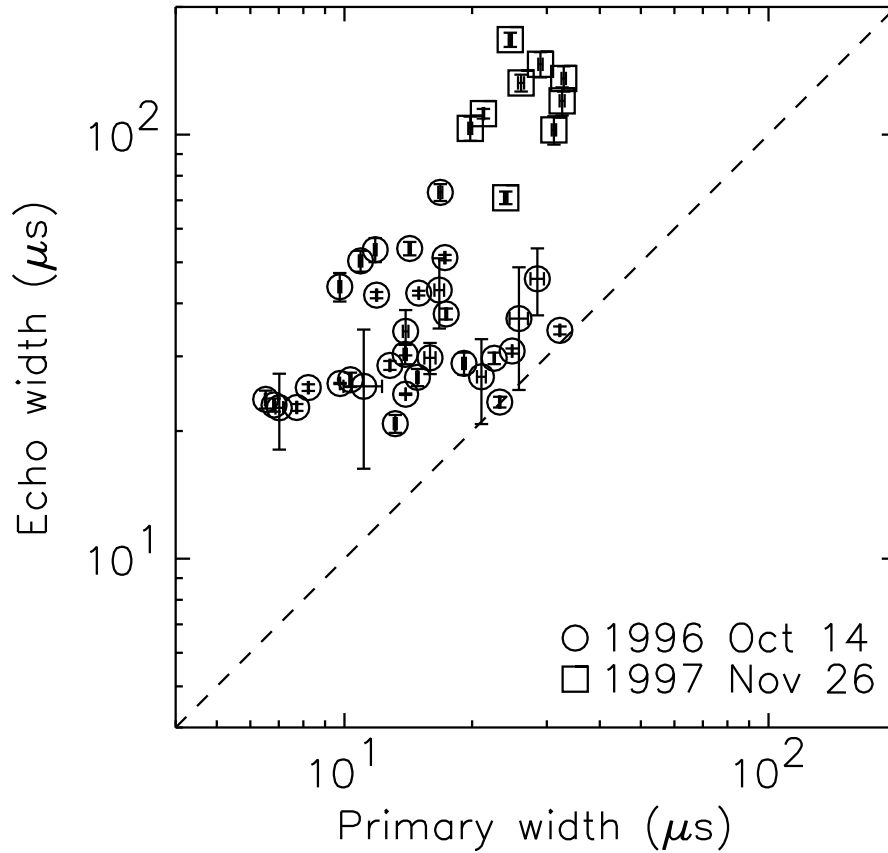


Figure 3.5: Plot of echo microburst width, W_{echo} , versus primary microburst width, W_{primary} , for 1996 October 14 and 1997 November 26 at 1.4 GHz. The pulses used here are the same as those used in Figure 3.3. The 1996 October 14 and 1997 November 27 distributions are disjoint, with the 1997 November 27 echoes being wider than all but one of the 1996 October 14 echo microbursts. The dashed line shows the location of primary and echo width equality. The average ratio of echo-to-primary width is 2.54 ± 1.07 for 1996 October 14 and 4.61 ± 1.20 for 1997 November 27.

disjoint distributions for Observations A and B; this is not surprising considering the enhanced scattering during 1997 November. The ratio of the echo-to-primary widths, $W_{\text{echo}}/W_{\text{primary}}$, ranges from 1.0 to 6.8, with the majority of the Observation B pulses having wider echo emission; the average ratio of echo-to-primary width for both Observation A and B is ~ 3.5 .

The energy of each echo microburst, E_{echo} , is plotted against the energy of the corresponding primary microburst, E_{primary} , in Figure 3.6. For each pulse plotted the echo microburst energy is less than the energy in the primary microburst by approximately a factor of 4 for Observation A and a factor of 3 for Observation B. That the echoes have less total energy than the primary microbursts does not follow immediately from the fact that the echo flux maximum is less than the primary flux maximum, since the microburst energies also depend on the microburst widths, W_i . A necessary condition for the small-angle refraction model discussed in §3.5 is that the echo energy is less than the primary energy. We note that the strong echo-primary energy and maximum flux correlations suggest that the echo emission is not intrinsic to the star, since microstructure intensity is usually observed to be highly variable.

We find no temporal evolution of the pulse characteristics discussed in this subsection for either Observation A or Observation B.

3.4.3 Polarization

The pulses of all observations listed in Table 3.1 are polarized with an average degree of polarization for each observation and each frequency ranging from 12 to 22 percent. The standard deviation in the degree of polarization

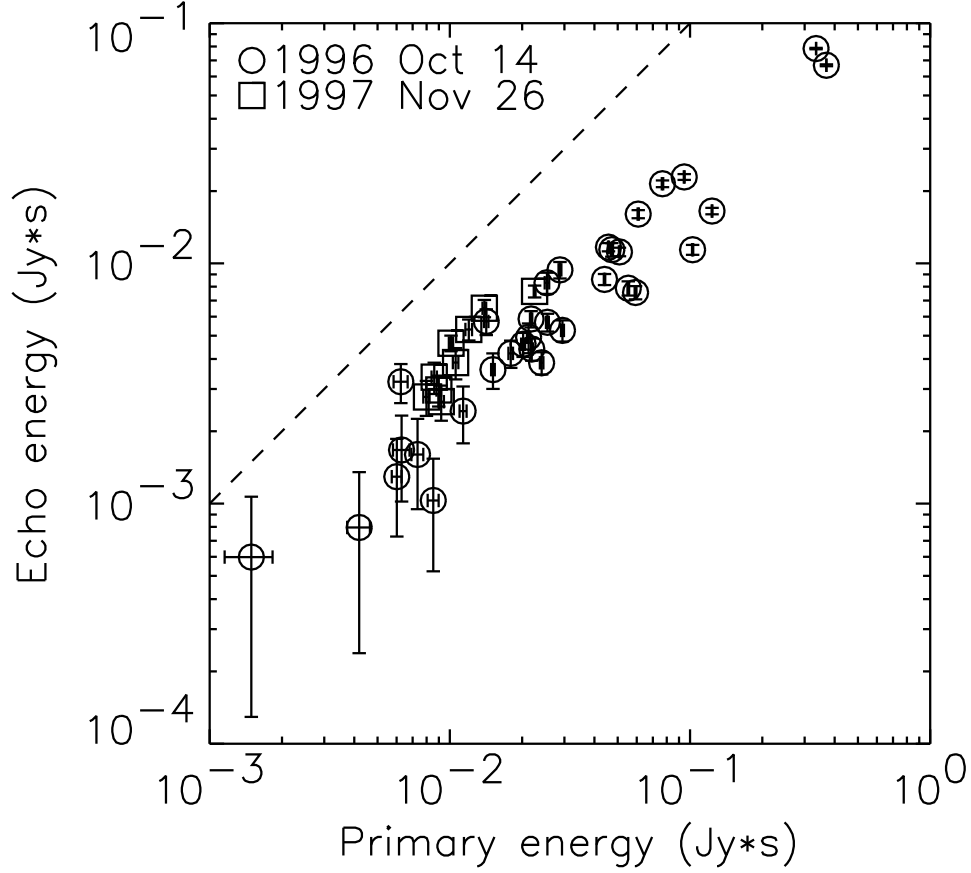


Figure 3.6: Plot of echo energy, E_{echo} , versus primary energy, E_{primary} , for 1996 October 14 and 1997 November 27 at 1.4 GHz. The pulses used here are the same as those used in Figure 3.3. The i 'th microburst energy is calculated by integrating over $F_i(t)$ in the exponential fitting function, equation (3.1). The dashed line shows the location of primary and echo energy equality. The average ratio of echo-to-primary energy is 0.25 ± 0.09 for 1996 October 14 and 0.38 ± 0.6 for 1997 November 27.

measured off-pulse is approximately 5 percent for all pulses observed. The strongest polarized flux is always concurrent with the strongest total intensity flux; the type of polarization (circular or linear) and the time evolution of the polarized flux are inconsistent from one giant pulse to the next. We find that echo microbursts have approximately the same degree of polarization as the primary microbursts. With the exception of 4.9-GHz giant pulses from 1996 November 26, all 4.6 to 4.9-GHz observations have an on-pulse degree of polarization that is approximately 1 to 7 percent larger than the 1.4-GHz giant pulses, which is within instrumental calibration uncertainty. The change in Faraday rotation over 50 MHz is 8.1° at 1.4 GHz and 0.19° at 4.9 GHz, using a rotation measure of 43 rad m^{-2} (Rankin et al., 1988); hence, no significant depolarization from Faraday rotation is expected.

3.5 Discussion

Echoes from the Crab pulsar seen in previous studies were explained as refraction within evolving plasma structures in the Crab nebula (see §3.1). However, the echo events we observed in Observations A and B differ in several important ways from the echoes seen in previous studies.

The strength of giant pulses allows us to avoid the loss of individual pulse information inherent in the pulse averaging used in other echo observations. The main pulse average profile width at 318 MHz and 430 MHz is $\sim 0.5 \text{ ms}$ and $\sim 0.3 \text{ ms}$, respectively (Rankin et al., 1970); previous Crab echo studies (Lyne et al., 2001; Backer et al., 2000; Smith & Lyne, 2000) were not sensitive to the small echo delays we report in §3.4. At 1.5 and 5.5 GHz the average profile width is $0.5 \pm 0.2 \text{ ms}$ and $0.3 \pm 0.08 \text{ ms}$ respectively (Cordes et al.,

2004). Although single pulse widths tend to decrease with increasing frequency, pulse phase variability keeps average profile widths above ~ 400 MHz approximately constant over a large range in frequency (Cordes et al., 2004; Moffett & Hankins, 1996). Therefore, even at these higher frequencies, the echoes we report are only visible in individual, coherently dedispersed giant pulse data.

3.5.1 Echo Event Lifetimes

Lyne et al. (2001) observed echo events with lifetimes ranging from 6 to 50 days. Our Observation A echo event is constrained to less than or equal to 4 days by observations two days before and after which show no echoes. Thus the Observation A echo event has the shortest lifetime of any Crab echo yet observed. As discussed in §3.5.5, this same lifetime is expected for a refraction event caused by Crab nebula wisps. Since we have no other 1.4-GHz observations within several months of Observation B, we cannot constrain the duration of this echo event.

3.5.2 Echo Broadening

In §3.4 we found that the ratio of echo-to-primary microburst width is ~ 3.5 for both Observation A and B. Two propagation phenomena could account for the enhanced echo microburst width: dispersion and scattering. Using dedispersed dynamic spectra, for example see Figure 3.7, we find no evidence that the echo microbursts have a higher dispersion measure than the primary microbursts. The spectra show no dispersion delay changes greater than $5 \mu\text{s}$ across the passband. This places an upper limit on the change in dispersion measure between the primary and echo microbursts, $\Delta\text{DM} < 0.04 \text{ pc} \cdot \text{cm}^{-3}$.

We conclude that dispersion does not account for the enhanced echo width.

The larger echo width may have resulted from enhanced turbulent scattering along the echo ray path. Scattering from plasma turbulence would tend to spread the pulse energy in time and result in broader pulse emission and lower peak flux; the total pulse energy should not be affected. Crab pulse scattering variability has been attributed to changes in the nebula plasma (Rickett, 1977; Isaacman & Rankin, 1977), and it seems likely that a plasma density enhancement significant enough to refract pulsed emission (see §3.1 and §3.5.4) might also be turbulent enough to contribute to pulse scatter broadening.

3.5.3 Energy and Power Loss in Reflection

From §3.4 it is clear that the echoes we observed contain less energy than the primary microbursts. Under the refraction (or reflection) model this energy difference can be explained by a number of mechanisms: partial reflection where some of the energy is transmitted through the reflecting medium; reflection of only a small part of the pulsar beam by a reflecting medium that is small in size; reflection from a curved surface that broadens the reflected beam. In this subsection we explore the possibility that energy loss is due to a curved reflection surface.

Consider the simple case of a spherical reflector located much closer to the pulsar than the earth so the earth-pulsar distance, D_o , is approximately equal to the earth-reflector distance, $D_i \approx D_o$, where we use subscripts i and o for “image” and “object”, respectively. From geometrical optics we know that reflection from a spherical surface produces a demagnified virtual image within

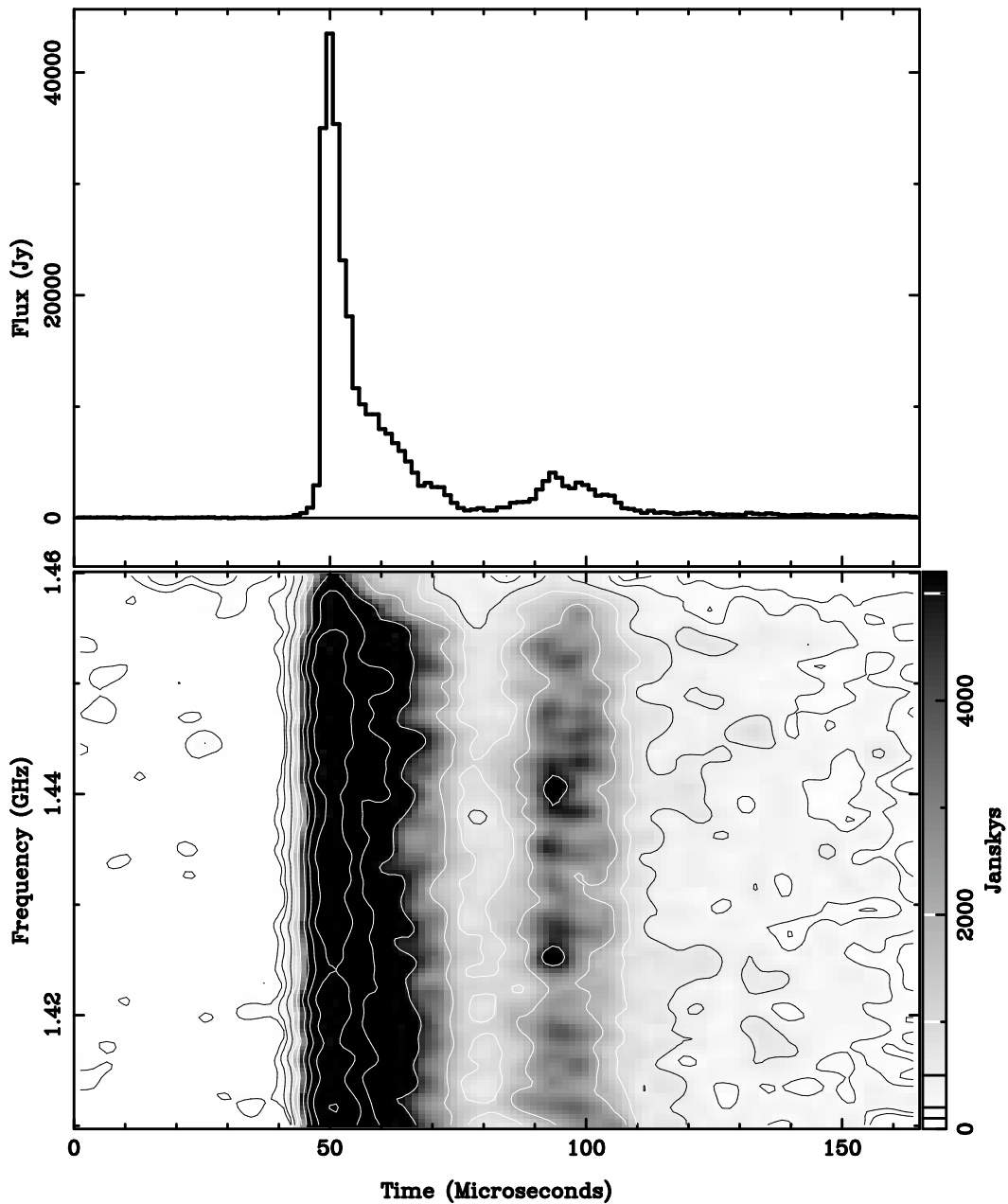


Figure 3.7: The dedispersed total intensity and dynamic spectrum of one pulse are shown. The total intensity time resolution is $1.28 \mu\text{s}$; the dynamic spectrum resolution is approximately $10 \mu\text{s}$ and 3.1 MHz . The dynamic spectrum reveals that the dispersive time of arrival delay for the echo microburst varies by $< 5 \mu\text{s}$ across the 50 MHz band. This equates to an upper limit on the difference in dispersion measure between the primary and echo microbursts of $0.04 \text{ pc} \cdot \text{cm}^{-3}$.

the spherical surface. The location and apparent size of the reflected image obeys the transverse magnification relation,

$$\frac{d_i}{d_o} = -\frac{x_i}{x_o}, \quad (3.3)$$

and the mirror formula,

$$\frac{1}{x_o} + \frac{1}{x_i} = -\frac{2}{R_c}. \quad (3.4)$$

Here d_i and d_o are the transverse sizes of the image and object respectively, and x_i and x_o are the distances from the surface of the reflector to the image and object respectively (when the origin is at the reflecting surface). R_c is the radius of curvature of the reflecting surface. We know neither d nor x for both the object and image; we now proceed to make use of equations (3.3) and (3.4) to relate R_c to the image-to-object (echo-to-primary) flux ratio, which we do know.

An observer sees two sources of radiation, the pulsar and its reflection. These two unresolved sources are identical save for their observed flux and pulse time of arrival (ignoring additional echo scattering for the moment). The flux of the reflection, F_i , will be less than the pulsar flux, F_o , because the flux of a radiating source decreases with the square of the distance from the source ($F_i \propto D_i^{-2}$) and because the curved surface of the reflector widens the pulsar beam in the process of reflection. To connect this flux loss to R_c , we note that the observer cannot discern between a demagnified ($d_{i1} < d_o$) image at the pulsar distance (D_o) and an equal size ($d_{i2} = d_o$) image farther away. The angular size of the image, ξ_i , is assumed to be the same in either case, so that $d_{i1} = \xi_i D_o$ and $d_{i2} = d_o = \xi_i D_i$. Combining this with equation (3.3) and (3.4)

we obtain

$$R_c = \frac{2x_o}{\sqrt{F_o/F_i} - 1}. \quad (3.5)$$

To determine the energy loss factor F_o/F_i we must account for the fact that the echo microbursts are broadened more than the primary. Since scatter broadening lowers the peak flux (but not the total energy), we want to remove the effect of this scattering before making use of equation (3.5); after removal, the remaining difference between the flux maxima is a result of the energy loss of the spherical reflector.

From §3.3 and §3.4 we know that if the echo is a duplicate of the primary, with the same total energy but with different degrees of scatter broadening, then $W_{\text{echo}}/W_{\text{primary}} = F_{\text{primary}}/F_{\text{echo}} \sim 3.5$. What we actually observe is $F_{\text{primary}}/F'_{\text{echo}} \sim 10$. The observed echo flux, F'_{echo} , is less than the scatter broadened echo flux, F_{echo} , telling us that some sort of energy loss has occurred in the observed echo. Upon taking the ratio, we have $F_{\text{echo}}/F'_{\text{echo}} = F_o/F_i \sim 2.9$; this is the energy loss factor that we attribute to reflection from a spherical surface.

If we assume the reflection takes place in the vicinity of the Crab wisps (§3.5.5), then we can approximate the pulsar-wisp distance from radio images to be roughly $x_o = 0.3 \text{ pc}$ (Bietenholz et al., 2004). Substituting this in equation (3.5), we obtain

$$R_c = 2.8x_o \approx 0.84 \text{ pc}.$$

The radius of curvature needed on the reflector to obtain the energy loss we observe is a few times the distance of the reflector from the pulsar.

3.5.4 Echo Frequency Dependence

Backer et al. (2000) found a ratio of echo to primary energies of 0.02–0.06 at 327 MHz and ~ 0.5 at 610 MHz. We have carefully searched our 4.8-GHz data for echo emission, taking into consideration two mechanisms that could affect echo emission: a geometric echo delay and additional echo dispersion.

Echo Delay

If the echo delay is due only to the difference in the light travel time along the direct and refraction paths, the echo delay will be the same at all frequencies. If the echo delay is due in part or in whole to the difference in the column density of electrons along the direct and refraction paths, we can expect the echo delay to depend on frequency as

$$\Delta t_{\text{TOA}} \propto \frac{1}{\nu^2}.$$

The echo delay in Observation A at 1.4 GHz is $48 \mu\text{s}$; for a purely dispersive delay, the echo delay at 4.8 GHz on the same day should be $4.1 \mu\text{s}$. For Observation B, with a 1.4 GHz delay of $92 \mu\text{s}$, the echo delay at 4.8 GHz should be $9 \mu\text{s}$. The time resolution of our data (ultimately 10 ns) is more than adequate to resolve delays this short, but we do not see them.

It is worth noting that if the dispersion measure of the primary and echo microbursts differ, the dedispersion process will not have properly removed the dispersion from both microbursts. However, since the effect of dispersion is greater at lower frequencies, if some dispersive effect remained after dedispersion, the effect should be less prominent at higher frequencies. Since both

the primary and echo microbursts are visible at 1.4 GHz, dispersion should not impair our ability to see both microbursts at higher frequency, if indeed the emission of both microbursts actually extends to higher frequency.

The combined affect of a geometrically and dispersively delayed echo allows us to estimate a possible range for the echo delay at 4.8 GHz. The lower limit on the higher frequency echo delay would obtain in the limit of a purely dispersed echo. The upper limit on the higher frequency echo delay would obtain when the delay results from both geometric and dispersive effects. The possible range of the high frequency echo delay is then

$$1996 \text{ Oct } 14 : 4 \mu\text{s} < \Delta t_{\text{TOA}} < 52 \mu\text{s}$$

$$1997 \text{ Nov } 27 : 9 \mu\text{s} < \Delta t_{\text{TOA}} < 118 \mu\text{s}.$$

We have examined our higher frequency observations for emission within this time range, but no evidence of an echo microburst was found.

Frequency Dependent Refraction

If the refracting plasma model (§3.1) is correct, the absence of echo emission at 4.8 GHz places constraints on the electron number density within the plasma. If the refracting medium bends the pulsar beam by an angle θ , then the refraction event as a whole can be regarded as reflection, with equal incident and reflection angles, ϕ , and $\theta = \pi - 2\phi$ (see Figure 3.8). To obtain reflection within a region of plasma density enhancement the index of refraction (electron number density) must decrease (increase) toward the inner region of the plasma to a critical value, n_{rc} , such that the ray is refracted until it is parallel to the plasma boundary through which it entered (Lorrain & Corson,

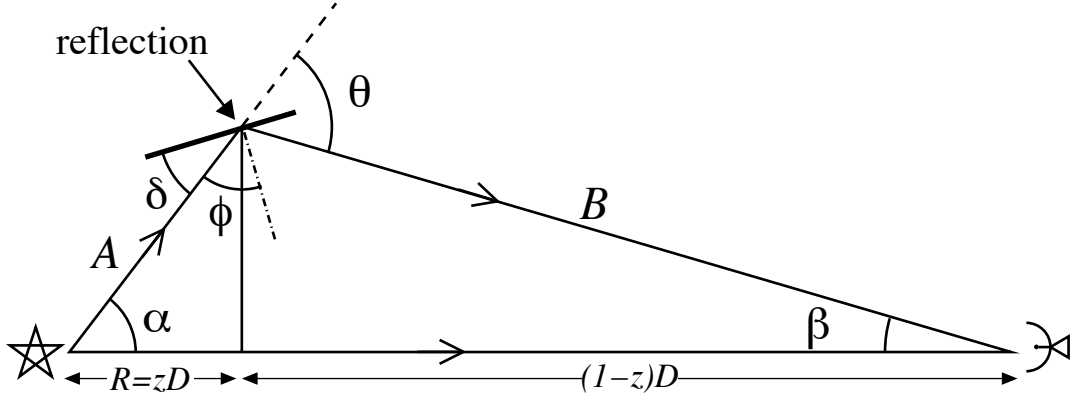


Figure 3.8: Diagram of the direct and reflected ray paths from the pulsar to telescope. The thick line shows the tangent to the surface of reflection, and the dash-dot line shows the normal to the tangent surface. The open arrowheads show the direction of ray propagation. Figure not to scale.

1970). In this case Snell's law of refraction can be written $n_{rc} = n_{ri} \sin \phi$, where n_{ri} is the index of refraction outside the plasma structure. By substituting in the expression for the index of refraction of a cold plasma, we obtain

$$N_e = (1 - n_{ri} \sin \phi) \frac{2\pi m \nu^2}{e^2},$$

where N_e is the electron number density, m and e the electron mass and charge, and ν the frequency of the pulsar emission.

Thus the critical electron density for pulse reflection is frequency dependent and is larger for higher frequencies. It is possible that the maximum density encountered by the reflected pulse during the times of our observations on 1996 October 14 and 1997 November 27 was between the critical values, $N_e(\nu = 1.4 \text{ GHz}) \leq N_e \leq N_e(\nu = 4.8 \text{ GHz})$, thus explaining the absence of an echo at 4.8 GHz.

We now consider the geometry of the reflection process in order to

gain insight into the characteristics of the reflecting plasma. Here we assume the echoes of Observations A and B were produced by small-angle reflection from cold plasma close to the pulsar and that the echo delay is a purely geometric effect, rather than a dispersive effect. We assume that the average index of refraction per unit length from the pulsar to Earth along both the direct and reflected paths is close to unity. We model the observed echo frequency dependence by supposing the intensity of the echo is determined by the ratio of the reflected to incident intensity at the boundary of the plasma structure.

Figure 3.8 is a cartoon of the ray paths considered in our model. If the angle of incidence, ϕ , of the pulsar radiation upon the plasma structure is $\phi \geq \phi_c$, where ϕ_c is the critical angle, then the incident radiation is reflected completely. For $\phi < \phi_c$, the incident radiation is only partially reflected. At the critical angle, Snell's law becomes

$$\sin \phi_c = \frac{n_{rt}}{n_{ri}} = \cos \delta_c,$$

where n_{rt} is the index of refraction of the the plasma (transmission) medium, n_{ri} is the index of refraction of the surrounding (incident) medium, and $\delta_c \equiv \pi/2 - \phi_c$. We define $\eta \equiv e^2 N_e / (2\pi m \nu^2)$, and the plasma index of refraction is $n_r \approx 1 - \eta$. For $\delta_c \ll 1$ and $\eta_i \ll 1$,

$$\frac{1}{2} \delta_c^2 \approx \eta_t - \eta_i. \quad (3.6)$$

Since we know the echo delay, we also know the difference in the length of the direct and reflected paths, S . If we then assume that $\alpha \ll 1$, $\beta \ll 1$, $z \ll 1$, (angles and lengths are defined in Figure 3.8) and use the small

angle relations, $\alpha/\beta \approx B/A \approx (1-z)/z$, S can be written as

$$S = A + B - D \approx \frac{1}{2}R\theta^2, \quad (3.7)$$

where $\theta = \alpha + \beta \approx \alpha/(1-z)$. Since we are considering reflection, $\theta = 2\delta$, and equation (3.6) can be rewritten as

$$4\delta_c^2 = \theta_c^2 \approx 8(\eta_t - \eta_i). \quad (3.8)$$

Total reflection occurs when $\delta \leq \delta_c$. By employing equation (3.7), (3.8), and the definition of η , this inequality can be written as

$$\frac{2S\pi m\nu^2}{4e^2} \leq R\Delta N_e, \quad (3.9)$$

where ΔN_e is the change in the electron number density at the boundary of the reflecting plasma. Partial reflection occurs when equation (3.9) is not true. Thus, if echoes are visible only in the limit of total reflection, then for Observation A, where echoes are seen at 1.4 GHz but not 4.8 GHz, equation (3.9) results in a range for the product $R\Delta N_e$:

$$10^{16} \text{ cm}^{-2} \leq R\Delta N_e \leq 10^{17} \text{ cm}^{-2}. \quad (3.10)$$

These two parameter values are determined by Backer et al. (2000) to be $R_{\text{fil}} \sim 1 \text{ pc}$ and $\Delta n_{\text{e fil}} \sim 1500 \text{ cm}^{-3}$ for the ejecta filaments in the outer nebula (assuming the region between the filaments has much lower electron density). However, the product of these values is 4 orders of magnitude above the range allowed by inequality (3.10). We believe that we may be observing refraction from a different type of ionized structure than was active in the echo observations of Backer et al. (2000) and Lyne et al. (2001).

3.5.5 Crab Nebular Wisps as a Location for Reflection

We note that the central wisp region of the Crab nebula, studied by Bietenholz et al. (2004), Hester et al. (2002), Mori et al. (2002), and Hester et al. (1995), provides plasma structures with a smaller pulsar-plasma distance, $0.01 \text{ pc} \lesssim R \lesssim 0.3 \text{ pc}$ (Bietenholz et al., 2004; Hester et al., 1995). To obtain the lowest allowable electron number density we use $R \sim 0.3 \text{ pc}$, which reduces equation (3.10) to

$$10^{-2} \text{ cm}^{-3} \leq \Delta N_e \leq 10^{-1} \text{ cm}^{-3}. \quad (3.11)$$

The wisp region is also more rapidly variable than the outer-nebula filaments. The wisps have been measured to have width $0.1'' < w < 0.4''$ (Hester et al., 1995) and projected speed $\sim 0.3c$ (Bietenholz et al., 2004). This combines to give us a line-of-sight (or small pulsar beam) crossing time of

$$4 \text{ days} < t_{\text{cross}} < 14 \text{ days}.$$

which is close to what we measured for the lifetime of the 1996 October event (≤ 4 days). To determine better the plausibility of refraction from the wisps we turn now to an estimation of the electron number density within the wisps via analysis of synchrotron emission.

We begin by assuming that the electron distribution in energy has a power law form, $n(\gamma) = n_0 \gamma^{-p}$, and that this distribution is the same in both the larger nebula and the wisps. Our goal is to determine the total electron density

$$N_e = \int_{\gamma_1}^{\gamma_2} n(\gamma) d\gamma$$

using the appropriate range of $\gamma_1 < \gamma < \gamma_2$ for the particles in the wisps.

The Crab nebula has been observed to have a power law emissivity, $\epsilon(\nu) \propto \nu^{-\alpha}$, with $\alpha \sim 0.3$ between 10^7 and 10^{13} Hz; the spectral index steepens within infrared and optical wavelengths to $\alpha \sim 0.8$ (Atoyan, 1999), and at higher frequencies the index increases further still. The spectral index relates to the distribution index according to $\alpha = (p-1)/2$. Here we ignore the highest energy part of the distribution because the contribution to the total electron density from this energy range is much smaller than that from the lower energy part of the distribution.

The synchrotron emissivity is a function of n_0 and the magnetic field B ,

$$\epsilon(\nu) \propto n_0 B^{1+\alpha} \nu^{-\alpha}. \quad (3.12)$$

Therefore, to determine n_0 we need to know $\epsilon(\nu)$ and B ; in general it is not possible to determine these quantities independently. It is conventional to resolve this degeneracy by assuming equipartition of energy between the particles and the magnetic field,

$$\int_{\gamma_{\min}}^{\gamma_{\max}} \gamma mc^2 n(\gamma) d\gamma = \frac{B^2}{8\pi}, \quad (3.13)$$

where γmc^2 is the particle energy. This assumption makes our problem one of solving for two unknowns, n_0 and B , in equations (3.12) and (3.13). We do this by utilizing the emissivity measured by Hester et al. (1995) for the wisp structure they label as “knot 1”, which is the smallest and densest structure they observe.

We first employ a two-part power law electron distribution function, where the break in the functional form occurs at the energy, $\gamma_c = 10^4$, corre-

sponding to the break in the spectrum.

$$n(\gamma) = \begin{cases} n_0\gamma^{-1.6} & , \quad \gamma_1 < \gamma < \gamma_c \\ n_1\gamma^{-2.6} & , \quad \gamma_c < \gamma < \gamma_2 \end{cases},$$

where $n_1 = n_0\gamma_c$. The emissivity of the higher-energy part of the distribution was measured by Hester et al. (1995); we include the lower-energy part of the distribution to account for the observed radio emission. We follow Hester et al. (1995) and set $\gamma_2 = 10^9$. The high Lorentz factors dominate the energy density, and equipartition of energy using $\epsilon(\nu) = 1.23 \times 10^{-31} \text{ ergs cm}^{-3} \text{ s}^{-1} \text{ Hz}^{-1}$ (Hester et al., 1995) gives us $B \sim 3.8 \text{ mG}$ and $n_1 \sim 42 \text{ cm}^{-3}$. From this we choose $\gamma_1 = 25$ so that the synchrotron spectrum will extend down to 10 MHz, as observed for the nebula. We find a total electron number density $N_e \sim 1.0 \times 10^{-3} \text{ cm}^{-3}$.

Alternatively, if we assume the wisp electron distribution has an unbroken power law form

$$n(\gamma) = n_0\gamma^{-2.1} \quad , \quad \gamma_1 < \gamma < \gamma_2,$$

the number of low energy electrons increases relative to the broken power law above. Again with $\gamma_2 = 10^9$, equipartition of energy using knot 1 emissivity gives $B \sim 3.9 \text{ mG}$ and $n_0 \sim 7.9 \times 10^{-2} \text{ cm}^{-3}$. We choose $\gamma_1 = 25$ in order to obtain 10-MHz radiation. This gives us a total electron number density of $N_e \sim 5.5 \times 10^{-3} \text{ cm}^{-3}$.

Using two different power law electron density distributions, we have found that the total electron density is less than that predicted by equation (3.11). We make three points concerning this discrepancy. First, the six wisp emissivities reported by Hester et al. (1995) span an order of magnitude. We

think it is likely that higher pressure features, dense enough to produce the echoes we have observed, exist either transiently or on scales smaller than those observed in the optical wavelength range. Second, we have assumed that the wisps have a low-frequency emissivity and magnetic field similar to the mean nebula. It is possible that the magnetic field may be weaker, or the low-frequency emissivity stronger than we have assumed. This would increase the total electron density found through equipartition. Third, equipartition is an assumption. If the electron energies and the magnetic field energies differed by a few-to-ten in pressure, the total electron density would increase sufficiently to satisfy our reflection model.

3.6 Conclusions

We have observed echo emission in Crab pulsar giant pulses at 1.4 GHz on 1996 October 14 and 1997 November 26. The echo emission is strongly frequency dependent; the echo is absent in simultaneously observed giant pulses at 4.8 GHz. The echo lag time, $\geq 40 \mu\text{s}$, is the shortest yet observed for Crab echoes. The 1996 October echo event has the shortest lifetime, ≤ 4 days, of any echo event observed.

We find for both the 1996 October and 1997 November echo events: the echo microburst maximum flux is a factor of 10 less than the primary microburst maximum flux; the echo total energy is less than the primary total energy by a factor of a few; the ratio of the widths of the echo microbursts to the widths of the primary microbursts is ~ 3.5 .

The echo power and energy are both lower than that of the corre-

sponding primary microburst. This may be attributed to pulse reflection from the curved surface of a plasma structure in the nebula. For a spherical surface, the radius of curvature needs to be a few times the distance from the pulsar to the plasma structure. We have also found that the echoes are broader than the primary microbursts; this is likely a result of additional scattering along the echo ray path.

We believe that the echoes we have observed may have been produced by refraction from plasma structure in the inner nebula wisp region. The frequency dependence and echo delay times we observed suggest refraction close to the star; the 1996 October event lifetime suggests plasma structure variability such as that present in the outward-moving wisps; synchrotron emissivity analysis shows that the wisps may have the electron densities, either transiently or on small angular scales, necessary to generate pulse reflection at 1.4 GHz.

We thank David Moffett and Tracey DeLaney for their assistance with VLA observations. We also thank Christine Jordan of Jodrell Bank Observatory for the data she provided us on Crab echoes observed at Jodrell Bank. We thank Paul Arendt and the Socorro pulsar group for helpful discussions. This work was partially supported by NSF grant AST-0139641.

CHAPTER 4

DISPERSION MEASURE DETERMINATION

4.1 Introduction

Dispersion has been evident in pulsar observations since the discovery of the first pulsar (Hewish et al., 1968), in which dispersion was manifested by later pulse arrival times at lower frequencies. Dispersion variability of the Crab pulsar was evident as early as 1971 (Rankin & Roberts, 1971), where the dispersion was observed to vary on time scales from several days to one year. More recent dispersion measurements by Backer (2002) suggest¹ variability may exist on time scales as short as tens of minutes.

For typical pulsars, the only method of measuring pulse dispersion is a comparison of average pulse profiles at different frequencies. The difference in the arrival time at each frequency allows for a direct measurement of cold plasma dispersion in the form of the dispersion measure, which is defined as the path integral of the electron number density,

$$\text{DM} \equiv \int_0^L N_e dr. \quad (4.1)$$

L is the distance from Earth to the pulsar. Dispersion measure is introduced in § 1.3.1.

¹No error bars are available in Backer's data; see § 4.4.2.

Dispersion is interesting for several reasons. First, investigation of the pulsar emission mechanism *via* high-time-resolution pulsar observations relies upon an understanding of pulse dispersion. For such observations, it is desirable to remove the dispersion incurred by passage through ionized material between the emitter and receiver and study the pulse as it was at the place of emission. Effectively accomplishing dispersion removal and judging the quality of the dedispersed pulse requires an understanding of the behavior of dispersion and dispersion variability.

Second, if any dispersion occurs within the pulsar magnetosphere (the emission region), identifying and analyzing it may give further insight into the physics of the emission region and emission mechanism. Single pulse observations of the Crab main pulse and interpulse allow for comparison of the dispersive properties of different parts of the magnetosphere.

Third, since dispersion variability is a direct indication of plasma density fluctuations, and an indirect indication of plasma turbulence scales (Phillips & Wolszczan, 1991; Armstrong et al., 1995) along the line of sight to the pulsar, it is of interest to know how quickly and with what amplitude pulse dispersion varies. Backer et al. (2000) found Crab pulsar dispersion to vary significantly over ≤ 7 days. The nebular refraction discussed in Chapter 3 suggests variations may exist over periods of several days or less.

This chapter reports dispersion measurements obtained from high-time-resolution Crab giant pulses. Dispersion in a giant pulse is measured just as dispersion is measured in an average profile: the time of arrival difference between flux maxima in different frequency bands is measured and converted

directly to DM. Dispersion variability can then be determined with a time resolution set by the interval between recorded giant pulses. I have measured fluctuations in DM with unprecedented time resolution, as small as several minutes.

Both giant main pulses and giant interpulses have been used to measure dispersion. I show in this chapter that there are differences between main pulse and interpulse dispersion, and these differences are likely caused by propagation through the magnetized plasma in the pulsar magnetosphere. I compare the data with two magnetospheric dispersion laws put forth in the literature.

The observations used in this chapter are discussed in § 4.2. I present the method of measuring giant pulse dispersion in § 4.3. The results of my measurements are discussed in § 4.4. Then, in § 4.5 I further discuss of my results by focusing on interpulse dispersion and its connection to the magnetosphere. I summarize my findings in § 4.6.

4.2 Observations

The ultra high time resolution (UHTR) observing system (Kern, 2004; Moffett, 1997) was used to record high-time-resolution Crab giant pulses. (See § 1.5 for a description of the UHTR system.) The dispersion investigation in this chapter makes use of 11 years of Crab single giant pulse observations. Each observing session is listed in Table 4.1. Pulses observed between years 1996 and 1999 (MJD 50368 and 51218) were recorded with the Very Large

Array² (VLA); pulses observed between years 2002 and 2007 (MJD 52414 and 54123) were recorded with the Arecibo Observatory radio telescope³.

Table 4.1: DM measurements listed by observing session.

MJD	Center		BW (GHz)	MP ⟨DM⟩ (pc cm ⁻³)	# MP's	IP ⟨DM⟩ (pc cm ⁻³)	# IP's
	freq (GHz)						
	ν_1	ν_2					
50368	4.8851	1.4351	0.050	n/a	0	56.8208 ± 0.0001	3
50368	4.8851	1.4351	0.050	56.8226 ± 0.0037	28	n/a	0
50370	4.8851	1.4351	0.050	56.8276 ± 0.0030	53	n/a	0
50372	4.8851	1.4351	0.050	56.8325 ± 0.0004	3	n/a	0
50372	4.6351	1.4351	0.050	56.8324 ± 0.0002	5	n/a	0
50778	4.9351	4.8851	0.050	56.9187 ± 0.0708	3	n/a	0
51159	1.6649	1.3851	0.050	56.8000 ± 0.0010	22	n/a	0
51167	4.9851	4.5351	0.050	56.8009 ± 0.0036	35	n/a	0
51167	4.9851	4.6851	0.050	56.7995 ± 0.0037	11	n/a	0
51174	8.5351	8.4351	0.050	n/a	0	$56.5603 \pm 0.3089^\dagger$	12
51174	4.7351	4.6851	0.050	56.7844 ± 0.0185	4	n/a	0
51174	1.7149	1.3851	0.050	56.7968 ± 0.0005	49	n/a	0
51174	1.7149	1.4351	0.050	56.7967 ± 0.0003	34	n/a	0
51217	4.8351	4.7351	0.050	56.7942 ± 0.0138	19	n/a	0
51217	4.8351	4.6351	0.050	56.7931 ± 0.0093	6	n/a	0
51218	4.8351	4.7351	0.050	56.8057 ± 0.0189	4	n/a	0
51218	4.8351	4.6351	0.050	56.7970 ± 0.0094	3	n/a	0
51218	1.7141	1.2401	0.025	56.7948 ± 0.0007	36	n/a	0
52414	5.7500	5.2500	0.500	56.7686 ± 0.0034	5	n/a	0
52414	8.9000	8.4000	0.500	56.7655 ± 0.0082	9	n/a	0

continued on next page

[†]This DM value is suspect due to its large uncertainty, narrow passband width, and narrow frequency separation. See §4.4 for further discussion.

²The Very Large Array is an instrument of the National Radio Astronomy Observatory, a facility of the National Science Foundation operated under cooperative agreement by Associated Universities, Inc.

³The Arecibo Observatory is part of the National Astronomy and Ionosphere Center, which is operated by Cornell University under a cooperative agreement with the National Science Foundation.

Table 4.1: DM measurements listed by observing session

MJD	Center		BW (GHz)	MP \langle DM \rangle (pc cm $^{-3}$)	# MP's	IP \langle DM \rangle (pc cm $^{-3}$)	# IP's
	freq (GHz)						
	ν_1	ν_2					
52417	5.2500	4.7500	0.500	56.7671 ± 0.0011	5	n/a	0
53156	9.8750	8.6250	1.250	n/a	0	56.7626 ± 0.0106	12
53162	7.9250	6.6750	1.250	n/a	0	56.8012	1
53372	9.8750	8.6250	1.250	56.7411 ± 0.0045	2	56.7567 ± 0.0030	4
53375	9.8750	8.6250	1.250	56.7354	1	56.7481 ± 0.0105	6
53375	9.8750	8.6250	1.250	56.7353 ± 0.0009	4	56.7459	1
53378	4.8563	5.1688	0.313	56.7344 ± 0.0021	30	56.7393 ± 0.0031	3
53582	6.3125	6.9375	0.625	56.7385 ± 0.0024	5	n/a	0
53582	9.8750	8.6250	1.250	56.7383 ± 0.0007	3	56.7548	1
53584	6.1875	6.8125	0.625	56.7388 ± 0.0012	34	56.7485 ± 0.0112	20
53584	6.1875	6.8125	0.625	56.7389 ± 0.0026	16	56.7417 ± 0.0007	2
53586	4.1875	4.8125	0.625	56.7397 ± 0.0011	11	n/a	0
53586	7.9250	6.6750	1.250	56.7387 ± 0.0004	7	n/a	0
53590	4.1875	4.8125	0.625	56.7387 ± 0.0004	11	n/a	0
53590	9.8750	8.6250	1.250	56.7401 ± 0.0022	10	56.7517	1
53591	8.0250	6.7750	1.250	56.7387 ± 0.0002	5	56.7566 ± 0.0040	3
53591	9.8750	8.6250	1.250	56.7389 ± 0.0000	2	56.7603 ± 0.0213	23
53803	9.8750	8.6250	1.250	n/a	0	56.7523 ± 0.0077	6
53804	9.8750	8.6250	1.250	56.7426 ± 0.0079	8	56.7528 ± 0.0041	5
53805	7.3125	6.6875	0.625	56.7407 ± 0.0021	10	56.7582 ± 0.0149	17
53807	4.3438	4.6563	0.313	56.7431 ± 0.0018	3	n/a	0
53807	9.8750	8.6250	1.250	56.7410	1	56.7490 ± 0.0098	3
53807	9.8750	8.6250	1.250	56.7446 ± 0.0081	8	56.7663 ± 0.0162	3
53808	6.1875	6.8125	0.625	56.7430 ± 0.0070	5	56.7485 ± 0.0117	6
53808	9.8750	8.6250	1.250	56.7427 ± 0.0045	3	56.7526 ± 0.0077	4
54007	4.6563	4.3438	0.313	56.7610 ± 0.0009	3	n/a	0
54101	9.8750	8.6250	1.250	56.7646 ± 0.0102	11	56.7697 ± 0.0110	3
54101	9.8750	8.6250	1.250	56.7591 ± 0.0009	5	n/a	0
54123	9.8750	8.6250	1.250	56.7610 ± 0.0009	3	56.7715 ± 0.0076	8

VLA observations were recorded in phased-array mode. The array of antennas was divided into two subarrays. One subarray operated at a low

observing frequency and the other array at a higher frequency. Both subarray passbands were 50 MHz wide. See §1.5 for more detail on two-frequency observations with the VLA.

Arecibo observations were made with passband widths $0.313 \text{ GHz} \leq \Delta\nu \leq 2.5 \text{ GHz}$. The dispersion measurement method (discussed in § 4.3) requires a pulse to be observed at two different passbands. I therefore split the bandwidth of each pulse recorded at Arecibo to obtain two records with adjacent passbands, each with half the original pulse bandwidth.

In Arecibo observations, the UHTR system often monitored multiple disjoint ranges of Crab pulsar phase, namely the main pulse and interpulse, and captured giant pulses that occurred within those phase windows. I use the pulse dynamic spectra to distinguish conveniently between main pulses and inter-pulses. At the observing frequencies recorded at Arecibo ($4 < \nu < 10 \text{ GHz}$), there is a consistent difference between the dynamic spectra of main pulses and inter-pulses, as demonstrated in Figure 4.1 (Hankins & Eilek, 2007). Main pulses tend to be more narrow in time than inter-pulses and have spectra that are typically uniform across the observing bandwidth. Inter-pulses are broader in time and exhibit regularly spaced spectral bands that may increase in frequency with time. Multiple trigger windows were not used in VLA observations, and thus each observing session captured either main or inter-pulses exclusively.

The main pulse and interpulse displayed in Figure 4.1 were both recorded at Arecibo Observatory on MJD 53808 with 9.25-GHz center frequency and 2.5-GHz bandwidth; the interpulse was recorded 12 minutes after the main pulse. The main pulse (interpulse) total intensity time resolution is

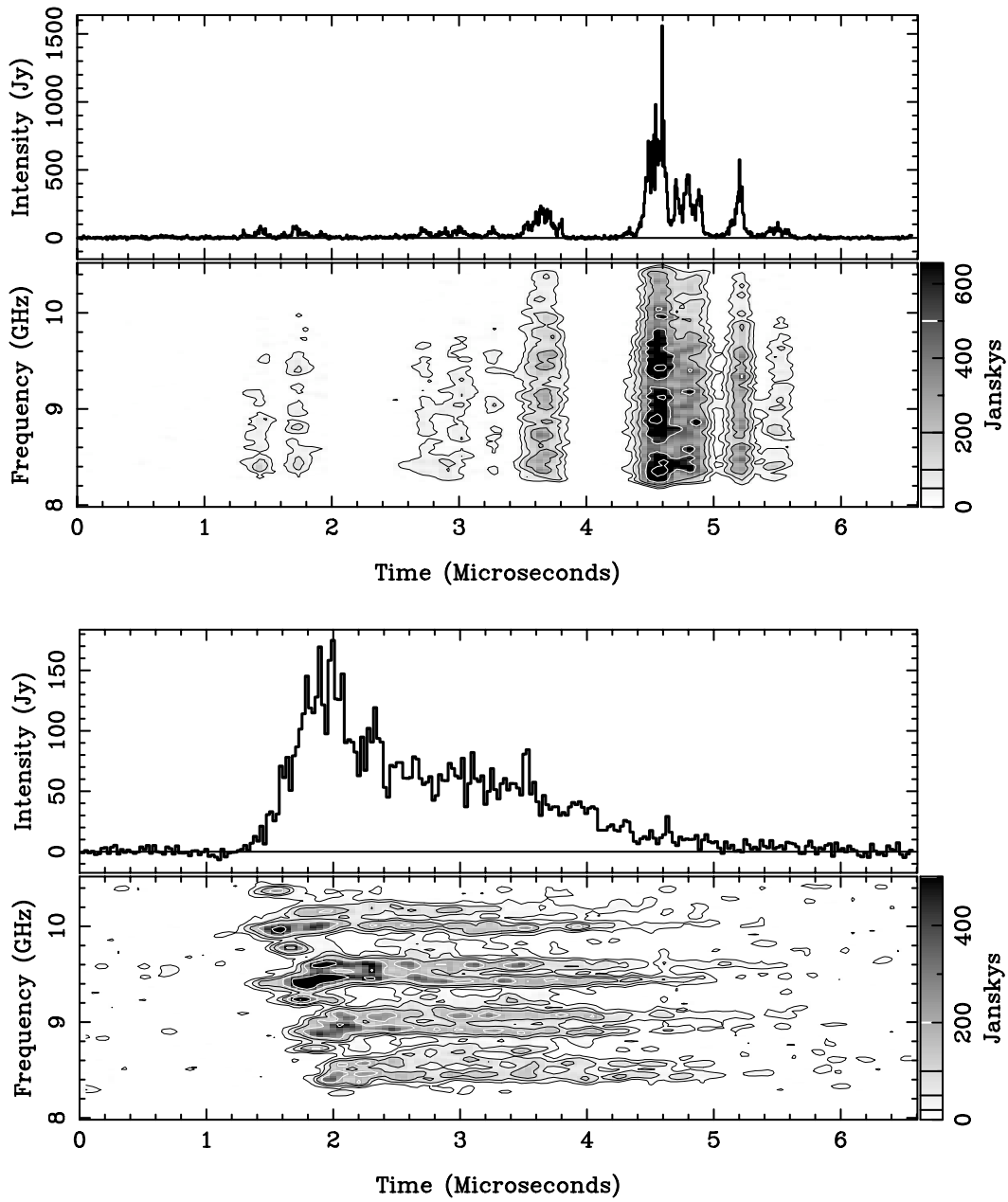


Figure 4.1: Dedispersed total intensity and dynamic spectra from one main pulse (top) and one interpulse (bottom). See § 4.2 for details. Figure taken from Hankins & Eilek (2007).

6.4 ns (51.2 ns); both main and interpulse dynamic spectra have time resolution of 51.2 ns and frequency resolution of 19.5 MHz.

4.3 Dispersion Measurement Method

The propagation time of a pulse in an isotropic, non-relativistic plasma relates to DM and frequency as shown here [and in Equation (1.8)],

$$t_p(\nu) = t_0 + \frac{q^2}{2\pi cm\nu^2} \text{DM}, \quad (4.2)$$

where t_0 is the propagation time in vacuum, and DM has *fundamental* units of cm^{-2} . The difference in the propagation time at two frequencies, $\Delta t_p = t_{p2} - t_{p1}$, then relates to DM by (Manchester & Taylor, 1972),

$$\text{DM} = 2.41 \times 10^{-16} \left(\frac{1}{\nu_2^2} - \frac{1}{\nu_1^2} \right)^{-1} \Delta t_p. \quad (4.3)$$

Here, DM has the *conventional* units of $\text{pc} \cdot \text{cm}^{-3}$, ν has units of Hertz, and Δt_p has units of seconds. Equation (4.3) shows that dispersion measure is directly proportional to the pulse time of arrival difference between two frequencies.

To measure the DM of individual giant pulses I use the following process. A set of pulses is dedispersed with assumed dispersion measure, $\widetilde{\text{DM}}$, initially obtained from an interpolation of monthly average profile Crab pulsar DM measurements made at the Jodrell Bank Observatory⁴. If the true dispersion measure, DM, is not equal to $\widetilde{\text{DM}}$, the pulse will then have a residual dispersion,

$$\text{DM}_{\text{res}} = \text{DM} - \widetilde{\text{DM}} = 2.41 \times 10^{-16} \left(\frac{1}{\nu_2^2} - \frac{1}{\nu_1^2} \right)^{-1} \Delta t_{\text{res}}, \quad (4.4)$$

⁴The Jodrell Bank Crab pulsar ephemeris, containing a monthly DM measurement, is available online at <http://www.jb.man.ac.uk/~pulsar/crab.html>.

where $\Delta t_{\text{res}} = \Delta t_{\text{p}} - \widetilde{\Delta t}_{\text{p}}$. Here, Δt_{p} is the true time-of-arrival (TOA) difference between the two observing frequencies, and $\widetilde{\Delta t}_{\text{p}}$ is the TOA difference predicted by the dedispersion value, $\widetilde{\text{DM}}$. I measure Δt_{res} by cross-correlating the dedispersed high and low frequency pulse profile (see immediately below) and then obtain DM_{res} ; finally, I get $\text{DM} = \widetilde{\text{DM}} + \text{DM}_{\text{res}}$. To obtain the most accurate DM measurement, I may choose to iterate, by setting $\widetilde{\text{DM}}$ to derived DM, dedispersing the original set of pulses again with the more accurate $\widetilde{\text{DM}}$, and obtaining a new value of DM. Since I find that the main and interpulse DM's often differ substantially (see § 4.4), I segregate these pulses when necessary and dedisperse them separately to find the most accurate value of DM for each group.

I use the following process to measure Δt_{res} from the cross-correlation function (CCF) of the dedispersed high and low frequency pulse profiles.

1. A window of predetermined width is centered on the flux maximum of the high frequency pulse time series so it contains the on-pulse region.
2. The $\widetilde{\text{DM}}$ used in pulse dedispersion determines the expected time of arrival of the low frequency pulse relative to the high frequency flux maximum. A window is then centered on this time in the low frequency pulse record.
3. The CCF is computed from the data in the high and low frequency windows.
4. A parabola is fit to the peak of the CCF. The time offset of the maximum of the parabola from zero-lag is set equal to Δt_{res} . The uncertainty in the

time of the parabola maximum is equal to the uncertainty in Δt_{res} .

The measurement of Δt_{res} then gives Δt_{p} , and Δt_{p} gives DM. The uncertainty in Δt_{res} translates to an uncertainty in DM. The arithmetic mean of the individual-pulse dispersion measures, $\langle \text{DM} \rangle$, is computed for each main pulse and interpulse group for each observing session. In anticipation of the discussion in § 4.5, where I explore alternative dispersion laws, all DM measurements should be regarded as *apparent* dispersion measure, since the measured DM is not necessarily a result only of propagation through an isotropic, cold plasma medium. If the pulses have been dispersed in any other medium, Equations (4.1) and (4.3) may not agree.

This method of DM measurement assumes that the high and low frequency parts of the pulse are emitted at the same time and in the same place. Thus, I find a value for DM that makes the flux maximum at each frequency within the observing bandwidth as nearly simultaneous as possible.

Use of this CCF method of DM determination requires there be sufficient power in both the high and low frequency pulses to produce a CCF that can be fitted with a parabola. A small fraction of the pulses I have observed do not have sufficient power in both observing bands to make such a CCF. I choose to exclude from this dispersion study pulses for which the maximum signal-to-noise-ratio⁵ (SNR) in either band is ≤ 2 .

⁵The maximum SNR is computed by subtracting the off-pulse mean power from the maximum on-pulse power and then dividing by the off-pulse standard deviation,

$$\text{SNR}_{\text{max}} = (F_{\text{max}} - \langle F_{\text{off-pulse}} \rangle) / \sigma_{\text{off-pulse}}.$$

4.4 Giant Pulse Dispersion Measurements

Table 4.1 lists apparent $\langle \text{DM} \rangle$ measurements for each two-frequency Crab giant pulse VLA observation and each wide bandwidth giant pulse Arecibo observation. The standard deviation among single-pulse DM measurements within each observing session is given as the uncertainty of $\langle \text{DM} \rangle$. The center frequencies of the two passbands are shown in Table 4.1 along with the bandwidth at each center frequency. The number of giant main pulses and giant interpulses used to compute $\langle \text{DM} \rangle$ in each observing session is also shown.

The VLA interpulse observation from MJD 51174 (see Table 4.1) has been excluded from the dispersion analysis that follows. This observation is the only 8 GHz (X-band) VLA interpulse observation. The DM values measured in this observation are exceptionally scattered, as indicated by the large $\langle \text{DM} \rangle$ uncertainty. I believe this enhanced scattering is a result of observing high frequency interpulses with narrow (50 MHz) bandwidth and narrow frequency separation between passbands, so that Δt_p is small; I do not believe that those measurements represent the true dispersion of the interpulse. Wider bandwidth observations of interpulses (for example, see the interpulse in Figure 4.1) reveal complex spectral structure that evolves with time. By observing with narrow bandwidth, only portions of the complex structure are recorded, and this may skew DM measurement. However, I choose to leave this observation in Table 4.1 to emphasize the unique characteristics of the interpulse and one of the challenges associated with making accurate DM measurements.

4.4.1 Single Pulse Measurements

Single-main-pulse and single-interpulse DM measurements recorded on MJD 53805 are plotted in Figures 4.2 and 4.3, respectively. The data points contained in these figures are single-pulse DM measurements. Figures 4.2 and 4.3 demonstrate four findings consistent throughout my data.

1. The uncertainty in single-pulse DM measurements is smaller than the DM scatter among single pulses separated in time by minutes to hours.
2. The interpulse DM scatter measured over time scales of minutes to hours is larger than the main pulse DM scatter. (To emphasize this point Figures 4.2 and 4.3 are plotted with the same vertical scale.)
3. DM does not depend upon pulsar rotational phase.
4. DM is not observed to vary systematically over times of minutes to hours.

4.4.2 Pulse-Averaged Measurements

Figure 4.4 is a plot of the $\langle \text{DM} \rangle$ measurements in Table 4.1, along with the monthly average profile DM measurements made at Jodrell Bank and average profile measurements made by Backer (2002) and described by Backer et al. (2000). While giant pulse $\langle \text{DM} \rangle$ measurements do not always agree to within uncertainties with the average profile DM values, both the giant pulse and average profile measurements follow the same long-time-scale trends. Six of the $\langle \text{DM} \rangle$ values in Figure 4.4 are derived from ensembles consisting of only one giant pulse; these data points are plotted without error bars. The high-DM data point at MJD 53162 is one such single-pulse measurement; its high value

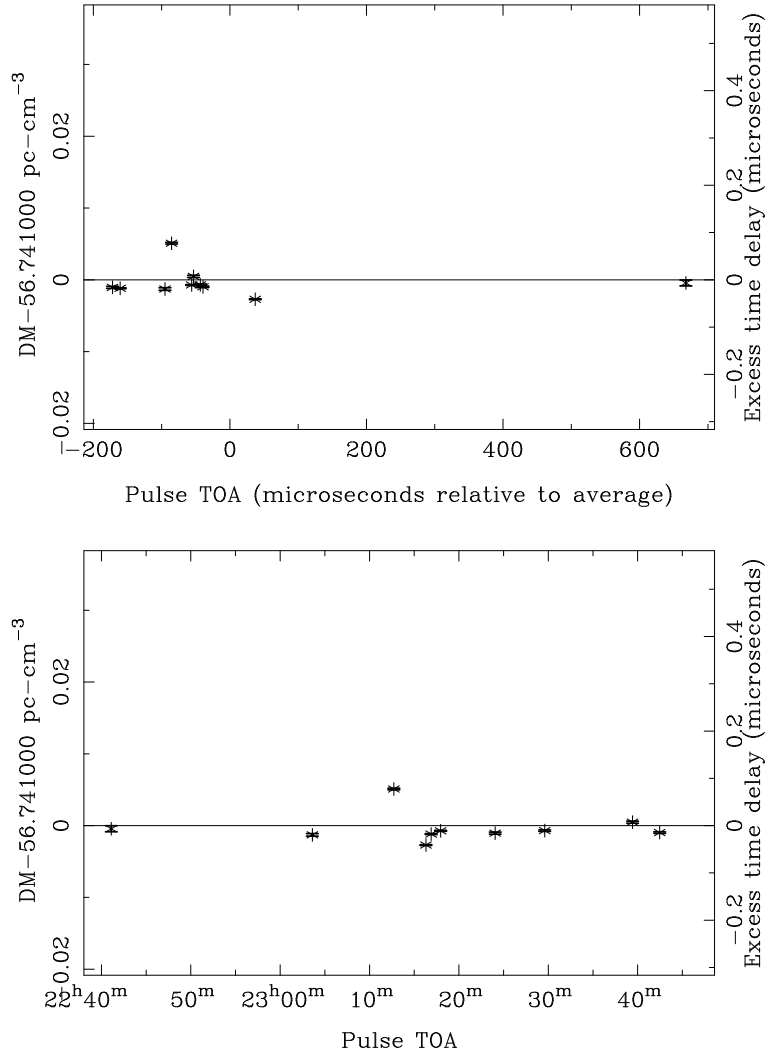


Figure 4.2: Single giant main pulse DM measurements observed on MJD 53805 and split into two passbands (see table 4.1). The main pulses shown here have been dedispersed with $\bar{DM} = 56.741 \text{ pc cm}^{-3}$. The left side vertical axis shows the residual, DM_{res} . The right side vertical axis shows the residual time of arrival difference, Δt_{res} , between the pulse in the high and low frequency passbands. The pulse time of arrival is measured at the pulse flux maximum. The top plot horizontal axis is the pulse time of arrival relative to the average time of arrival in each pulse record; this is equivalent to relative pulsar rotational phase. The bottom plot horizontal axis is the time of arrival of each pulse in Universal Time.

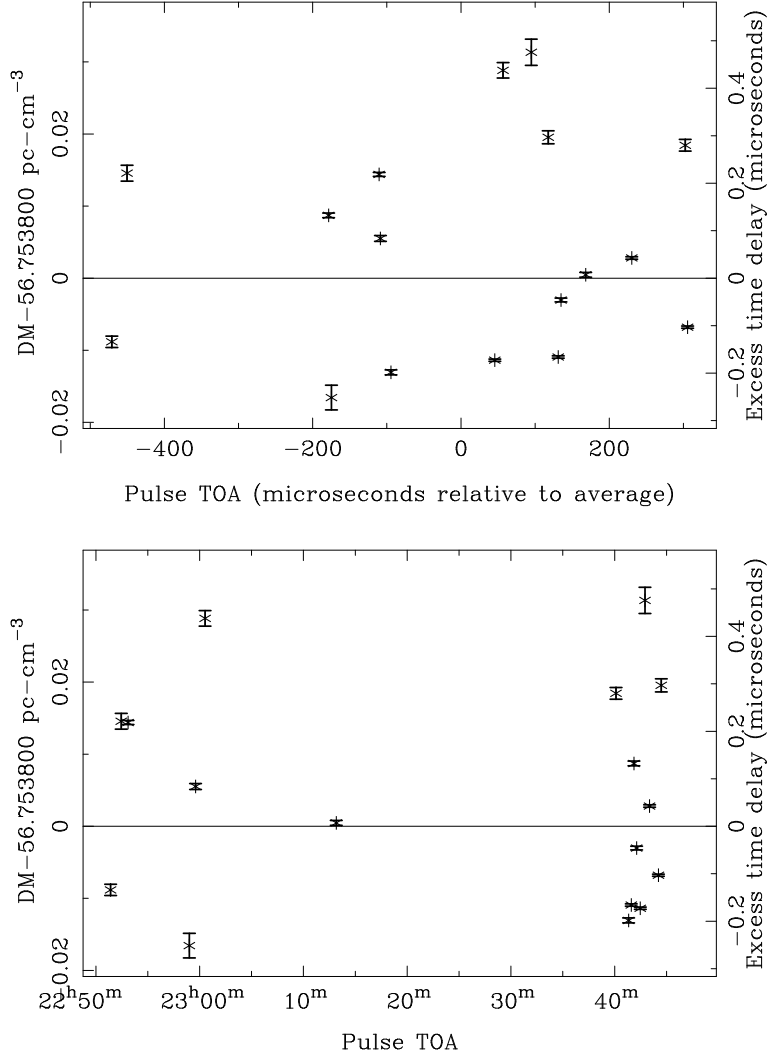


Figure 4.3: Single giant interpulse DM measurements observed on MJD 53805 and split into two passbands (see table 4.1). The interpulses shown here have been dedispersed with $\widehat{\text{DM}} = 56.741 \text{ pc cm}^{-3}$. The left side vertical axis shows the residual, DM_{res} . The right side vertical axis shows the residual time of arrival difference, Δt_{res} , between the pulse in the high and low frequency passbands. The pulse time of arrival is measured at the pulse flux maximum. The top plot horizontal axis is the pulse time of arrival relative to the average time of arrival in each pulse record; this is equivalent to relative pulsar rotational phase. The bottom plot horizontal axis is the time of arrival of each pulse in Universal Time.

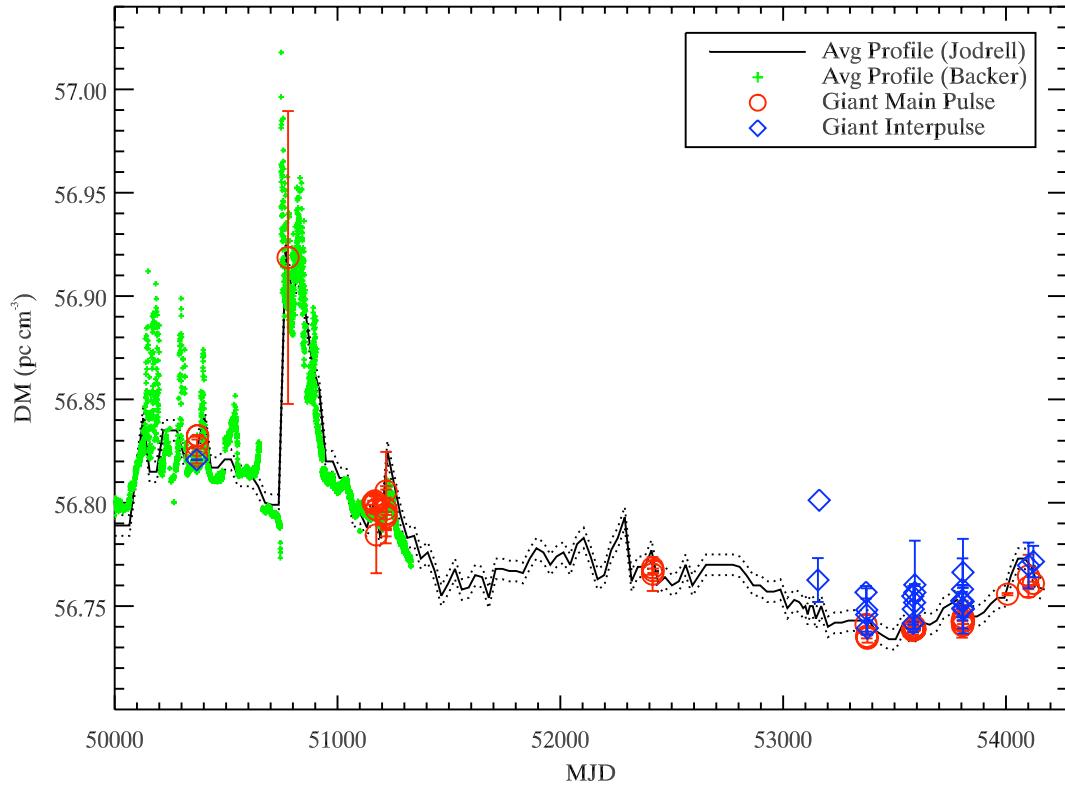


Figure 4.4: Dispersion measurements obtained from average profile observations made at Jodrell Bank, average profile observations made by Backer (2002), and giant pulse observations made at the VLA and Arecibo Observatory. The dotted lines denote the typical uncertainty in the Jodrell Bank monthly DM measurements. The DM measurements made by Backer (2002) are provided without uncertainties. The giant pulse $\langle \text{DM} \rangle$ values are averages over either the main pulses or interpulses recorded in each observing session; giant pulse $\langle \text{DM} \rangle$ uncertainties show the standard deviation of the single-pulse measurements. The six giant pulse observing sessions consisting of only one pulse are plotted without error bars. This figure shows that giant pulse DM measurements follow the same trends over long time scales as average profile measurements.

is indicative of the large variability in dispersion throughout all my interpulse measurements.

Figure 4.5 shows two plots of enlarged regions from Figure 4.4. The plots in Figure 4.5 show better the variability among the giant pulse, Jodrell Bank, and Backer (2002) measurements over days to tens of days; these plots also show the degree of correspondence between these three independent sets of measurements.

Figure 4.6 shows another enlarged region from Figure 4.4 (MJD 53100 to 54174). It is evident from this figure that the giant interpulse DM measurements are often higher and more scattered than giant main pulse DM measurements taken around the same time. This suggests that the interpulse may under go an additional, variable dispersion not encountered by the main pulse. I investigate this idea below, in §4.5. It is also apparent in Figure 4.6 that the average profile DM is in better agreement with $\langle \text{DM} \rangle$ measurements of giant main pulses than giant interpsules.

As mentioned in §4.1, average profile DM measurements have been used by other authors (Phillips & Wolszczan, 1991; Armstrong et al., 1995) to measure turbulence in the interstellar medium. Though it is beyond the scope of this work, single pulse DM measurements may be used to measure turbulence within the Crab pulsar magnetosphere and Crab nebula. However, differentiating the turbulent contribution of the magnetosphere from that of the ISM will likely require observations of other sources.

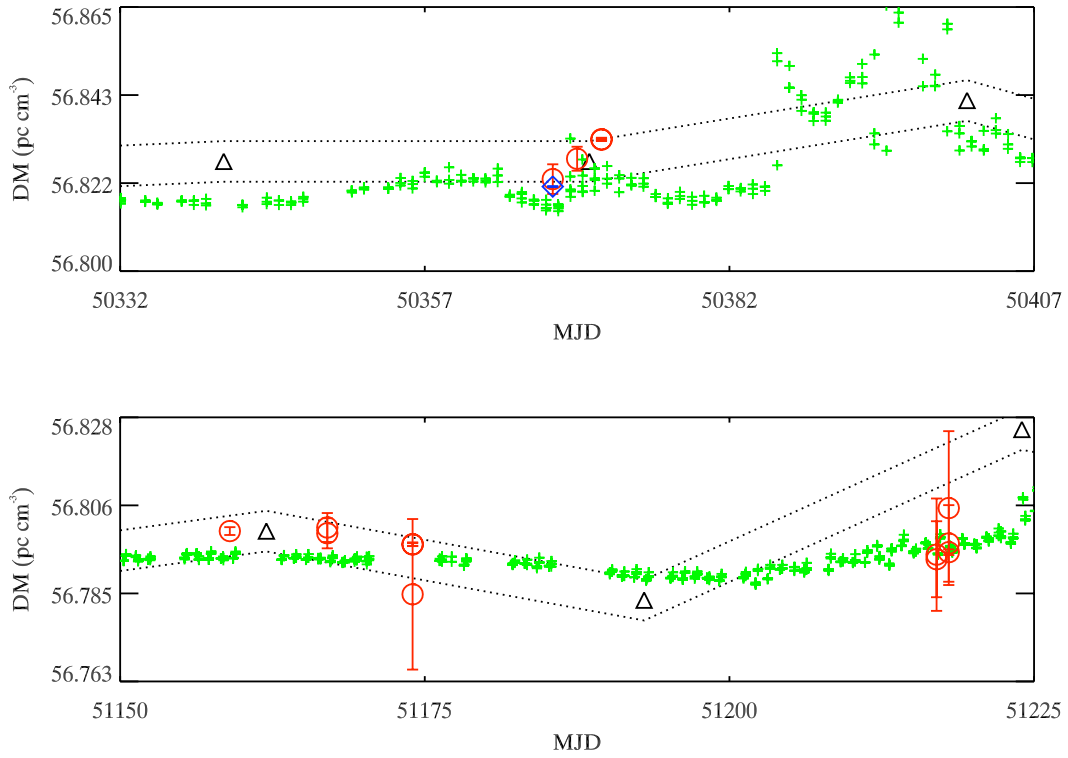


Figure 4.5: Enlargement of two groups of giant pulse $\langle \text{DM} \rangle$ measurements from Figure 4.4. The vertical and horizontal scales are the same in both plots here. The plot symbols, lines styles, and color codes are identical to those in Figure 4.4, with the exception that the Jodrell Bank DM measurements are now plotted with triangles rather than a solid line; dotted lines again represent the interpolated Jodrell Bank DM uncertainty. These plots show giant pulse and average profile DM fluctuations on time scales of days to tens of days.

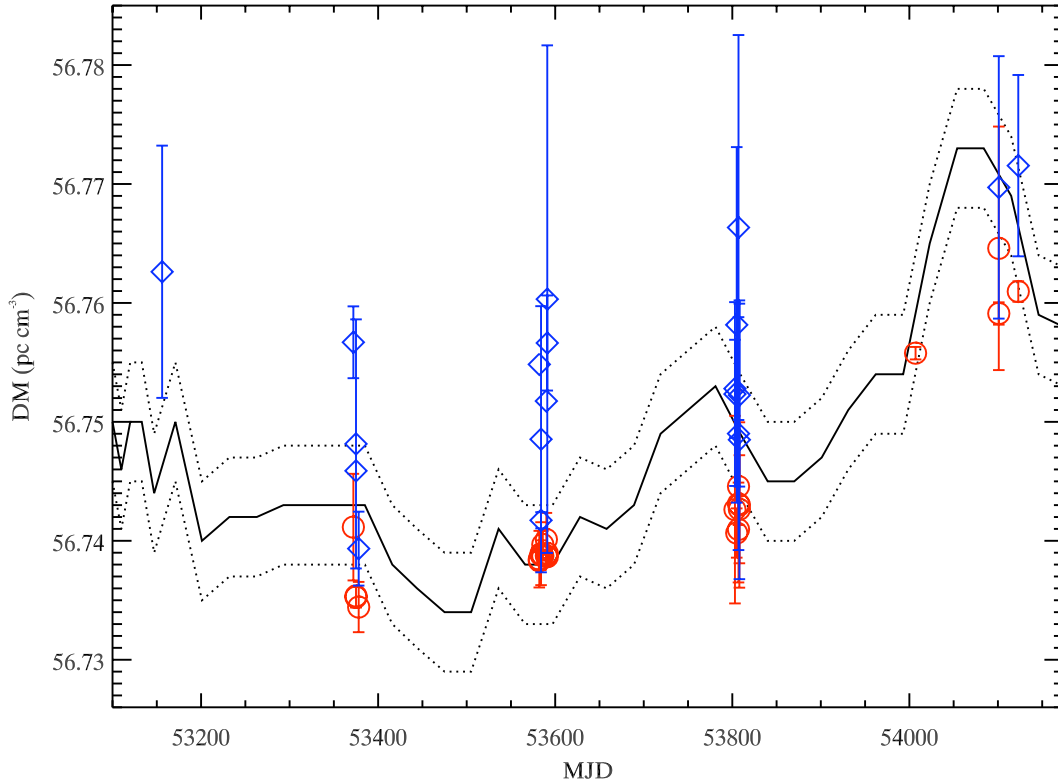


Figure 4.6: Enlargement of one group of giant pulse $\langle \text{DM} \rangle$ measurements. The plot symbols, lines styles, and color codes are identical to those in Figure 4.4. This enlarged region of DM-versus-MJD space demonstrates several important points: the difference between the often higher-DM interpulse and the lower-DM main pulse; the large scatter in interpulse DM measurements, in contrast to the more consistent main pulse DM measurements; the size of average profile and giant pulse $\langle \text{DM} \rangle$ uncertainties; the degree of correspondence between average profile and giant main pulse and interpulse $\langle \text{DM} \rangle$ measurements; and DM fluctuations on time scales of 652 days to less than 1 day. One outlying interpulse $\langle \text{DM} \rangle$ measurement from MJD 53162 is not visible, residing above the upper bound of the plot window (but see Figure 4.4).

4.5 Giant Interpulse Dispersion

As shown in Figure 4.6, over a span of 751 days the interpulse dispersion is larger and often more variable than the main pulse dispersion. Since the main pulse and interpulse ray paths are very nearly the same in the Crab nebula and ISM, it is likely that any dispersion caused in these two regions is shared by both pulses. I believe the pulsar magnetosphere is the only region along the ray paths that can exhibit the spatial and temporal variability necessary to produce the observed differences between main pulse and interpulse dispersion.

If I assume for the moment that the excess interpulse dispersion follows the cold, isotropic plasma law, I can estimate the magnetospheric charge density enhancement necessary to produce the interulses I have observed. The excess DM can be written as

$$\Delta\text{DM} = \text{DM}_{\text{ip}} - \text{DM}_{\text{mp}} = \int_{r_{\text{es}}}^{r_{\text{lc}}} N_e dr, \quad (4.5)$$

where the integral is taken over the interpulse ray path from the emission site radius, r_{es} , to the light cylinder radius, r_{lc} . The conventional magnetospheric charge density distribution goes as $N_e \propto r^{-3}$. I measure approximately

$$\Delta\text{DM} \approx 0.01 \text{ pc cm}^{-3}.$$

If I approximate the emission site as being at the stellar surface, I find

$$N_e \approx 6.2 \times 10^{28} r^{-3}. \quad (4.6)$$

The number density necessary to produce the enhanced interpulse dispersion is approximately 100 times less than the Goldreich-Julian density (the Goldreich-Julian model is introduced in § 1.1.1). The above calculation shows that if cold

plasma dispersion holds in the simple Goldreich-Julian magnetosphere, (which it probably does not for reasons discussed immediately below) there would be a sufficient number density to explain the observed higher interpulse dispersion.

The canonical pulsar model describes the magnetosphere as containing: high magnetic field strength, relativistic particle thermal speed, and relativistic particle bulk flow. These criteria call for an anisotropic and relativistic dispersion relation, unlike that in Equation (4.2). If the total pulse delay is due to the sum of delays from (i) propagation in vacuum, (ii) cold plasma ISM and nebular dispersion, and (iii) an anisotropic, relativistic magnetospheric dispersion, the interpulse propagation time delay can be written as

$$t_p = t_0 + t_{\text{ISM}} + t_{\text{mag}} = \frac{L}{c} + \text{DM}_{\text{ISM}} \frac{1}{A\nu^2} + t_{\text{mag}}(\nu), \quad (4.7)$$

where L is the path length from pulsar to Earth, $t_{\text{ISM}} = \text{DM}_{\text{ISM}}/A\nu^2$ is the cold plasma dispersion time delay, DM_{ISM} is the cold plasma dispersion measure, $A = 2.41 \times 10^{-16} \text{ s} \cdot \text{pc} \cdot \text{cm}^{-3}$ as in Equation (4.3), and $t_{\text{mag}}(\nu)$ is the time delay induced by the additional magnetospheric dispersion. If I then compute the difference in arrival time, Δt_p , and multiply by

$$A \left(\frac{1}{\nu_2^2} - \frac{1}{\nu_1^2} \right)^{-1},$$

as in Equation (4.3), I get the total apparent dispersion measure,

$$\text{DM} = \text{DM}_{\text{ISM}} + A \left(\frac{1}{\nu_2^2} - \frac{1}{\nu_1^2} \right)^{-1} [t_{\text{mag}}(\nu_2) - t_{\text{mag}}(\nu_1)]. \quad (4.8)$$

4.5.1 Dispersion-Frequency Dependence

In Figure 4.7, the average apparent dispersion measure, $\langle \text{DM} \rangle$, is plotted against average center frequency for main pulses and interpulses; data

is shown for the three observing epochs with the most main pulse and interpulse data points (MJD 53156-53378, 53582-53591, 53803-53808). The plots reveal that the main pulse $\langle \text{DM} \rangle$ is approximately constant with average center frequency. The interpulse $\langle \text{DM} \rangle$, in contrast, has a weak tendency to *increase* with average center frequency; the lower bound of the interpulse $\langle \text{DM} \rangle$ distribution is roughly equal to the main pulse $\langle \text{DM} \rangle$.

I now explore interpulse $\langle \text{DM} \rangle$ frequency dependence as a possible constraint on interpulse dispersion models. I begin by postulating that the interpulse propagation delay can be described as a power law in frequency. I gain some insight later in this section by deriving the propagation delay from the group velocity. Let the magnetospheric group velocity be written

$$v_{\text{mag}} = c \left(1 - \frac{K}{\nu^x} \right), \quad (4.9)$$

where K contains physical constants specified by the particular dispersion model. The delay time is then

$$t_{\text{mag}} \approx \frac{D}{c} \left(1 + \frac{K}{\nu^x} \right) \quad (4.10)$$

where D is the distance along the interpulse ray path in the magnetosphere, and I have approximated $K/\nu^x \ll 1$. Dropping the constant vacuum light travel time term, which is accounted for by t_0 in Equation (4.7), the expression reduces to

$$t_{\text{mag}}(\nu) = \frac{C}{\nu^x}, \quad (4.11)$$

where $C = DK/c$. Combining Equations (4.11) and (4.8) gives

$$\text{DM} = \text{DM}_{\text{ISM}} + AC\xi \quad (4.12)$$

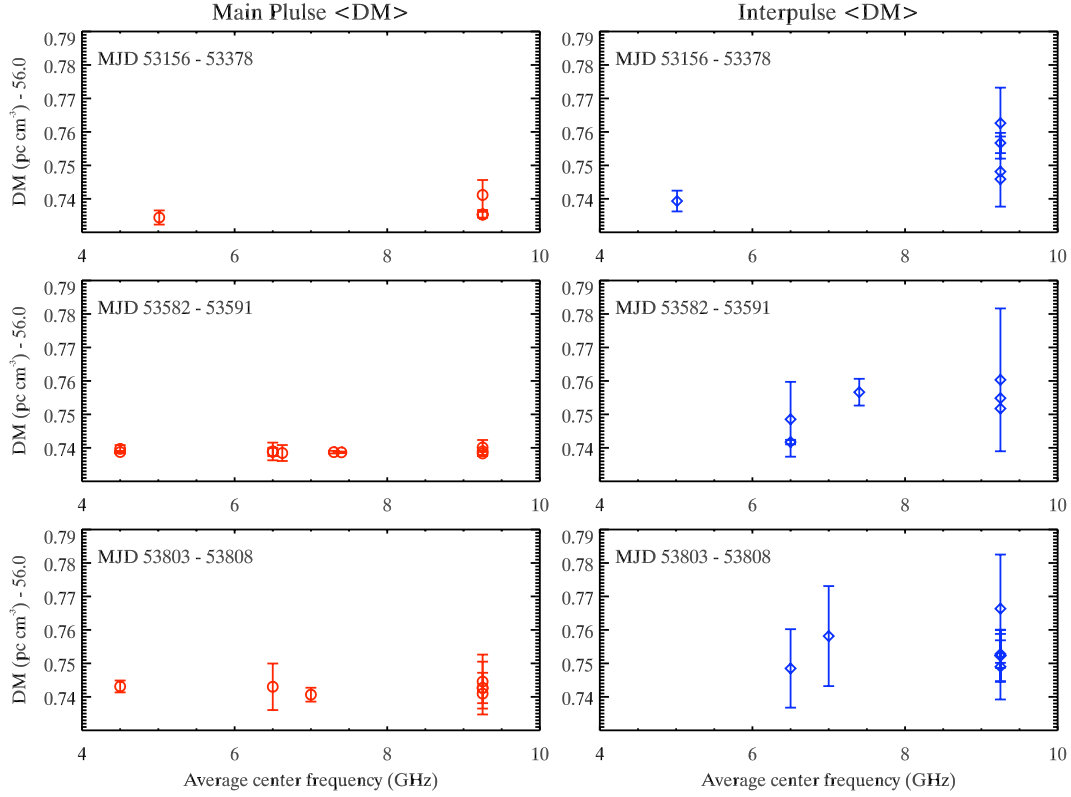


Figure 4.7: Average dispersion measure, $\langle \text{DM} \rangle$, of giant main pulses (left) and giant interpulses (right) plotted against average center frequency. The plot symbols and colors are the same as in Figure 4.4. The three rows depicted here show the three epochs of observations with the most MP and IP data points.. The main pulses and interpulses are plotted in different windows to keep the two sets of data points from overlapping and obscuring each other. In each of the three epochs, the main pulse $\langle \text{DM} \rangle$ remains roughly constant with average center frequency and approximately equal to the lower bound of the interpulse observations; the interpulse $\langle \text{DM} \rangle$ has a weak tendency to increase with average center frequency.

where

$$\xi = \left(\frac{1}{\nu_2^2} - \frac{1}{\nu_1^2} \right)^{-1} \left(\frac{1}{\nu_2^x} - \frac{1}{\nu_1^x} \right) = \left(\frac{\nu_1^x - \nu_2^x}{\nu_1^2 - \nu_2^2} \right) \left(\frac{\nu_1^2 \nu_2^2}{\nu_1^x \nu_2^x} \right). \quad (4.13)$$

Identify the ISM (cold plasma) dispersion with the main pulse, $\text{DM}_{\text{ism}} \rightarrow \text{DM}_{\text{mp}}$, and the total DM with the interpulse, $\text{DM} \rightarrow \text{DM}_{\text{ip}}$. Equation (4.12) can then be rewritten as

$$\frac{1}{A} (\text{DM}_{\text{ip}} - \text{DM}_{\text{mp}}) (\nu_1^2 - \nu_2^2) = C (\nu_1^x - \nu_2^x) (\nu_1 \nu_2)^{2-x}, \quad (4.14)$$

Let DM_{ip} and DM_{mp} be measurements made during the same observing session, using the same center frequencies, ν_1 and ν_2 . By dividing Equation (4.14) by the same equation containing DM measurements from different center frequencies, ν_3 and ν_4 , the following ratio is obtained,

$$\frac{(\text{DM}_{\text{ip}(\nu_1, \nu_2)} - \text{DM}_{\text{mp}}) (\nu_1^2 - \nu_2^2)}{(\text{DM}_{\text{ip}(\nu_3, \nu_4)} - \text{DM}_{\text{mp}}) (\nu_3^2 - \nu_4^2)} = \frac{(\nu_1^x - \nu_2^x) (\nu_1 \nu_2)^{2-x}}{(\nu_3^x - \nu_4^x) (\nu_3 \nu_4)^{2-x}}. \quad (4.15)$$

I assume the main pulse DM is constant with frequency, which is approximately true, as evidenced by Figure 4.7. Equation (4.15) can be numerically solved for x (see below and Table 4.2).

An approximate analytical solution for x can be obtained by noting that the center frequencies used in my observations allow for the following approximation,

$$\begin{aligned} \nu_2 &= \nu_1 + \delta\nu_1 = \nu_1 \left(1 + \frac{\delta\nu_1}{\nu_1} \right), & \delta\nu_1 &\ll \nu_1, \nu_2, \\ \nu_4 &= \nu_3 + \delta\nu_3 = \nu_3 \left(1 + \frac{\delta\nu_3}{\nu_3} \right), & \delta\nu_3 &\ll \nu_3, \nu_4. \end{aligned} \quad (4.16)$$

Equation (4.15) can now be approximated to zeroth order in $\delta\nu_1/\nu_1$ and $\delta\nu_3/\nu_3$ to give

$$\frac{\text{DM}_{\text{ip}(\nu_3, \nu_4)} - \text{DM}_{\text{mp}}}{\text{DM}_{\text{ip}(\nu_1, \nu_2)} - \text{DM}_{\text{mp}}} = \frac{\Delta\text{DM}_{\nu_3}}{\Delta\text{DM}_{\nu_1}} \approx \left(\frac{\nu_3}{\nu_1} \right)^{2-x}. \quad (4.17)$$

This equation can easily be solved for x (see Table 4.2).

Table 4.2 lists the values of the exponent x obtained by numerical and analytical solution of Equations (4.15) and (4.17), respectively. Solutions are listed for the same three epochs presented in Figure 4.7. The values of $DM_{ip(\nu_1, \nu_2)}$ and $DM_{ip(\nu_3, \nu_4)}$ are obtained from the interpulse data points with the smallest and largest average center frequency, respectively; the values of DM_{mp} are obtained by averaging all main pulse $\langle DM \rangle$ measurements in each epoch. The scatter in $\langle DM \rangle$ values at a given average center frequency implies a variability in x . I explore the range of x variability by first selecting $\langle DM_{ip} \rangle$ data points that together give the steepest possible DM-frequency slope (see first row of each epoch in Table 4.2), and then again by selecting data points that together give the shallowest possible slope (second row of each epoch in Table 4.2). The values of x obtained using the numerical and analytical solutions are similar. I find that the steep-slope solutions range between $-4.1 \leq x \leq -1.7$. The shallow-slope solutions range between $-0.1 \leq x \leq 1.8$. Considering the dispersion delay time, Equation (4.11), the change in x with slope makes sense: as x becomes increasingly negative, the dispersion delay and apparent DM will increase with frequency, resulting in a steeper slope in Figure 4.7; likewise, as x increases toward positive numbers, the delay and apparent DM will increase less with frequency, resulting in a shallower slope.

Table 4.2: Power law model for interpulse dispersion frequency dependence

Epoch (MJD)	ν_1 (GHz)	ν_2 (GHz)	ν_3 (GHz)	ν_4 (GHz)	DM_{mp} (pc/cm ³)	$DM_{ip}(\nu_1, \nu_2)^\dagger$ (pc/cm ³)	$DM_{ip}(\nu_3, \nu_4)^\dagger$ (pc/cm ³)	x Numerical	x Analytical
53156-53378	4.8563	5.1688	8.6250	9.8750	56.7365	56.7393	56.7626	-1.7	-1.9
53582-53591	6.1875	6.8125	8.6250	9.8750	56.7389	56.7417	56.7603	0.0	-0.1
53803-53808	6.1875	6.8125	8.6250	9.8750	56.7425	56.7485	56.7517	-3.8	-4.1
								1.2	1.1
								-1.8	-2.2
								1.6	1.8

[†]The first row of each epoch contains the DM_{ip} measurements used to obtain the steepest DM-frequency slope; the second row contains DM_{ip} measurements used to obtain the shallowest DM-frequency slope. See § 4.5.1 for discussion.

To better understand the physical significance of the x values I have measured, it is helpful to consider the group velocity expression. Equation (4.9) shows that $x < 0$ is not physically realistic, since at very high frequency $|v_{\text{mag}}|$ becomes greater than the speed of light in vacuum. It is, however, possible that x may vary with frequency, being negative within the bandwidth of my observations and positive at higher frequencies. The full range of $-4.1 \leq x \leq 1.8$ demonstrates the uncertainty in my estimation of the DM frequency dependence. This estimation uncertainty is due to the large variability in single pulse DM measurements within each of my interpulse observing sessions; the uncertainty is not a result of instrumental or algorithmic limitations.

In the subsections to follow, I compare my data with two published magnetospheric dispersion models, using characteristics other than frequency dependence.

4.5.2 Dispersion-Flux Dependence

At least two attempts have been made to describe the dispersion law in the magnetosphere (Wu & Chian, 1995; Lyutikov & Parikh, 2000). The first pertains to strong electromagnetic (EM) waves. EM waves propagating in a plasma will induce motion in the charges; a strong EM wave will induce relativistic motion. Particles with relativistic velocities appear more massive, and therefore change the dispersion law of the medium. Following Wu & Chian (1995), Clemmow (1974), and Max (1973), the index of refraction of a strong EM wave is

$$n_r^2 = 1 - \frac{2\omega_p^2}{\gamma_s \gamma_\delta \omega^2}. \quad (4.18)$$

(compare to the cold plasma index of refraction, equation [1.6]) Here, $\omega_p = \sqrt{4\pi N_e e^2/m}$ is the plasma frequency; the relativistic factor $\gamma_\delta = (1 + \delta^2)^{1/2}$, where δ is a dimensionless Lorentz-invariant parameter,

$$\delta = \frac{\omega_E}{\omega} = \frac{eE}{mc\omega},$$

e and m are the electron charge and mass, respectively, and E is the electric field; the factor $\gamma_s = (1 - V_s^2/c^2)^{-1/2}$, where V_s is the plasma streaming velocity. I will assume that a strong EM wave has $\delta \gg 1$. Recalling that $n_r = ck/\omega$, I can compute the group velocity, $v_g = d\omega/dk$, and thereby the dispersion delay time,

$$t_{\text{mag}} = \int \frac{1}{v_g} dr = \frac{1}{c} \int_{r_{\text{es}}}^{r_{\text{lc}}} \left[1 + \frac{1}{2} \left(\frac{\omega_p^2}{\gamma_s \omega_E \omega} \right)^2 \right] dr. \quad (4.19)$$

I may neglect the first term in the integrand since this is simply the vacuum light travel time and is accounted for by t_0 in Equation (4.8). If I substitute the remainder of Equation (4.19) in the magnetospheric term (second term) of Equation (4.8) I get an expression for the *apparent* DM induced by magnetospheric dispersion,

$$\text{DM}_{\text{mag}} = \frac{A}{8\pi^2} \left(\frac{1}{\gamma_s \omega_E} \right)^2 \int_{r_{\text{es}}}^{r_{\text{lc}}} \omega_p^4 dr. \quad (4.20)$$

Since $\omega_E \propto E$ and pulse flux, F_{max} , goes as $F_{\text{max}} \propto E^2$, it follows that

$$\text{DM}_{\text{mag}} = \frac{B}{F_{\text{max}}}, \quad (4.21)$$

where B consists only of physical constants and the quantity

$$\int_{r_{\text{es}}}^{r_{\text{lc}}} \frac{N_e^2}{\gamma_s^2} dr.$$

To test this, I plot single pulse DM measurements against flux for each observing session listed in Table 4.1; two example plots are shown in Figure 4.8. I find no visible systematic relationship between DM and flux, either for the interpulse or the main pulse, in any of my observations. I conclude that either the strong wave dispersion law does not apply in the magnetosphere or the DM-flux relationship derived above is hidden by DM variability from some additional phenomena.

In the case of the latter, I can place an upper limit on B by measuring the variability in DM,

$$\Delta\text{DM} = \Delta\text{DM}_{\text{mag}} = B \left(\frac{1}{F_{\text{min}}} - \frac{1}{F_{\text{max}}} \right). \quad (4.22)$$

The first equality in this equation is a statement of my belief that DM variability within a single observing session (time scales of minutes to hours) is a result of magnetospheric dispersion processes. Variables F_{min} and F_{max} are the minimum and maximum peak flux values within an observing session. Table 4.3 contains upper limits of B , and thus indirectly of

$$\int_{r_{\text{es}}}^{r_{\text{lc}}} \frac{N_e^2}{\gamma_s^2} dr,$$

obtained for interulses and main pulses in two observing sessions. In the table, $\Delta\text{DM} = \text{DM}_{\text{min}} - \text{DM}_{\text{max}}$, where DM_{min} and DM_{max} are the minimum and maximum dispersion measure values for the observing session. The main pulse limits are measured for comparison with the interpulse and are, as expected, less than the limits measured for the interpulse.

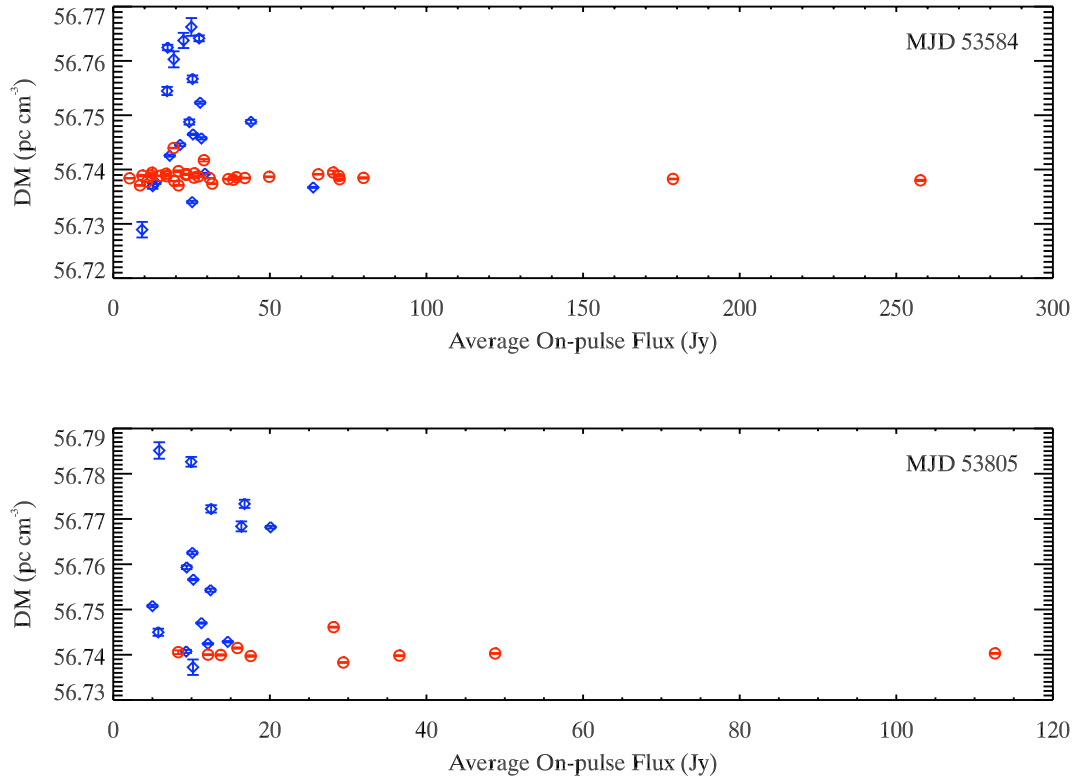


Figure 4.8: Dispersion measure versus average on-pulse flux for two observing sessions. The plot symbols and colors are the same as in Figure 4.4. The observing session from MJD 53584 corresponds to the top most of the two rows in Table 4.1 containing this date. For both of the observing sessions shown here, the on-pulse flux is calculated by averaging over $13.1 \mu\text{s}$, centered about the flux maximum; the average on-pulse flux scales with the pulse energy. In the plots shown here, there is no discernible trend in DM as a function of flux, either for the interpulse or for the main pulse.

Table 4.3: DM-flux relation for strong wave dispersion

Epoch (MJD)	Pulse	DM _{max} (pc/cm ³)	DM _{min} (pc/cm ³)	F _{max} (Jy)	F _{min} (Jy)	B < (Jy·pc/cm ³)
53584	IP	56.7663	56.7289	63.85	9.220	0.4023
	MP	56.7440	56.7371	257.7	5.209	0.03659
53805	IP	56.7851	56.7372	20.09	5.003	0.3191
	MP	56.7461	56.7383	112.6	8.299	0.06996

4.5.3 Dispersion in a Strong Magnetic Field

Another dispersion law suggested for the magnetosphere pertains to EM waves propagating through a region of strong background magnetic field and cold plasma. This model of dispersion was applied to pulsars by Lyutikov & Parikh (2000). The general expression for the index of refraction in a cold, magnetized plasma is

$$n_r^2 = 1 + \frac{\omega_p^2}{\Omega^2 - \omega^2}, \quad (4.23)$$

where $\Omega = eB/mc$ is the cyclotron frequency (compare to the index of refraction for an unmagnetized plasma, Equation [1.6]). Lyutikov & Parikh (2000) assumed $\Omega \gg \omega$ and ignored the ω in the denominator of Equation (4.23). In the following derivation I keep ω terms up to 2nd order.

By making use of the definition of the index of refraction ($n_r = ck/\omega$) and differentiating with respect to k , an expression for the EM wave group velocity can be obtained,

$$\frac{c}{v_g} = \left(1 + \frac{x^2}{1-y^2} + \frac{x^2 y^2}{(1-y^2)^2} \right) \left(1 + \frac{x^2 y}{1-y^2} \right)^{-1/2} \quad (4.24)$$

where $x = \omega_p/\Omega$ and $y = \omega/\Omega$. In a strong magnetic field, I assume $x, y \ll 1$. Two Taylor series expansions to 2nd order in x and y about $x = 0$ and $y = 0$

yield,

$$\frac{c}{v_g} \approx 1 + \frac{1}{2} \frac{\omega_p^2}{\Omega^2} + \frac{3}{2} \frac{\omega^2 \omega_p^2}{\Omega^4}. \quad (4.25)$$

The magnetospheric propagation delay time is then,

$$t_{\text{mag}} = \frac{1}{c} \int_{r_{\text{es}}}^{r_{\text{lc}}} \left(\frac{1}{2} \frac{\omega_p^2}{\Omega^2} + \frac{3}{2} \frac{\omega^2 \omega_p^2}{\Omega^4} \right) dr, \quad (4.26)$$

where the constant term, representing the light travel time in vacuum, is dropped since it is accounted for by t_0 in Equation (4.7). Substituting this expression for t_{mag} in the second term of Equation (4.8) gives the apparent magnetospheric DM,

$$\text{DM}_{\text{mag}} = -\frac{6\pi^2 A}{c} \nu_1^2 \nu_2^2 \int \frac{\omega_p^2}{\Omega^4} dr. \quad (4.27)$$

This expression for DM_{mag} does not agree with my data, since $\text{DM}_{\text{mag}} < 0$ for all values of ν_1 and ν_2 . In contrast to this model, my interpulse DM measurements are typically higher than main pulse DM measurements within the same epoch, as shown in Figure 4.6.

It should be noted that the strong magnetic field dispersion law (Lyutikov & Parikh, 2000) and the strong EM wave dispersion law (Wu & Chian, 1995) (discussed in § 4.5.2) result from approximating the conditions of the pulsar magnetosphere in different ways. The Crab giant pulses are strong enough to accelerate leptons to relativistic speeds, and the pulsar magnetosphere is strongly magnetized. The strong EM wave solution does not account for a strong background magnetic field. Alternatively, the strong magnetic field solution does not account for the relativistic effects induced by a high amplitude EM wave. In light of these approximations, the disagreement between these theories and my data is not surprising.

4.6 Conclusions

I have measured dispersion in single Crab giant pulses in 49 observing sessions over the course of 11 years. Both main pulses and interpulses have been observed. The measurements follow the same trends as average profile DM measurements over time scales of 100's to 1000's of days. The measurements vary over short time scales of minutes to hours, but these variations do not appear to be systematic. I find no correlation between DM and pulsar rotational phase, with the exception of $DM_{IP} > DM_{MP}$.

The main pulse has a marked tendency toward better agreement with average profile DM. The interpulse has a more variable, and, on average, higher DM than does the main pulse. This suggests that the interpulse undergoes an additional and variable dispersion not encountered by the main pulse. It is likely this additional dispersion is acquired within the pulsar magnetosphere.

I analyze the frequency dependence of the main pulse and interpulse data and find the main pulse DM to be approximately constant with average center frequency; the interpulse DM, however, tends to increase slightly with increasing average center frequency. This suggests that the dispersion affecting the interpulse differs from the cold plasma dispersion generally present in the magnetosphere.

I investigate two dispersion laws proposed for pulsar magnetospheres. The first magnetospheric dispersion law applies to high amplitude electromagnetic waves propagating in an isotropic, relativistic plasma. The dispersion law predicts a dependence between DM and pulse flux. I compare the single-giant-pulse measurements with average pulse flux but find no visible correlation; I

use my measurements to place upper limits on the DM-flux relationship.

The second dispersion law applies to a cold plasma in a strong magnetic field, and predicts a magnetospheric dispersion that decreases the apparent DM. This contradicts my observational findings, which indicate the magnetospheric interaction increases the apparent DM.

CHAPTER 5

CONCLUSIONS

Pulsars, and especially the Crab pulsar, remain exotic and mysterious in many ways. Though there are a number of existing models of the pulsar emission mechanism and of pulsar magnetospheres, none account for all observed phenomena (Eilek et al., 2002). Understanding requires that theory and observation continue to develop synergistically. This thesis is another step in this synergism. In this chapter I review the important results of this thesis.

5.1 Microsecond-scale Pulse Structure

By fitting the microsecond-scale structure (microbursts) of Crab giant radio pulses, I have shown that flux distributions are broad but stable. Microburst flux can vary by up to 2 orders of magnitude, even within a single pulse, but on time scales of hours to days the centroid of the flux distribution varies only by a factor of 2.

The widths of microbursts also form a wide distribution, spanning 2 orders of magnitude at frequencies between 1 and 5 GHz. Microburst widths tend to decrease with increasing frequency. Some of the observations were recorded using two distinct passbands separated by 0.2 to 4 GHz. These data reveal that microburst widths are the result of two frequency power laws working in concert: the lower bound of the width distribution follows the steep scat-

tering law of the interstellar medium, $W \propto \nu^{-4}$; however, the centroid of the width distribution reveals a variable and more shallow frequency dependence, roughly described by $W \propto \nu^{-2}$. Since the variability exists on microsecond timescales the origin of the width variation must be rapidly changing. The pulsar emission mechanism and the magnetosphere are both variable on microsecond scales and may produce the width variation observed.

Microburst energies are also distributed over several orders of magnitude. Some theorists have suggested that microbursts have constant energy in the rest frame of emission. I have transformed the rest frame constant energy model to the observed frame and found that the model overestimates the number of high energy microbursts. I find that microbursts occupy a range of energies in both the observed and emitted frame.

Plots of microburst flux versus width reveal a break in the flux-width density distribution; the distribution decays rapidly on the high-flux and large-width side of this break. The break is a physical characteristic of observed microbursts (it is not a systematic effect of instrumentation or analytic methods). The flux-width break is present at all observed frequencies, though it does move to smaller widths as the frequency increases. The microburst fitting function I have used for this analysis has a total microburst energy that is proportional to the product of flux and width, $E \propto F_{\max}W$. I have speculated that this diagonal break in the distribution may be related to a soft upper limit in microburst energy; however, overlaid lines of constant energy show that this is not exactly the case. High-energy microbursts are well sampled in my observing method and therefore this diagonal break is real, but its meaning remains

unknown.

In simultaneous two-passband observations I have identified corresponding microbursts for band separations of up to 0.5 GHz (1.2 to 1.7 GHz); corresponding bursts were not found for bands separated by 4 GHz. I conclude that the observed microburst bandwidth is $0.5 < \Delta\nu < 4$ GHz at radio frequencies between 1 and 5 GHz and may be frequency dependent. This bandwidth limitation may be imposed by the emission mechanism or by some interfering or scattering mechanism along the line of sight. Corresponding microbursts have widths and energies that are well correlated. Microburst spectral index measurements are highly variable from burst to burst, but on the whole the spectral indices are roughly consistent with average profile measurements made by other authors.

In Summary

There is a lot of variability in the pulsar magnetosphere: microburst flux, width, and energy vary over ~ 2 orders of magnitude, and this sometimes within a single pulse. Analysis of the energy distribution has shown us that energy variation is not caused by relativistic beaming but is present even in the rest frame of emission.

Microbursts, and their origin, remain mysterious: there is an unexplained limit to the product of microburst flux and width; microbursts have a finite bandwidth < 4 GHz between 1 and 5 GHz.

5.2 Echoes in Single Giant Pulses

On one day in 1996 and one day in 1997 single giant pulse observations reveal an echo-like pulse following main pulse microbursts. For both events, the echo flux is 10 times less than the flux of the “primary” main pulse microburst; the echo energy is less than the primary energy by a factor of a few; the echoes are wider than the primary microbursts by a factor of a few. The lag time between the primary and echo microbursts is $120 \geq \Delta t_{\text{lag}} \geq 40 \mu\text{s}$; the smallest echo lag ever observed for the Crab pulsar.

The 1996 observation was a simultaneous two-frequency observation (1.4 and 4.8 GHz), and the echoes are only visible in the lower frequency pass-band. The 1996 echo event lifetime is constrained to < 4 days by earlier and later observations. The short timescale of this event precludes the possibility of it being an interstellar medium refraction phenomenon. Ionized material closer to the pulsar has a much more rapid motion relative to the pulsar-Earth sight line. Timescale and frequency characteristics of the observed echoes are consistent with what is known about the Crab nebula wisps. We have calculated the electron densities of wisps resolved by the Hubble Space Telescope (Hester et al., 1995) and found the densities are too low to produce the echoes we observe. However, higher density, unresolved wisps may be present.

In Summary

These observations make a strong case that the inner nebula does affect single giant pulses. It is possible to explain some pulse phenomena, like these echoes, through the interaction of pulsed radiation with the surrounding

nebula. When pulsar observations are fortunate enough to detect echoes, the observations can be used as a probe of the environment around the star.

5.3 Dispersion Measure

I have analyzed dispersion for 11 years of Crab giant pulse observations. I find that over long time scales (100's to 1000's of days) giant pulse dispersion measure (DM) follows the same trend as average profile dispersion measurements. Over short times however, giant pulse DM varies randomly.

On short timescales, the interpulse is much more variable than the main pulse; averaged over 10s of minutes to hours, the interpulse DM measurements are greater than main pulse DM measurements. The short time scale variability of the interpulse DM, and the fact that it is on average greater than the main pulse DM, suggests that the additional dispersion occurs within the pulsar magnetosphere. The main pulse DM is constant with observing frequency to within uncertainties from pulse-to-pulse DM variation ($\sim 0.003 \text{ pc cm}^{-3}$). The interpulse DM shows a slight tendency to increase with average center frequency, despite having a larger pulse-to-pulse DM variability.

I compare my observations with two magnetospheric models and find both models to be inconsistent with my observations. The first model predicts a dependence between DM and pulse flux, but I find no visible correlation between these two quantities. I instead set an upper limit on the DM-flux relationship. The second model predicts that a strong magnetic field will weakly decrease the apparent DM. In contrast we observe a weak increase in DM¹.

¹Since we have not measured the magnetic field in the magnetosphere, we cannot comment

In Summary

The surprising result that the main and interpulse have different dispersion measures provide a new constraint on Crab pulsar models.

5.4 Pulse Scattering and Alternative Dispersion Laws

I showed in Chapter 1 that a cold plasma dispersion law [equation (1.4)]

$$\omega^2 = \omega_p^2 + k^2 c^2$$

relates to the index of refraction [equation (1.6)]

$$n_r = \sqrt{1 - \frac{\omega_p^2}{\omega^2}}$$

and to the propagation time for a pulse in a cold, isotropic plasma [equation (1.8)]

$$t_p(\omega) = \frac{L}{c} + \frac{2\pi q^2}{cm\omega^2} DM.$$

In Chapter 4, I showed evidence for an alternative dispersion law operating in giant interulses. I wrote the general propagation time for a pulse moving through a magnetosphere with an unspecified dispersion relation [equation (4.10)]

$$t_{\text{mag}} \approx \frac{D}{c} \left[1 + K \left(\frac{2\pi}{\omega} \right)^x \right].$$

Measured values of index x are given in Table 4.2. If the interpulse dispersion had been cold plasma, x would have been 2; instead, x was found to be less than 2 and vary over a wide range between -3.8 and 1.8 .

on the validity of the model itself, but only that it does not describe the data we have recorded.

The dispersion law also determines the scatter broadening function,

$$\tau \propto \left(\frac{\omega}{2\pi}\right)^y,$$

(see equations 1.9 through 1.14 for derivation) where for cold, isotropic plasma $y = -4$. The scatter broadening power law measured in Chapter 2, $y \sim -2$, (Table 2.5) differs from the simple cold plasma law. This suggests, then, that the shallow scattering law measured in Chapter 2 may result from an alternative dispersion law in the magnetosphere.

It should be noted that the frequency dependent DM measurements of Chapter 4 were made using giant interulses; in the same chapter I demonstrated that giant main pulses show no evidence of frequency dependent DM during the epochs of observation. The alternative, shallow scatter broadening law was measured in Chapter 2 using giant main pulses. If the scatter broadening is caused by alternative dispersion, it is strange that this alternative dispersion law was not detected in the analysis of Chapter 4. However, it is always possible that the alternative dispersion varies with time². My DM-frequency comparison was made using data recorded between MJD 53156 and 53808 (see §4.5.1); scatter broadening measurements were made using data from MJD 49080 to 51218 (see Table 2.1). The 1,938 days between these two data groups may explain the different results regarding dispersion.

²In fact, I found that the alternative interpulse dispersion varies over short timescales. Variability in an alternative main pulse dispersion would not be surprising.

5.5 Next Steps

It is clear that new theories and observations are required to explain these surprising measurements of Crab pulsar characteristics. The work presented in this thesis can be continued as follows.

The intriguing distribution break visible in plots of microburst flux versus width should be analyzed with careful functional fitting. Additional observations can help to gain a better grasp on this limit and its temporal and frequency dependence. The microburst fitting function I have used [equation (2.1)] suggests that this upper limit may indicate a maximum microburst energy, but the slope of the limit in flux-width space is steeper than expected. Since the origin of this upper limit remains unknown, a more careful investigation may lead to a refinement of the microburst fitting function, and additionally may give insight into pulse emission and propagation in the magnetosphere.

My study of microbursts should be extended to include interpulses, in addition to main pulses. A recent study by Hankins & Eilek (2007) has revealed new information about the differences between main and interpulses. A detailed investigation of the differences between main and interpulse microbursts may further illuminate the nature of the pulsar emission mechanism and magnetosphere. Because the interpulse varies greatly across the radio spectrum (Moffett & Hankins, 1996; Hankins & Eilek, 2007), and in particular has a complex spectrum at higher radio frequencies (>4 GHz), the observing bandwidth used for a microburst study should be carefully considered³.

³It was precisely out of concern for the differences in bandwidths that wide-band giant pulse observations from Arecibo Observatory were not added to the data analyzed in Chapter 2.

A proposal to further investigate giant pulse echoes faces the difficulty of the inability to predict when echoes will occur. Furthermore, the giant pulse echoes I observed in 1996 had a total lifetime less than 4 days. Not knowing the exact event lifetime, I cannot say whether observing such an event as a “target of opportunity” is plausible; however average profile echoes have been observed to have lifetimes of 10s of days. The best course for continuing a study of this phenomenon may be to use archival data. This presents its own challenges, as pulsar observing equipment—and especially giant pulse observing equipment—does not conform to any one standard; a variety of software may be necessary to extract the relevant information. With regard to new observations, echo events may remain serendipitous. In this case the best an observer can do is remain mindful of the possibility of echo emission appearing in a new data set.

Additional observations with excellent spectral coverage will further the work of this thesis in two ways. First, such observations can help constrain the bandwidth of Crab microbursts. I found between 1 and 5 GHz that the microburst emission bandwidth is $0.449 < \Delta\nu < 4$ GHz. A single, very wide passband or two simultaneous passbands separated by various frequency intervals may constrain this limit. A good limit will give insight into the poorly understood pulse emission and magnetospheric propagation processes.

Second, observations with excellent spectral coverage will help to confirm or refute the possibility of an alternative dispersion law operating in the Crab pulsar magnetosphere. I have proposed this possibility based on dispersion and scattering measurements made over a range of frequencies; still the proposal remains tenuous because of the large variability in both dispersion

and scattering measurements. Additional data recorded in other parts of the radio spectrum may help to better quantify dispersion and scattering trends. Such quantification may provide an important platform for new models of the pulsar magnetosphere and emission mechanism.

Bibliography

- Arendt, Jr., P. N., & Eilek, J. A. 1998, *ArXiv Astrophysics e-prints*, (astro-ph/9707195)
- Armstrong, J. W., Rickett, B. J., & Spangler, S. R. 1995, *Astrophys. J.*, **443**, 209
- Atoyan, A. M. 1999, *Astr. Astrophys.*, **346**, L49
- Baars, J. W. M., Genzel, R., Pauliny-Toth, I. I. K., & Witzel, A. 1977, *Astr. Astrophys.*, **61**, 99
- Backer, D. C. 1988, in *Galactic and Extragalactic Astronomy*, 2nd edn., ed. G. L. Verschuur & K. I. Kellermann (New York: Springer-Verlag), 480–521
- Backer, D. C. 2002, private communication
- Backer, D. C., Wong, T., & Valanju, J. 2000, *Astrophys. J.*, **543**, 740
- Benford, G. 2003, *Physics Letters A*, **318**, 412
- Bietenholz, M. F., Hester, J. J., Frail, D. A., & Bartel, N. 2004, *Astrophys. J.*, **615**, 794
- Bracewell, R. 2000, *The Fourier Transform and Its Applications*, 3rd edn. (New York: McGraw-Hill Book Company)
- Carroll, B. W., & Ostlie, D. A. 1996, *An Introduction to Modern Astrophysics* (Reading, Massachusetts: Addison-Wesley)

- Clemmow, P. C. 1974, *Plasma Phys.*, **12**, 287
- Cordes, J. M. 1976, *Astrophys. J.*, **210**, 780
- Cordes, J. M., Bhat, N. D. R., Hankins, T. H., McLaughlin, M. A., & Kern, J. 2004, *Astrophys. J.*, **612**, 375
- Cordes, J. M., & Lazio, T. J. W. 2002, *ArXiv Astrophysics e-prints*, (astro-ph/0207156)
- Craft, Jr., H. D., Comella, J. M., & Drake, F. D. 1968, *Nature*, **218**, 1122
- Dickerson, J. D. 2003, Master's thesis, New Mexico Institute of Mining and Technology
- Eilek, J. A., Arendt, Jr., P. N., Hankins, T. H., & Weatherall, J. C. 2002, in *Neutron Stars, Pulsars, and Supernova Remnants*, ed. W. Becker, H. Lesch, & J. Trümper, 249–+
- Gold, T. 1968, *Nature*, **218**, 731
- Goldreich, P., & Julian, W. H. 1969, *Astrophys. J.*, **157**, 869
- Hankins, T. H. 1971, *Astrophys. J.*, **169**, 487
- Hankins, T. H., & Eilek, J. A. 2007, *Astrophys. J.*, **670**, 693
- Hankins, T. H., Kern, J. S., Weatherall, J. C., & Eilek, J. A. 2003, *Nature*, **422**, 141
- Hankins, T. H., & Rickett, B. J. 1975, *Methods in Computational Physics*, Vol. 14, *Pulsar Signal Processing* (New York: Academic Press), 55–129

- Hester, J. J., Mori, K., Burrows, D., Gallagher, J. S., Graham, J. R., Halverson, M., Kader, A., Michel, F. C., & Scowen, P. 2002, *Astrophys. J.*, **577**, L49
- Hester, J. J., Scowen, P. A., Sankrit, R., Burrows, C. J., Gallagher, J. S., Holtzman, J. A., Watson, A., Trauger, J. T., Ballester, G. E., Casertano, S., Clarke, J. T., Crisp, D., Evans, R. W., Griffiths, R. E., Hoessel, J. G., Krist, J., Lynds, R., Mould, J. R., O'Neil, E. J., Stapelfeldt, K. R., & Westphal, J. A. 1995, *Astrophys. J.*, **448**, 240
- Hewish, A., Bell, S. J., Pilkington, J. D., Scott, P. F., & Collins, R. A. 1968, *Nature*, **217**, 709
- Isaacman, R., & Rankin, J. M. 1977, *Astrophys. J.*, **214**, 214
- Kern, J. S. 2004, PhD thesis, New Mexico Institute of Mining and Technology
- Kraus, J. D. 1986, *Radio astronomy* (Powell, Ohio: Cygnus-Quasar Books, 1986)
- Lee, L. D., & Jokipii, J. R. 1975, *Astrophys. J.*, **201**, 532
- Lorimer, D. R., Yates, J. A., Lyne, A. G., & Gould, D. M. 1995, *Mon. Not. R. astr. Soc.*, **273**, 411
- Lorrain, P., & Corson, D. R. 1970, *Electromagnetic Fields and Waves*, 2nd edn. (San Francisco: W. H. Freeman and Company)
- Lundgren, S. C., Cordes, J. M., Ulmer, M., Matz, S. M., Lomatch, S., Foster, R. S., & Hankins, T. 1995, *Astrophys. J.*, **453**, 433

- Lyne, A. G., Pritchard, R. S., & Graham-Smith, F. 2001, *Mon. Not. R. astr. Soc.*, **321**, 67
- Lyne, A. G., & Thorne, D. J. 1975, *Mon. Not. R. astr. Soc.*, **172**, 97
- Lyutikov, M. 2003, *Mon. Not. R. astr. Soc.*, **346**, 540
- . 2006, *Mon. Not. R. astr. Soc.*, **367**, 1594
- Lyutikov, M., & Parikh, A. 2000, *Astrophys. J.*, **541**, 1016
- Manchester, R. N., Hobbs, G. B., Teoh, A., & Hobbs, M. 2005, *Astron. J.*, **129**, 1993
- Manchester, R. N., & Taylor, J. H. 1972, *Astrophys. Lett.*, **10**, 67
- Max, C. E. 1973, *Phys. Fluids*, **16**, 1277
- Meszaros, P. 1992, *High-energy radiation from magnetized neutron stars Meszaros*. (Chicago : University of Chicago Press, c1992.), 47–+
- Moffett, D. A. 1997, PhD thesis, New Mexico Institute of Mining and Technology
- Moffett, D. A., & Hankins, T. H. 1996, *Astrophys. J.*, **468**, 779
- Mori, K., Hester, J. J., Burrows, D. N., Pavlov, G. G., & Tsunemi, H. 2002, in ASP Conf. Ser. 271: Neutron Stars in Supernova Remnants, ed. P. O. Slane & B. M. Gaensler, 157–+
- Petrova, S. A. 2004, *Astr. Astrophys.*, **424**, 227

- Phillips, J. A., & Wolszczan, A. 1991, *Astrophys. J.*, submitted
- Popov, M. V., Kuzmin, A. D., Ulyanov, O. M., Deshpande, A. A., Ershov, A. A., Kondratiev, V. I., Kostyuk, S. V., Losovsky, B. Y., Soglasnov, V. A., & Zakharenko, V. V. 2006, *On the Present and Future of Pulsar Astronomy, 26th meeting of the IAU, Joint Discussion 2, 16-17 August, 2006, Prague, Czech Republic, JD02, #19, 2*
- Popov, M. V., & Stappers, B. 2007, *Astr. Astrophys.*, **470**, 1003
- Press, W. H., Teukolsky, S. A., Vetterling, W. T., & Flannery, B. P. 1992, *Numerical Recipes in FORTRAN*, 2nd edn. (New York: Cambridge University Press)
- Rankin, J. M., Campbell, D. B., Isaacman, R. B., & Payne, R. R. 1988, *Astr. Astrophys.*, **202**, 166
- Rankin, J. M., Comella, J. M., Craft, Jr., H. D., Richards, D. W., Campbell, D. B., & Counselman, C. C. 1970, *Astrophys. J.*, **162**, 707
- Rankin, J. M., & Roberts, J. A. 1971, in IAU Symp. 46: The Crab Nebula, ed. R. D. Davies & F. Graham-Smith, 114–+
- Rickett, B. J. 1977, *Ann. Rev. Astr. Ap.*, **15**, 479
- . 1990, *Ann. Rev. Astr. Ap.*, **28**, 561
- Rickett, B. J., & Lyne, A. G. 1990, *Mon. Not. R. astr. Soc.*, **244**, 68
- Ruderman, M. A., & Sutherland, P. G. 1975, *Astrophys. J.*, **196**, 51

- Rybicki, G. B., & Lightman, A. P. 1979, *Radiative Processes in Astrophysics*
(New York: Wiley)
- Sallmen, S., Backer, D. C., Hankins, T. H., Moffett, D., & Lundgren, S. 1999,
Astrophys. J., **517**, 460
- Sankrit, R., Hester, J. J., Scowen, P. A., Ballester, G. E., Burrows, C. J.,
Clarke, J. T., Crisp, D., Evans, R. W., Gallagher, III, J. S., Griffiths, R. E.,
Hoessel, J. G., Holtzman, J. A., Krist, J., Mould, J. R., Stapelfeldt, K. R.,
Trauger, J. T., Watson, A., & Westphal, J. A. 1998, *Astrophys. J.*, **504**, 344
- Scheuer, P. A. G. 1968, *Nature*, **218**, 920
- Sheckard, J., Eilek, J., & Hankins, T. 2009, in preparation
- Słowikowska, A., Jessner, A., Klein, B., & Kanbach, G. 2005, in AIP Conf.
Proc. 801: Astrophysical Sources of High Energy Particles and Radiation,
ed. T. Bulik, B. Rudak, & G. Madejski, 324–329
- Smith, F. G., & Lyne, A. G. 2000, in ASP Conf. Ser. 202: IAU Colloq. 177:
Pulsar Astronomy - 2000 and Beyond, ed. M. Kramer, N. Wex, & W. R.,
499–502
- Soglasnov, V. A., Popov, M. V., Bartel, N., Cannon, W., Novikov, A. Y.,
Kondratiev, V. I., & Altunin, V. I. 2004, *Astrophys. J.*, **616**, 439
- Staelin, D. H., & Reifenstein, III, E. C. 1968, *Science*, **162**, 1481
- Taylor, J. H., & Weisberg, J. M. 1989, *Astrophys. J.*, **345**, 434

- Weisskopf, M. C., Hester, J. J., Tennant, A. F., Elsner, R. F., Schulz, N. S.,
Marshall, H. L., Karovska, M., Nichols, J. S., Swartz, D. A., Kolodziejczak,
J. J., & O'Dell, S. L. 2000, *Astrophys. J.*, **536**, L81
- Wu, X., & Chian, A. C.-L. 1995, *Astrophys. J.*, **443**, 261